



**MONASH** University

**Observations of Microphysical Properties of Wintertime Low-altitude  
Clouds over the Southern Ocean**

Eunmi Ahn

Mathematical Sciences General

A thesis submitted for the degree of Doctor of Philosophy at

Monash University in 2017

School of Earth, Atmosphere and Environment

---

## **Copyright notice**

© Eunmi Ahn 2017

*I certify that I have made all reasonable efforts to secure copyright permissions for third-party content included in this thesis and have not knowingly added copyright content to my work without the owner's permission.*

---

## Abstract

The energy and water budgets over the Southern Ocean (SO) remain outstanding challenges to the climate community with persistent biases noted in coupled global climate models and the reanalysis products. Consequently, the microphysics and macrophysics of clouds over the SO have attracted considerable attention over the past decade, especially as current satellite products have demonstrated that these clouds are different from those over the Northern Hemisphere. Multiple analyses have suggested that the clouds over the SO more frequently contain supercooled liquid water at colder temperatures. Interest in the microphysics of these clouds goes back even further, where *in-situ* observations recorded large seasonal cycles in the cloud droplet number concentration ( $N_d$ ) and effective radius ( $r_{eff}$ ). Wintertime observations off the coast of Tasmania from the SO Cloud Experiment (SOCEX I) in the 1990's observed some of the lowest boundary layer values of  $N_d$  (10 – 40  $\text{cm}^{-3}$ ) on record.

This research analyses *in-situ* observations of the microphysical properties of the SO clouds (43 – 45 °S, 145 – 148 °E) from 20 flights taken over three winters (Jun – Oct, 2013 - 2015). Unlike the SOCEX I observations, these new field observations have been made under a variety of meteorological conditions. Subsequently, we have found a high frequency (~37%) of the total cloud records to consist of mixed phase clouds, as opposed to strictly supercooled liquid water. Looking at the remaining liquid water samples, 18 flights have  $N_d$  in the range of SOCEX I, but two distinct flights were found to have high  $N_d$  (80 – 90  $\text{cm}^{-3}$ ). The clouds from these two flights were further unique in that they were largely not drizzling and they formed as closed mesoscale cellular convection. Overall, 49% of all liquid cloud samples were observed to be drizzling with an average drizzle rate of 0.73  $\text{mmhr}^{-1}$ .

Eleven of these 20 flights were arranged so that they were observing clouds when the A-train satellite constellation passed overhead, and they have been employed to evaluate the microphysics products of MODIS ( $N_d$ ,  $r_{eff}$  and cloud-top thermodynamic phase) and CALIPSO (cloud-top thermodynamic phase). Compared to the *in-situ* observations, the

---

CALIOP and MODIS cloud phase optical product underestimated the occurrence of ice clouds, whereas the MODIS infrared product shows better agreement qualitatively but overestimated the *in-situ* ice frequency with a frequent classification of uncertainty. The MODIS  $r_{eff\_2.1}$  overestimates the *in-situ*  $r_{eff}$  for non-drizzling clouds (by  $\sim 13\mu\text{m}$  on average) and, to a lesser extent, for lightly drizzling cases (by  $\sim 4.8\mu\text{m}$  on average). Conversely, MODIS  $r_{eff\_2.1}$  underestimates the *in-situ*  $r_{eff}$  for heavily drizzling cases by  $\sim 10\mu\text{m}$  on average. This overestimation by MODIS is greater (67%) than that reported for other experiments (e.g. that of the stratiform clouds over South East Pacific from VAMOS Ocean-Cloud-Atmosphere-Land Study Regional Experiment (VOCALS-REx)). We also note that the success of the retrieval was strongly affected by the presence of drizzle.

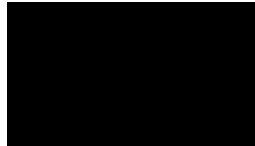
This research demonstrates that greater variability exists in the microphysics of wintertime clouds over the SO than previously reported, when a wider range of synoptic meteorology is investigated. Further, the remote-sensing capabilities of MODIS and CALIOP have substantial uncertainties in the retrievals for these clouds, particularly as they are commonly patchy, partially glaciated and drizzling.

---

## Declaration

This thesis contains no material which has been accepted for the award of any other degree or diploma at any university or equivalent institution and that, to the best of my knowledge and belief, this thesis contains no material previously published or written by another person, except where due reference is made in the text of the thesis.

Signature:



.....

Print Name: ...Eunmi Ahn.....

Date: ...6/Dec/2017.....

## Publications during enrolment

Eunmi Ahn, Yi Huang, Steven T. Siems and Michael J. Manton, " A comparison of cloud microphysical properties derived from MODIS and CALIPSO with *in-situ* measurements over the wintertime Southern Ocean ", *Journal of Geophysical Research*, subject to submit.

Eunmi Ahn, Yi Huang, Thomas H. Chubb, Darrel Baumgardner, Peter Isaac, Mark de Hoog, Steven T. Siems, Michael J. Manton "In situ observations of wintertime low-altitude clouds over the Southern Ocean." *Q. J. R. Meteorol. Soc* **143**. 704 (2017): 1381–1394, doi: 10.1002/qj.3011.

### Thesis including published works declaration

I hereby declare that this thesis contains no material which has been accepted for the award of any other degree or diploma at any university or equivalent institution and that, to the best of my knowledge and belief, this thesis contains no material previously published or written by another person, except where due reference is made in the text of the thesis.

This thesis includes 1 original paper published in peer reviewed journals and 1 to be submitted. The core theme of the thesis is to study on microphysical properties of wintertime low-altitude clouds and drizzle over the SO through in-situ observations and evaluate satellite products employing the observations. The ideas, development and writing up of all the papers in the thesis were the principal responsibility of myself, the student, working within the Monash University under the supervision of Steven Siems.

The inclusion of co-authors reflects the fact that the work came from active collaboration between researchers and acknowledges input into team-based research.

In the case of Chapter 2, 3, 4 and 5 my contribution to the work involved the following:

Thesis Chapter	Publication Title	Status (published, in press, accepted or returned for revision, submitted)	Nature and % of student contribution	Co-author name(s) Nature and % of Co-author's contribution*	Co-author(s), Monash student Y/N*
2 and 3	<i>In situ observations of wintertime low-altitude clouds over the Southern Ocean</i>	Published	80%. Concept and analysing data and writing first draft	1) Yi Huang, input into manuscript 7% 2) Thomas H. Chubb, Data analysis, input into manuscript 3% 3) Darrel Baumgardner, Data analysis, input into manuscript 2% 4) Peter Isaac, Data analysis, input into manuscript 2% 5) Mark de Hoog, Data analysis, input into manuscript 2%	No No No No No

				6) Steve T. Siems, Data analysis, input into manuscript 2% 7) Michael Manton, Data analysis, input into manuscript 2%	No No
4	<i>A comparison of cloud microphysical properties derived from MODIS and CALIPSO with in-situ measurements over the wintertime Southern Ocean</i>	<i>Returned for revision</i>	<i>80%. Concept and analysing data and writing first draft</i>	1) Yi Huang, input into manuscript 12% 2) Steve T. Siems, Data analysis, input into manuscript 5% 3) Michael Manton, Data analysis, input into manuscript 3%	No No No

I have renumbered sections of submitted or published papers in order to generate a consistent presentation within the thesis.

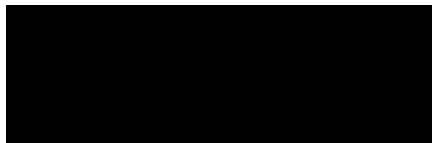
**Student signature:**



**Date:** 5/12/2017

The undersigned hereby certify that the above declaration correctly reflects the nature and extent of the student's and co-authors' contributions to this work. In instances where I am not the responsible author I have consulted with the responsible author to agree on the respective contributions of the authors.

**Main Supervisor signature:**



**Date:** 5/12/2017

---

## Acknowledgements

*I am blessed to find Professor Steve Siems as my supervisor. I gratefully acknowledge him for guiding, advising, and supporting me throughout the research. Without his continuous encouragement, enthusiasm and patience, this study would hardly have been completed. His kind guide and inspiration shall always be remembered. I owe my deepest gratitude to my other supervisor Professor Michael Manton, who provides his valuable resources, which helped me to improve the quality of my work and made it commendable and worthy.*

*I have my deep appreciation and regard for Dr. Yi Huang, a research fellow in School of Earth, Atmosphere and Environment and coauthor of our two papers during my candidature. Not only she made many important suggestions which enhanced this study, but also she kept inspired me with her great enthusiasm and sharp and detailed advice. I would like to extend my thanks to Thom Chubb and Peter Isaac for your outstanding works on the in-situ observations data and kind directions and supports. This study would not have been made without their unwearied and intellectual contributions. I would also like to express my gratitude to Darrel Baumgardner, who has been a coauthor on the one paper presented in this thesis. I really appreciate his insightful suggestion to improve the study. I also deeply appreciate Aaron Bansemer, NCAR, for his expert advice and constant support with the CIP data analysis.*

*I am very grateful to the cloud seeding team of Hydro Tasmania. It was really appreciated for their continuous collaboration on the field project to make the research possible and valuable. Thanks Christina Nebel, Mark DeHoog, and Mike for organising, supporting, and conducting the flights.*

*My appreciation is also to my colleagues and staff of school of EAE at Monash University for your kind and generous support. Thank you my dear friends for all your support and encouragement when I have gone through difficult times.*

*I owe a great debt of gratitude to my husband, my daughter and my family. Words can not express how grateful I am to them. Thank you especially to my mother, brother, sister, and in-laws. Thank you to my beloved husband for all of the devotions that you've made. Your love, sacrifice and trust for me were what sustained me this far.*

---

# Contents

<i>Abstract</i>	<i>ii</i>
<i>Declaration</i>	<i>iv</i>
<i>Publications during enrolment</i>	<i>v</i>
<i>Acknowledgements</i>	<i>vii</i>
<i>Contents</i>	<i>viii</i>
<i>List of Figures</i>	<i>xi</i>
<i>List of Tables</i>	<i>xv</i>
<b>Chapter 1</b>	<b>1</b>
1.1 Unique features of the Southern Ocean clouds and drizzle	2
1.2 Cloud $N_d$ and $r_{eff}$ in marine boundary layer clouds dynamics	6
1.3 Past field campaigns on the SO clouds and drizzle	9
1.4 Satellite observations of the SO clouds and drizzle	12
1.5 Aims summary	17
<b>Chapter 2</b>	<b>19</b>
2.1 Flight overview and instrumentation	20
2.1.1 Flight overview	20
2.1.2 Aircraft instrumentation	25
2.2 Meteorology	27
2.3 Cloud thermodynamic phase	29
2.4 Mean microphysical characteristics of liquid clouds	33
2.5 Summary and discussion	40
<b>Chapter 3</b>	<b>43</b>
3.1 Drizzle fraction and rain rate	44
3.2 Mean microphysical properties of drizzling and non-drizzling clouds	46
3.3 A Comparison of drizzle and non-drizzle cases	49

3.4 Summary and discussion	58
<b>Chapter 4</b>	<b>60</b>
4.1 Introduction	61
4.2 Data and methodology	63
4.2.1 Flight overview and aircraft measurements	63
4.2.2 MODIS data	65
4.2.3 CALIOP data	67
4.3 Cloud thermodynamic phase	70
4.3.1 CALIOP	72
4.3.2 MODIS	75
4.4 Cloud Microphysics	77
4.4.1 MODIS Cloud $r_{eff}$	82
4.4.2 MODIS Cloud $N_d$	86
4.5 Discussions and Summary	89
<b>Chapter 5</b>	<b>93</b>
5.1 Introduction	94
5.2 Experimental Design and Data	96
5.2.1 Experimental Design	96
5.2.2 Data	98
5.2.3 Meteorology	100
5.3 Preliminary Results	101
5.4 Preliminary Conclusions	107
<b>Chapter 6</b>	<b>110</b>
6.1 Summary and Discussions	111
6.2 Future Directions	117
<b>Reference</b>	<b>120</b>
<b>APPENDIX</b>	<b>142</b>
Cloud seeding flights	142
Error estimates	143
CIP data processing	145

---

<b>Calculation of liquid and ice water content from WCM-2000_____</b>	<b>145</b>
<b>Cloud phase observed by <i>in-situ</i> and MODIS in spatiotemporally coincided_____</b>	<b>147</b>

---

## List of Figures

Figure 1.0 Souther Ocean waves are known to be the largest due to the strongest boundary layer winds (zonally averaged) across the globe in the absence of any significant land mass.....	1
Figure 1.1. Ensemble mean error for CMIP5 model in shortwave radiation absorbed by the Earth System. ....	4
Figure 1.2. Conceptual system dynamics diagram illustrating important feedbacks related to the macrophysical and microphysical properties of stratiform top boundary layer (STBL).....	7
Figure 1.3. Seasonal cycles of cloud drop concentration ( $N_d$ ) and CCN concentration over the Southern Ocean.....	14
Figure 2.0 The Cessna Conquest aircraft hired by Hydro Tasmania and used for in-situ observations.....	19
Figure 2.1. Seventy-two hour Hybrid Single Particle Lagrangian Integrated Trajectory Model (HYSPLIT) back trajectories for 20 flights of three consecutive winters (Jun - Oct, 2013 - 2015) with the Global Data Assimilation System (GDAS) reanalysis. ....	21
Figure 2.2. Mean sea level pressure (MSLP) from 15 <sup>th</sup> August, 2013 00 UTC..	28
Figure 2.4. Fractions of cloud phase coefficient ( $\mu_3$ ) for different temperature intervals for 5 different field campaigns across Canada (Adapted from Korolev et al., 2013). ....	32
Figure 2.5. Averaged microphysical properties and spectra by temperature for liquid clouds from 20 flights observations of three consecutive winters (Jun - Oct, 2013 - 2015). ....	37
Figure 3.0 Broken, patchy and drizzling cloud imagery taken by the Gopro camera equipped on the Cessna Conquest aircraft at 14:35 AEST, 30-August-2015 heading north. ....	43
Figure 3.1. The probability density function (PDF) of drizzling and non-drizzling sections of liquid clouds from 20 flights observations of three consecutive winters (Jun - Oct, 2013 - 2015).....	45
Figure 3.2. The probability density function (PDF) of (a) $N_d$ , (b) reff (CAS + CIP), (c) LWC (CAS+CIP), and (d) the spectra of drizzling and non-drizzling	

---

liquid clouds from 20 flights' observations of three consecutive winters (Jun - Oct, 2013 - 2015). .....	48
Figure 3.3. Comparison of $r_{eff}$ and spectra for CASES A and B against all 18 flights. 'All' means all flights except CASES A and B. ....	50
Figure 3.4. MODIS satellite images (a) - (d) and soundings (e) - (h) for two minimum drizzle cases, CASES A and B (23 July 2013 and 01 October 2015, respectively) and two heavily drizzle cases, CASES C and D (28 June 2013 and 30 August 2015, respectively). ....	55
Figure 3.5. (a) – (d) Vertical profile of cloud microphysical properties ( $N_d$ , $r_{eff}$ , and LWC) from the soundings of non-drizzling cases (CASES A and B) and drizzling dominant (CASES C and D) flights in Figure 3.4 (e) ~ (h). ....	57
Figure 4.0 MODIS on board Aqua visible imagery at 14:25 AEST, 30-August-2015. Open MCC cloud is noticeable where the research flight was conducted at ~44.5°S, 147°E adjacent to closed MCC clouds near 46°S and 148°E. ....	60
Figure 4.1. Composite images of longitude-altitude cross section of aircraft flight track for 20130614 on spatiotemporally coincided Aqua MODIS retrieval map. ....	69
Figure 4.2. Vertical profiles of the CALIOP cloud phase for nine flights from 2013 – 2015. Each flight has two CALIOP profiles; first profile with high altitude and second profile with low altitude zoomed in the target coincided area. The red line on the second profile indicates the coincided altitudes with the aircraft track. ROI, HOI and UK/ND mean “randomly-oriented ice”, “horizontally-oriented ice”, and “unknown / not determined” .....	74
Figure 4.3. Vertical profiles of $r_{eff}$ from spatiotemporally coincided aircraft measurements and MODIS retrievals for eleven flights from 2013 – 2015. ....	80
Figure 4.4. Comparison of liquid cloud effective radius ( $r_{eff}$ ) retrieved from Aqua MODIS with <i>in-situ</i> measurements from CAS + CIP. The MODIS $r_{eff}$ is retrieved by channel (each column) and by cloud regime (each row).....	83
Figure 4.5. Same as Figure 4.4 but for $N_d$ . $N_d$ is derived by the MODIS retrievals of $r_{eff}$ and COT.....	87

---

Figure 4.6. Cloud optical thickness (COT) as a function of $N_d$ for “merged” (overcast + PCL) pixels retrieved from Aqua MODIS and derived from equation (1), respectively. ....	88
Figure 5.0 Artist's concept of the Global Precipitation Measurement (GPM) core observatory and the swath coverage by the GPM sensors. ....	93
Figure 5.1. Experimental design for the case study for 30 <sup>th</sup> August, 2015. ....	97
Figure 5.2. The mean-sea-level pressure (MSLP) diagrams for 0000 and 0600 UTC 30 August 2015.....	100
Figure 5.3. Time series of rain rate (RR, mmhr <sup>-1</sup> ) and CIP image from aircraft observations during 30 August 2015 flight.....	102
Figure 5.4. A-Train satellite observations at 04:30 UTC 30 August 2015. (a) CALIOP categorization. (b) CloudSat CPR reflectivities.....	104
Figure 5.5. Time averaged map of multi-satellite precipitation estimate – half hourly 0.1 deg. [GPM_3IMERGHH v04] mmhr <sup>-1</sup> over 2015-08-30 0500 UTC – 2015-0830 0529 UTC, region 144E, 47S, 150E, 40S. ....	105
Figure 5.6. Time Averaged map of the GPM multi-satellite precipitation estimate with gauge calibration – Final Run half-hourly 0.1 deg. [mmhr <sup>-1</sup> ] over 2015-08-30 0430 UTC – 2015-08-30 0529 UTC. ....	106
Figure 5.7. ACCESS simulated surface precipitation at 0405 UTC 30 August 2015 with aircraft track overlaid. ....	107
Figure A1. The cloud seeding map in in 4 <sup>th</sup> August 2015. The map below shows the flight path for a cloud seeding flight targeting the Gordon catchment. The average wind direction was westerly (270) with a speed of 25 knots. The broken lined circle is where the clouds selected for the analysis. ....	142
Figure A2. Comparisons of LWC [gm <sup>-3</sup> ] from different measurements for 14 June 2013 flight, as noted. The correlation coefficients for (a) – (d) are 0.99, 0.79, 0.82, and 0.99, respectively and their linear regression equations are $y = 0.49x + 0.01$ , $y = 0.78x + 0.05$ , $y = 0.93x + 0.01$ , and $y = 0.94x + 0.02$ , respectively.....	144
Figure A3. Composite 3-D images of aircraft track and MODIS cloud phase optical properties (CPOP) retrieval pixels for each flight which are spatiotemporally coincided. The aircraft track is plotted with yellow line with green star for starting and purple star for ending point for the collocation.	

---

Cloud phase determined by aircraft measurements and MODIS CPOP product is indicated with different colours.....	147
Figure A4. The CIP images of mixed/ice phase clouds for four flights which heavily or lightly experienced of ice. ....	151
152	
Figure A5. Hybrid Single Particle Lagrangian Integrated Trajectory Model (HYSPLIT) back trajectory ensembles for the high $N_d$ cases (20130723 and 20151001).....	152
Figure A6. Mesoscale satellite imagery of cloud and MCC classification (a) a visible reflectance image (250-m resolution) for stratocumulus cloud by MODIS (left) and a visible image (15 m resolution) by Advanced Spaceborne Thermal Emission and Reflection Radiometer (ASTER) taken at 1235 UTC, 7 Apr 2001 over the northeast Atlantic Ocean (Adapted from Wood (2012).) (b) Illustration of the MCC classification (Adapted from Wood and Hartmann (2006)) .....	153
Figure A7. MODIS visual images sorted by MCC classification for the 20 flights. The flight location is marked as red on each image. ....	154
Figure A8. Mean Sea Level Pressure (MSLP) diagrams for the two high $N_d$ cases (20130723 and 20151001).....	155

---

## List of Tables

Table 2.1. Summary of synoptic conditions and thermodynamic and cloud microphysical properties for each flight for winter time during 2013-2015. ....	23
Table 2.2. The major instruments used for the research and their ranges for measurements. ....	26
Figure 2.3. Fractions of cloud phase coefficient ( $\mu_3$ ) for different temperature intervals for 20 flights of three consecutive winters (Jun - Oct, 2013 - 2015). ....	31
The durations of the sampled data are indicated in the legend next to the temperature bins. ....	31
Table 2.3. Overall averages of the liquid-only cloud average microphysical properties for 20 flights' observations of three consecutive winters (Jun - Oct, 2013 - 2015). ....	34
Table 3.1. Summary of microphysical properties of 1 and 10 s consistent drizzle and non-drizzle sections of clouds from 20 flights' observations of three consecutive winters (Jun - Oct, 2013 - 2015). The standard deviations (s.d.) are indicated in parentheses. ....	46
Table 3.2. Comparison of thermodynamic and microphysical properties and meteorology from the soundings for two non-drizzle dominant cases (CASES A and B, 23 July 2013 and 01 October 2015, respectively) and two drizzle dominant cases (CASES C and D, 28 June 2013 and 30 August 2015, respectively).....	52
Table 4.1 Summary of the eleven flights from 2013 – 2015 spatiotemporally coincided with A-Train constellation (MODIS and CALIPSO). ....	64
Table 4.2. Compositions of cloud phase for the eleven flights from 2013 – 2015 discriminated by aircraft measurements, CALIOP retrievals, and MODIS IR and CPOP product. The MODIS cloud phase is separated with single-layer cloud and all clouds including multi-layered clouds determined by MODIS Cloud Multi Layer Flag SDS. Cloud top temperature (CTT) and cloud top	

---

height (CTH) are the average values for the ice phase clouds for all cases. The three ‘widely iced’ cases are highlighted. ....	71
Table 4.3. MODIS $r_{eff}$ retrieval failure rates for drizzling/non-drizzling flights and cloud regime (overcast and PC) spatiotemporally aligned with <i>in-situ</i> observations from eleven flights from 2013-2015. ....	78
Figure 6.0 Global distribution of the frequency of occurrence of Mesoscale Cellular Convection (MCC) types over the ocean based on 1 year of MODIS Aqua observations from 2008. ....	110

---

# Chapter 1

## Introduction



Figure 1.0 Southern Ocean waves are known to be the largest due to the strongest boundary layer winds (zonally averaged) across the globe in the absence of any significant land mass.

---

## 1.1 Unique features of the Southern Ocean clouds and drizzle

The Southern Ocean (SO), covering 15% of the earth's surface, surrounds Antarctica and interacts closely with the massive ice shelves. Being largely remote from anthropogenic influences, the SO is sheathed in pristine clouds. These atmosphere and clouds transport water and energy to and from the Antarctic (Fitzpatrick and Warren, 2007; Yin, 2005) while the atmosphere and ocean further exchange heat, water and numerous chemical species including a vast uptake of carbon dioxide into the ocean (Caldeira and Duffy, 2000). These clouds have a high fractional cloud cover (~87%, Mace *et al.*, 2007) and are extensive (e.g. Huang *et al.*, 2012a; 2012b), and exert an immediate impact on the SO energy (e.g. Haynes *et al.*, 2011) and water budget. The SO influences the atmospheric and oceanic circulation of the entire southern hemisphere and beyond. Due to this crucial influence, the U.S. National Science Foundation (NSF) Advisory Committee for Geosciences (AC GEO) named the physical processes over the SO under one of their four research frontiers for 2015–20 (NSF 2014).

The synoptic meteorology of Tasmania and the SO is mainly driven by mid-latitude cyclones (Simmonds and Keay, 2000) and their associated prevalent frontal systems (e.g. Mace 2010), which are responsible for much of the variability in the weather over this region (Trenberth, 1991). Low altitude clouds in the cold sector of the mid-latitude cyclonic storm systems are notably prominent over this region, where such systems are ubiquitous year-round. The SO is the cloudiest region on Earth having 70 – 100% of the region covered in hydrometeors according to CloudSat (Mace *et al.*, 2007). Precipitation/drizzle is frequent over the SO (Ellis *et al.*, 2009). Drizzle over the SO is also found in ~ 89% of the clouds according to the Moderate- Resolution Imaging Spectroradiometer (MODIS) observations by Bennartz (2007). Wind shear is very strong in the lower troposphere, which has complex thermodynamic and aerosol

---

structure (*e.g.* Russell *et al.*, 1998; Jensen *et al.*, 2000).

Marine stratocumulus clouds have a strong negative impact on the radiation balance of Earth whereas deep convective tropical clouds have a relatively small effect on it (Hartmann *et al.*, 1992; Chen *et al.*, 2000). Clouds modulate the radiative balance by reflecting shortwave radiation back to space but trapping out-bounding longwave radiation emitted by the Earth's surface. The response of clouds to climate change remains one of the outstanding uncertainties in making projections into the future.

Trenberth and Fasullo (2010) revealed large biases in the radiative budget over the SO in both reanalysis products and global climate models which linked directly to the clouds in this region, and these biases still exist in Coupled Model Intercomparison Project Phase 5 (CMIP5) as in Figure 1.1. The persistent bias not only limits our ability to model the SO sea surface temperature (Bodas-Salcedo *et al.*, 2016; Kay *et al.*, 2014) and ocean-atmosphere interactions, but also limits our ability to simulate the Antarctic climate (Zelinka & Hartmann, 2012) and wider climate phenomena.

The net effect of the radiative cooling and warming over this region is closely related to the low-altitude clouds, as the majority of clouds (over 50%) over the SO are low and shallow clouds extending up to 3 km (Mace *et al.*, 2007). Relatively deeper clouds, which have the bases below 3 km and tops in the range 5 - 10 km, are less prevalent over this region. The low-altitude clouds preferably occur in shallow marine boundary layers that are readily coupled by turbulent mixing to the surface moisture supply. The turbulence circulations are mainly driven by the emission of thermal infrared radiation from near the cloud tops and enhanced by latent heating in updrafts and cooling in downdrafts and entrainment at the top of the marine boundary layer. Moreover, these low-altitude clouds have a direct influence on the general circulation and significantly impact the large-scale meteorology (Bretherton and Hartmann, 2009).

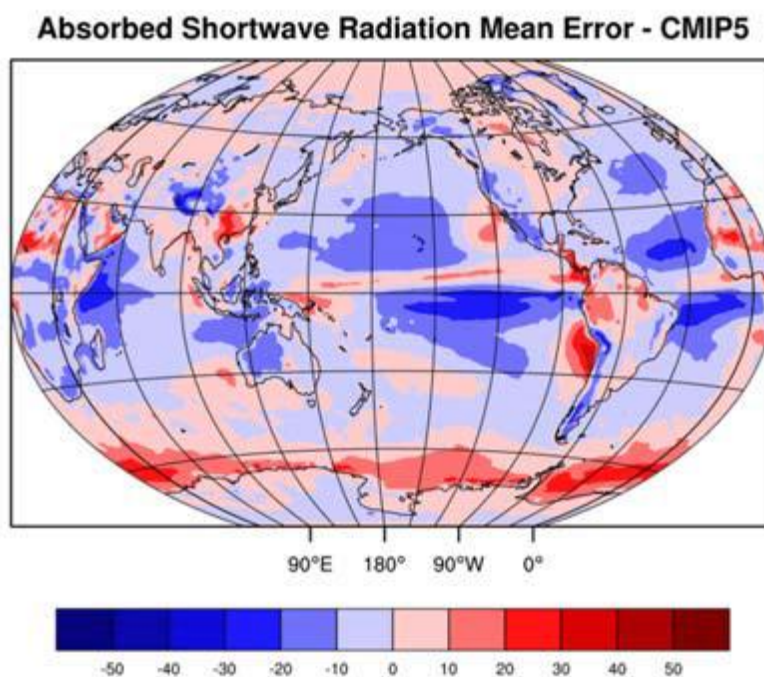


Figure 1.1. Ensemble mean error for CMIP5 model in shortwave radiation absorbed by the Earth System.

Positive values indicate too much shortwave radiation absorbed showing CMIP5 model clouds do not reflect enough sunlight (from Southern Ocean Clouds, Radiation, Aerosol Transport Experimental Study (SOCRATES) White Paper 2014)

Marine boundary layer clouds often contain light precipitation or drizzle (Pawlowska and Brenguier, 2003; Wood, 2005) and as aforementioned, over the SO, drizzle is prevalent (Bennartz, 2007). Drizzle leads to changes in the dynamics of the clouds which result in increasing mesoscale variability, stratification of the boundary layer, and finally breaking up the cloud (Wood, 2012b). Formation of drizzle involves interplay between microphysical, thermodynamic, and dynamical processes (Austin *et*

---

*al.*, 1995; Feingold *et al.*, 1996), affecting the lifetime and evolution of the clouds (Albrecht, 1993; Wood, 2000).

Cloud thermodynamic phase, a first-order cloud characteristic, affects many cloud properties and determines the ways in which clouds interact with other features of the climate system (Shupe, 2011). Liquid clouds and ice clouds have very different properties. Liquid clouds have typically been found to more strongly interact with atmospheric radiation than ice clouds (e.g., Hogan *et al.*, 2003; Shupe and Intrieri, 2004; McFarquhar and Cober, 2004), because liquid clouds have higher concentrations of smaller particles than ice clouds for a fixed amount of condensed mass (Twomey, 1977). Cloud thermodynamic phase affects microphysical processes such as collision, coalescence, aggregation and riming (Pruppacher and Klett 1997). Precipitation type and efficiency are also impacted by cloud phase (Harrington and Olsson, 2001; Zhang and Lohmann, 2003).

The clouds over the SO are predominantly comprised of super-cooled liquid water (SLW) in the low-altitude clouds as seen by MODIS and CloudSat (Morrison *et al.*, 2011; Huang *et al.*, 2012a). These clouds are significantly different from the clouds over the North Atlantic, where ice phase clouds are more prevalent (Huang *et al.*, 2015b). Similarly, the near constant presence of SLW over the SO is also found in the Cloud-Aerosol Lidar with Orthogonal Polarization (CALIOP) observations (Hu *et al.*, 2010). Later, Huang *et al.* (2016) used A-Train satellite products to highlight that the cloud properties over the SO are fundamentally different from those at comparable latitudes over the North Atlantic and North Pacific. It was found that there is a higher frequency of SLW present over the SO at colder temperatures. Further, the CALIOP backscatter revealed that the wintertime boundary layer is shallower (primarily below 1.5 km) over the SO than over the North Atlantic.

While these findings are of interest, these clouds are known to be sensitive to the

---

Hallett-Mossop process of ice multiplication (Mossop *et al.*, 1970). Chubb *et al.* (2013) also found varying thermodynamic phases in SO clouds, including ice, mixed-phase and SLW in the precipitation under SLW clouds across the span of hundreds of kilometres over the SO. Huang *et al.* (2017), in her aircraft observations, explored the potential for secondary ice production (specifically, the Hallett-Mossop process) to account for the widespread presence of mixed-phase clouds.

## 1.2 Cloud $N_d$ and $r_{eff}$ in marine boundary layer clouds dynamics

The two microphysical properties, droplet number concentration ( $N_d$ ) and effective radius ( $r_{eff}$ ), are primary parameters affecting cloud physical processes and cloud optical characteristics (Gultepe and Issac, 2004), and they are needed for radiative transfer calculations. Cloud  $N_d$  and  $r_{eff}$  in marine low-altitude clouds are the primary determinants of the ability to reflect solar radiation and to modulate precipitation (Wood, 2012b).  $N_d$  and  $r_{eff}$  of low-altitude clouds are sensitive to the concentration of aerosol particles on which cloud droplets form and therefore anthropogenic pollution. Polluted clouds tend to contain higher  $N_d$  and smaller  $r_{eff}$ , greater cloud albedo, and less drizzle in the same cloud thickness.

Figure 1.2 provides a conceptual diagram detailing the internal feedbacks that influence the macrophysical and microphysical properties. The major regulating feedback depicted by thick arrows shows the relationship between the cloud, radiation, turbulence and entrainment. The cloud thickness ( $h$ ), liquid water path (LWP), and cloud cover ( $f_c$ ), and precipitation all directly or indirectly affect the cloud droplet number concentration ( $N_d$ ). Precipitation can be suppressed by increasing  $N_d$  which is increased by aerosol concentration provided by outside sources.

An increase in  $N_d$  can also decrease the condensation time scale (by increasing the

overall droplet surface area), which increases TKE by increasing the liquid water flux (Wang *et al.*, 2003). This microphysically limited condensation is more acute for low droplet concentration  $N_d$ , such as in the clouds over the SO, because the equilibrium supersaturation is inversely proportional to  $N_d$  (Squires, 1952; Kogan *et al.*, 1995). Increasing  $N_d$  can also decrease the sedimentation rate of cloud droplets although this does not have a major impact throughout the body of the cloud because the sedimentation rates of clouds droplets are relatively very low.

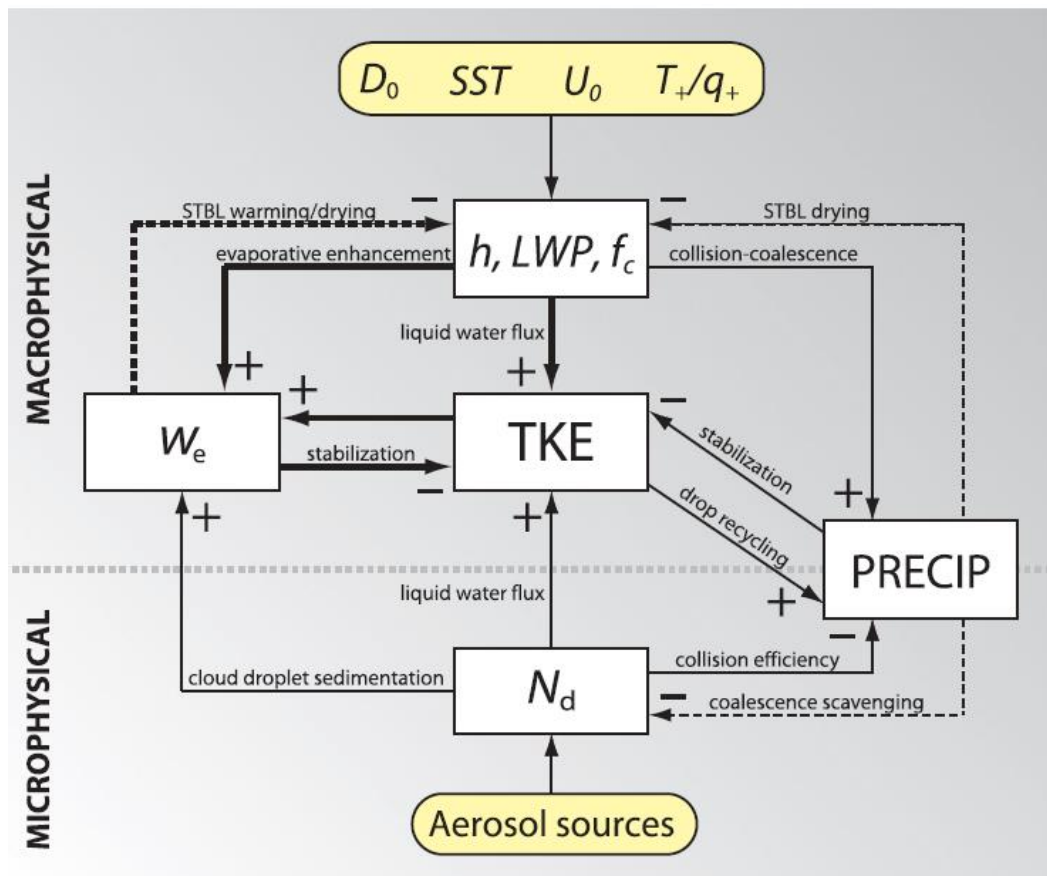


Figure 1.2. Conceptual system dynamics diagram illustrating important feedbacks related to the macrophysical and microphysical properties of stratiform top boundary layer (STBL).

The feedbacks serve to regulate the thickness  $h$ , liquid water path  $LWP$ , and cloud cover  $f_c$  of stratocumulus clouds. Yellow rounded rectangles show external meteorological

---

and aerosol parameters: surface divergence  $D_0$ , sea surface temperature SST, surface wind speed  $U_0$ , free-tropospheric temperature  $T_+$  and humidity  $q_+$ , and aerosol sources. White boxes show key internal variables: TKE represents a measure of the strength of the TKE within the BL;  $W_e$  is the cloud-top entrainment rate; PRECIP is a measure of the precipitation rate; and  $N_d$  is the cloud droplet concentration, which is the key microphysical variable that can influence macrophysical processes. Plus and minus signs indicate positive and negative impacts of one variable on another, with the key physical processes accompanying the arrows. Thick arrows indicate the cloud–radiation–turbulence–entrainment feedback system that constitutes a dominant negative feedback regulating stratocumulus thickness and cover. Solid lines indicate feedbacks that operate on time scales comparable with the eddy turnover time scale (typically an hour or less), while dashed lines indicate feedbacks that operate on markedly longer time scales. The thick dotted gray line is used to separate the chart into (top) macrophysical and (bottom) microphysical variables, with precipitation straddling the boundary between the macrophysical and microphysical realms (from Wood, 2012a).

Clouds over the SO in a pristine environment, remote from anthropogenic aerosol sources (e.g. Yum and Hudson, 2004; Gras, 1995) have unique microphysical properties. They have been reported in the literature to have the lowest  $N_d$  and biggest  $r_{eff}$  in the world (Boers *et al.*, 1996). On the other hand, Mace *et al.* (2007) found the microphysical conditions of these low-altitude clouds are suggested to show little variability over the entire region. Wood *et al.* (2012) developed an idealized model of  $N_d$  for maritime boundary layer clouds and found that precipitation was a principal driver of  $N_d$ , more so than CCN below the cloud base. Employing numerical simulations, McCoy *et al.* (2015) concluded that over 50% of the observed spatiotemporal variability in  $N_d$  over the SO was tied to sources of natural aerosols. Specifically, variability in  $N_d$  was ‘driven primarily by high concentrations of sulphate aerosols at lower latitudes (35° to 45°S) and by organic matter in the sea spray aerosols at higher latitudes (45° to 55°S)’.

---

### 1.3 Past field campaigns on the SO clouds and drizzle

Compared to the campaigns for the Northern Hemisphere, those for the SO are relatively sparse primarily due to its remote location and harsh operating conditions such as strongest annually-averaged mean surface wind speed on earth (Vinoth and Young, 2011) and heavy icing on the aircraft with high supercooled liquid water (SLW, Morrison *et al.*, 2011; Huang *et al.*, 2012a).

One of the first campaigns over the SO was the several research flights by Mossop *et al.* (1970) to investigate cloud microphysical processes. One hundred and fourteen small supercooled cumulus clouds were studied in May 1968 over the ocean off the Tasmanian coast. There was a 50 % chance of the clouds containing crystal particles when cloud top temperature was around  $-8^{\circ}\text{C}$ . In addition to identifying the various stages in the glaciation process, an ice multiplication process associated with the riming of ice was found. Later Mossop (1985) identified the detailed structure of a secondary ice “multiplication” mechanism.

Later, Southern Ocean Cloud EXperiments (SOCEX I and II; Boers *et al.*, 1996; 1998) were conducted off the west coast of Tasmania, Australia. The two SOCEX campaigns were made to investigate the variability of the microphysical and radiative properties of stratocumulus clouds in unpolluted background air. Four flights (excluding one flight done under non-baseline conditions) over three days were conducted during the SOCEX I (Boers *et al.*, 1996) in 11-20 July, 1993 for winter time and six flights over three days during the SOCEX II (Boers *et al.*, 1998) in 1 – 9 Feb, 1995 for summer time over the Southern Ocean near the north-west coast of Tasmania, Australia.

The droplet number concentration ( $N_d$ ) from winter time was found to be among the lowest ever recorded,  $10 - 40 \text{ cm}^{-3}$  for clouds of up to 300 m deep for winter time and

---

50 - 180 cm<sup>-3</sup> for summer time. The droplet concentration generally decreased with altitude, indicating the importance of droplet collision and coalescence in reducing the number of large cloud droplets. Drizzle was observed on three of the four flights. The results from SOCEX I and II show large differences in  $N_d$  between summer and winter (three times higher in summer). The high  $N_d$  in summer suggests a natural cause, a hypothesis being oxidation products of oceanic dimethylsulphide acting as cloud condensation nuclei, known as the CLAW hypothesis (Charlson *et al.*, 1987; Ayers and Cainey, 2007; Vallina and Simo, 2007), which takes the first letter of the surname of the hypothesis authors. The CLAW hypothesis details the role of dimethyl sulfide produced by phytoplankton which biogenic activity is more intense during the summer. Yum and Hudson (2004) studied the Cloud Condensation Nuclei (CCN) differences between summer and winter and found the CCN concentrations in summer is higher by an order of magnitude than in winter, which is consistent with the surface observations by Gras (1995) made at the Cape Grim Baseline Air Pollution Station located in northwest Tasmania. Quinn and Bates (2011), however, recently argued against the CLAW hypothesis, highlighting that the dimethyl sulphide biological control over cloud condensation nuclei probably does not exist and that sources of these nuclei in the marine boundary layer and the response of clouds to changes in aerosol are much more complex than was recognized twenty years ago.

Another comprehensive SO experiment, the Aerosol Characterization Experiment (ACE-1; Bates *et al.*, 1998) was conducted in November and December of 1995 south of Australia. ACE-1 quantified the chemical, physical, radiative, and cloud nucleating properties of aerosols and furthered our understanding of the processes controlling the aerosol properties in this minimally polluted marine atmosphere. While the National Center for Atmospheric Research (NCAR) C-130 aircraft used for the ACE-1 avoided flying in low-altitude clouds, it was found that some of the low-altitude clouds resided above a shallow boundary layer of 500 – 700 m deep in a “buffer layer” below the free troposphere (Russell *et al.*, 1998; Wang *et al.*, 1999). Consistently, Jensen *et al.* (2000)

---

also identified a subsaturated layer below the stratiform clouds called an intermediate layer, capped by the free troposphere.

Although there have been few recent *in-situ* observations, a fresh opportunity to examine the clouds over the SO was provided by the HIPPO (High-performance Instrumented Airborne Platform for Environmental Research (HIAPER) Pole-to-Pole Observations) campaign (Wofsy *et al.*, 2011) at latitudes as high as 67°S. Using the HIPPO missions, Chubb *et al.* (2013) studied the variability of  $N_d$  in April, observing  $N_d$  (30 – 50 cm<sup>-3</sup>) near 59°S and  $N_d$  (80 – 120 cm<sup>-3</sup>) at higher latitudes in weakly convective stratocumulus in the cold air sector of an extratropical cyclone. However, later in a wintertime HIPPO flight, Chubb *et al.* (2016) found that the highest  $N_d$  of 100 – 200 cm<sup>-3</sup>, which is inconsistent to the record from SOCEX I. For this high  $N_d$ , it was hypothesized that gale force pre-frontal winds enhanced the concentration of sea spray aerosols, which in turn contributed to the substantial enhancement of  $N_d$ . Another case of high variability of  $N_d$  was identified by Huang *et al.* (2015a). In their two wintertime case studies, the  $N_d$  varied from 30 – 90 cm<sup>-3</sup> when there were no nearby gale-force winds.

It is extremely challenging to understand the processes controlling the phase and precipitation of the clouds over the SO, the majority of which have a cloud-top temperature range from -30 °C to 0 °C (Huang *et al.*, 2012a; 2015b). In the HIPPO campaign, Chubb *et al.* (2013) revealed high quantities of supercooled liquid water (up to 0.47 gm<sup>-3</sup>) in clouds as cold as -22 °C during two flights in different seasons and different meteorological conditions. In addition, precipitation under the SLW was in various thermodynamic phases such as glaciated, mixed-phase or entirely supercooled liquid. The complexity of clouds over the SO was further highlighted by Huang *et al.* (2017) who observed mixed-phase (but predominantly supercooled liquid water) clouds at cloud-top temperatures around -6 °C during a research flight around the coast of Tasmania in 2013.

---

## 1.4 Satellite observations of the SO clouds and drizzle

Satellite observations with advances in spaceborne instrumentation have helped diagnosing cloud microphysical properties and their link to cloud radiative properties (e.g. Mace 2010; Bennartz 2007; Stephens *et al.* 2002). Nakajima and King (1990) estimated cloud **droplet effective radius** by using the satellite spectral signature of the cloud solar reflectance. This methodology has been used to derive a near-global climatology of the droplet effective radii of liquid clouds observed by Advanced Very High Resolution Radiometer (AVHRR) instruments (Han *et al.*, 1994) carried by the National Oceanic and Atmospheric Administration (NOAA)-9 (“afternoon”) and NOAA-10 (“morning”) polar orbiting platforms. AVHRR measures the radiance from the clouds on Earth in five spectral bands and the data are available from the International Satellite Cloud Climatology Project (ISCCP).

A global survey of cloud particle size variations reveals systematic differences between continental and ocean areas and between hemispheres, indicating differences in aerosol concentration. Continental water clouds have 2 - 3  $\mu\text{m}$  smaller droplet radii than marine clouds and maritime clouds of the Northern Hemisphere are 1  $\mu\text{m}$  smaller than those in the Southern Hemisphere. For example, the winter time  $r_{eff}$  of ocean clouds in the Northern Hemisphere is 10.2  $\mu\text{m}$  while that of Southern Hemisphere is 11.6  $\mu\text{m}$ . Uncertainties and biases from satellite observations on cloud are examined through numerous validation projects including intercomparisons against *in-situ* observations. The main sources of bias in the estimates are due to cloud field heterogeneity (especially in the vertical direction) and the reflectance of the underlying surface (Platnick and Valero, 1995; Breon and Doutriaux-Boucher, 2005; Nakajima *et al.*, 2010a; Marchand *et al.*, 2007; Huang *et al.*, 2012a)

Breon and Colzy (2000) estimated the global distribution of cloud droplet effective radius from Polarization and Directionality of the Earth Reflectance polarization

---

(POLDER, Deschamps *et al.*, 1994), which was launched on board the Advanced Earth Observing Satellite (ADEOS) in August 1996. The POLDER instrument provided a fresh opportunity for estimating the effective radius from space based on the directional signature of polarized solar light reflected by clouds (Breon and Goloub, 1998). The POLDER measurements require very specific conditions; for example, the cloud field must have homogeneous microphysical properties over an area of about  $150 \times 150 \text{ km}^2$ . Although the global distributions may not be representative of all liquid clouds, the results are broadly consistent with the results of Han *et al.* (1994). However, the studies of both Han *et al.* (1994) and Breon and Colzy (2000) have limited results at latitudes lower than  $45^\circ$  in wintertime due to high solar zenith angles.

Estimates of global cloud properties from existing meteorological instruments are limited by the precision and spectral coverage of those instruments. New instruments with better calibration and more spectral frequencies have been providing unprecedented opportunities to understand clouds and their role in climate. Moderate Resolution Imaging Spectroradiometer (MODIS; Platnick *et al.*, 2003) is a scientific instrument on board the Terra (EOS AM) Satellite and the Aqua (EOS PM) satellite launched into Earth orbit by NASA in 1999 and 2002 respectively. MODIS data provide much better calibration and spectral resolution than former meteorological satellites (King *et al.*, 2003). The wide swath width of 2330 km of MODIS allows nearly complete global coverage every two days at an altitude of 705 km, and 26 bands are used to derive atmospheric properties such as cloud mask, atmospheric profiles, aerosol properties, total precipitable water, and cloud properties.

Bennartz (2007) derived cloud droplet number concentration ( $N_d$ ) and cloud geometrical thickness from the MODIS level 3 data of cloud effective radius and optical thickness under the assumption of adiabatically stratified clouds. The results are consistent with previous studies, finding the mean  $N_d$  of the stratiform boundary layer clouds over remote Northern Hemisphere oceans is higher than over the Southern

---

Oceans ( $64 - 89 \text{ cm}^{-3}$  in the Northern Hemisphere and  $40 - 67 \text{ cm}^{-3}$  in the Southern Hemisphere). He also investigated the sensitivity of the  $N_d$  to drizzling, concluding that  $N_d$  in non-drizzling clouds was about 2.5 times higher than that in drizzling clouds.

The seasonal cycle of  $N_d$  over the SO suggested by Boers *et al.* (1996; 1998) is also found in the MODIS retrievals as shown in Figure 1.3, but the seasonal cycle remains an open question due to the lack of assessments of satellite products against *in-situ* observations and limited winter observations.

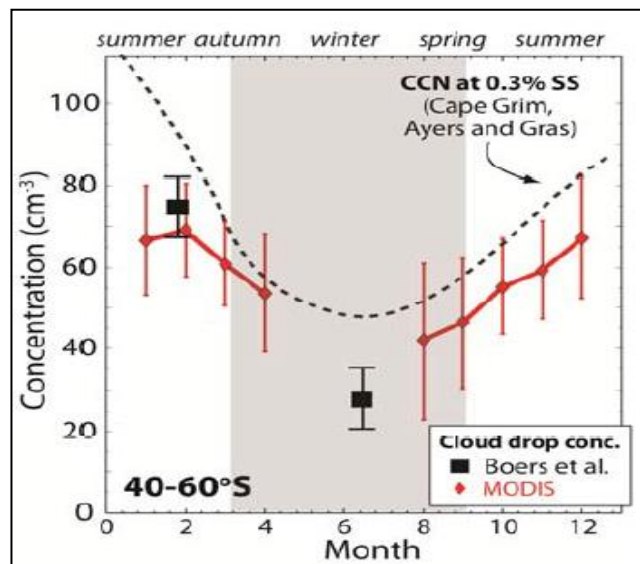


Figure 1.3. Seasonal cycles of cloud drop concentration ( $N_d$ ) and CCN concentration over the Southern Ocean.

$N_d$  data are derived from passive visible/near-IR data from MODIS (red) and from limited aircraft flights during winter and summer (black squares). The seasonal cycle of CCN at 0.3% supersaturation from measurements at Cape Grim (Ayers and Gras 1991) is also shown, as are  $N_d$  measurements from SOCEX campaigns (from SOCRATES White Paper, 2014).

---

The Cloud-Aerosol Lidar with Orthogonal Polarization (CALIOP, Winker *et al.*, 2007), a light detection and ranging (lidar) instrument on board CALIPSO, provides high-resolution vertical profiles of aerosols and clouds. CALIOP is a two-wavelength (532 nm and 1064 nm) polarization-sensitive lidar. It has three receiver channels: one measuring the 1064-nm backscattered intensity, and two channels measuring orthogonally polarized components (parallel and perpendicular to the polarization plane of the transmitted beam) of the 532-nm backscattered signal. Its footprint at the Earth's surface (from a 705-km orbit) is about 90 meters and vertical resolution of 30 meters (actual nominal resolution is ~15 m vertical and 333 m horizontal). Measurements of clouds with CALIOP give unprecedented detail on vertical cloud structure particularly showing how clouds are layered vertically, which was not possible with visible, infrared, or microwave passive instruments. The lidar in space can provide very sensitive measurements of thin layers of clouds or aerosols (Winker, 1997).

The CALIPSO lidar is used in the present study to qualitatively compare the cloud thermodynamic phase from aircraft observations with the newly-improved MODIS cloud phase infrared (CPI) and cloud phase optical properties (CPOP) retrievals.

The CloudSat (Im *et al.* 2005) Cloud Profiling Radar (CPR) on board CloudSat, which launched in 2006 as part of the A-Train constellation (Stephens *et al.*, 2002) with Aqua and CALIPSO, is a near-nadir pointing millimeter-wavelength (94 GHz, W-band) radar system. Measuring the power backscattered by clouds as a function of distance from the radar, the CPR provides good vertical resolution of reasonably thick clouds, including the tops and bottoms of layered clouds (Stephens *et al.*, 2002).

Drizzle is frequently observed in maritime clouds (Zanten and Stevens, 2005; Pawlowska and Brenguier, 2003; and Wood, 2005). According to the CPR precipitation product (2C-COLUMNPRECIP; Haynes *et al.*, 2009), a peak in the precipitation frequency was observed between 50° and 60°S over the global oceans, and much of the

---

precipitation was classified as ice or mixed phase (Ellis *et al.*, 2009). In addition, low-intensity precipitation over the SO is found to be dominant from the second CloudSat precipitation product (2C-RAIN-PROFILE; Mitrescu *et al.*, 2010), commonly with a frequency in excess of 15%. Meanwhile, Stephens *et al.* (2010) showed that the precipitation frequency from global numerical models is approximately twice that from the CPR, with the intensity being correspondingly weaker.

---

## 1.5 Aims summary

From the above discussion, the following major research questions associated with the SO clouds are arisen:

- What is the natural variability of  $N_d$  and  $r_{eff}$  of wintertime cloud over the Southern Ocean? Are they sensitive to the synoptic meteorology?
- How frequently is drizzle detected in the liquid clouds and does this drizzle affect the cloud  $N_d$  and  $r_{eff}$ ? How frequently is ice and mixed phase detected in the wintertime clouds over the SO?
- Can we use these observations to evaluate/appreciate satellite products (MODIS and CALIPSO) over the SO?

To address those question, *in-situ* observations of cloud microphysical porperties over the SO were made off the west, south and east coast of Tasmnia under various synoptic and local meterology. The *in-situ* observations consist of 20 cloud seeding operational flights and research flights and the research flights are employed to evaluate the satellite products.

The aims of the present thesis are summarized by chapter below:

### Chapter 2

To develop more representative microphysical and thermodynamic properties of wintertime low-altitude clouds over the SO than that from SOCEX I based on new aircraft observations.

### Chapter 3

To establish the sensitivity of the cloud microphysical properties ( $N_d$ ,  $r_{eff}$  and LWC) and the cloud thermodynamic phase to the synoptic and local meteorology (including drizzle).

---

(The research presented in chapter 2 and 3 has been published by Q. J. R. Meteorol. Soc, Volume 143, 2017. The research results from the *in-situ* observations of 20 flights during 2013 – 2015. )

#### **Chapter 4**

To evaluate satellite products, Moderate Resolution Image Spectroradiometer (MODIS) for cloud thermodynamic phase and microphysical properties and Cloud-Aerosol Lidar and Infrared Pathfinder Satellite Observations (CALIPSO) for cloud thermodynamic phase with our new *in-situ* observations.

(The research in chapter 4 is a complete manuscript submitted to a journal. The research analysed the 11 flights coincided with A-Train constellation out of the 20 flights studied in chapter 2 and 3.)

#### **Chapter 5**

To evaluate satellite products, Global Precipitation Measurements (GPM) and CloudSat for precipitation frequency and intensity (rain rate) with our new *in-situ* observations.

(The research in chapter 5 presents preliminary results as the GPM observations are limited due to the unavailability of essential Ku/Ka-band radar.)

---

## Chapter 2

# Clouds Thermodynamic and Microphysical Properties by *In-situ* Observations



Figure 2.0 The Cessna Conquest aircraft hired by Hydro Tasmania and used for in-situ observations.

The natural variability of  $N_d$  and  $r_{eff}$  for SO clouds remains poorly understood due primarily to limited *in-situ* observations. This work presents *in-situ* observations of the microphysical properties of pristine SO clouds from 20 flights over the open ocean around Tasmania, Australia, taken over the course of three winters (2013-2015). Unlike SOCEX I, observations have been made under a variety of meteorological conditions. In this chapter, cloud thermodynamic phase,  $N_d$  and  $r_{eff}$  from 20 flights are closely investigated in association with synoptic and local meteorology.

---

## 2.1 Flight overview and instrumentation

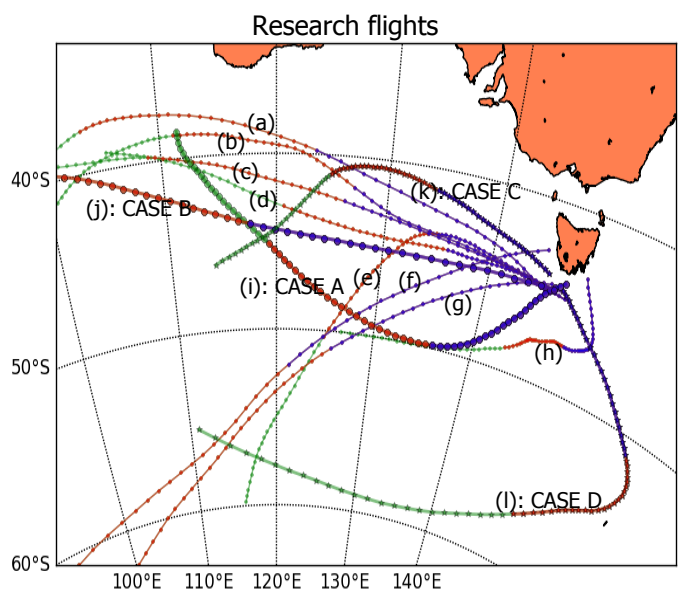
### 2.1.1 Flight overview

*In-situ* observations of SO clouds have been made during 20 flights of June – October, 2013 - 2015 from a lightly instrumented Cessna Conquest employed by Hydro Tasmania Ltd. (Huang *et al.*, 2014, 2015a). The analysis is limited to in-cloud observations located over the open ocean (43 – 45°S, 145 – 148°E), upwind of Tasmania. These clouds must not have been influenced by any upwind terrestrial sources of aerosols for a minimum of three days as examined with standard back-trajectory calculations (Figure 2.1) made with the Hybrid Single Particle Lagrangian Integrated Trajectory (HYSPLIT) model (Draxler and Hess 1998) employing the Global Data Assimilation System (GDAS) reanalysis. We refer to such conditions as being ‘pristine’ and are comparable to the ‘baseline’ conditions observed at the Cape Grim Baseline Air Pollution Station (CGBAPS) (e.g. Yum and Hudson, 2004; Gras, 1995), only the wind heading is not strictly constrained due to orography as it is for the fixed site of CGBAPS.

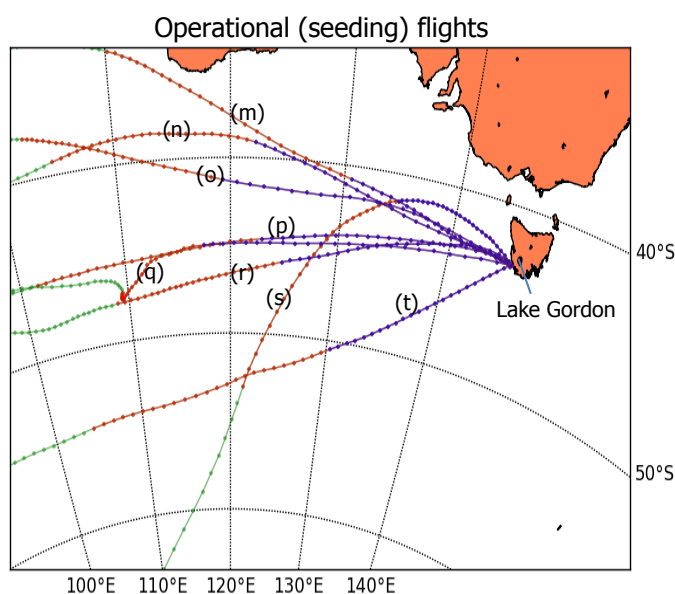
Twelve of 20 flights were ‘research-only’ flights, fully dedicated to observing ‘pristine’ SO cloud microphysics. These flights were constrained to coincide with A-Train overpasses, when the aircraft was not being used by Hydro Tasmania for operational cloud seeding (e.g. Morrison *et al.*, 2013, 2010). The remaining eight flights were comprised of ‘pristine’ segments of select operational cloud seeding flights. While the vast majority of cloud seeding flights were not suitable for this analysis, on very limited occasions the Cessna Conquest flew upwind of any seeding activity, over the open ocean, to collect unperturbed samples that would be suitable for other research activities (e.g. initialising numerical simulations). These pristine segments often consisted of ferrying out over the water to a point off the coast at which point a sounding was undertaken. More detailed descriptions of cloud seeding flights are found in the

appendix.

## Flight Locations and Air mass Back Trajectories



(a) 20130815\_1224 (e) 20130707\_1259 (i) 20130723\_1302  
(b) 20131011\_1324 (f) 20130806\_1513 (j) 20151001\_1230  
(c) 20140912\_1243 (g) 20130907\_1224 (k) 20130628\_1301  
(d) 20140903\_1243 (h) 20130614\_1336 (l) 20150830\_1305



(m) 20130921\_1133 (q) 20140806\_1508  
(n) 20131011\_0749 (r) 20150804\_1219  
(o) 20130803\_0844 (s) 20130707\_0737  
(p) 20130702\_1011 (t) 20140630\_0708

Figure 2.1. Seventy-two hour Hybrid Single Particle Lagrangian Integrated Trajectory Model (HYSPLIT) back trajectories for 20 flights of three consecutive winters (Jun - Oct, 2013 - 2015) with the Global Data Assimilation System (GDAS) reanalysis.

---

The upper panel is for research flights and the lower panel for operational (seeding) flights. The flights dates are indicated by the letter on the trajectory line. The calculation of each back trajectory was initialised for the average altitude of the samples for the flight. The colouring of each back trajectory changes for each 24h period. The two non-drizzling cases (CASES A and B) are indicated by a reddish colour with big circle marks, while the two heavily drizzling cases (CASES C and D) are indicated by a reddish colour with star marks.

We have included the pristine segments from these eight flights, as they satisfy our criteria and thus extend the observations under more various meteorology. The inclusion of these data does, however, introduce another sampling bias towards conditions suitable for operational cloud seeding. In Table 2.1 we examine this potential bias, finding no substantial difference in cloud effective radius or droplet number concentration between cloud seeding and research-only missions. It is further noted that seeding was not even undertaken in two of these eight cloud seeding flights. Further details of cloud seeding flights are described in the section of ‘Cloud seeding flights’ in the appendix.

All data are recorded and analysed at a temporal resolution of 1 Hz, which corresponds to a spatial scale of approximately 100 m based on the typical aircraft true air speed. The 20 flights analysed (Table 2.1) comprise a total of 20,357 one-second cloud samples. The flights of 14 June 2013 and 23 July 2013 have previously been presented in Huang *et al.* (2015a).

Table 2.1. Summary of synoptic conditions and thermodynamic and cloud microphysical properties for each flight for winter time during 2013-2015.

Flight Date/ Category	Type <sup>1)</sup>	Flight Location	Front association <sup>2)</sup>	Cloud Type <sup>3)</sup>	Pressure [hPa]	Cloud Base <sup>4)</sup> [km]	Cloud Top <sup>4)</sup> [km]	Wind Direction [°]	Time in Clouds [sec]	Liq Fraction [%]	Mxd Fraction [%]	Ice Fraction [%]	Temperature [°C]	$N_d$ [cm <sup>-3</sup> ]	$r_{eff}$ [μm]	$r_{eff}$ (CAS+CIP) [μm]	LWC (CAS) [gkg <sup>-1</sup> ]	LWC (CAS+CIP) [gkg <sup>-1</sup> ]	Drizzle [%]	RainRate [mmhr <sup>-1</sup> ]
20130803_084439	O <sup>5)</sup>	SW	Prefrontal	No MCC	683	2.5	3.8	261	541	19%	79.1%	1.7%	-10.8 ( -11.2 to -10.3 )	7	12.3	31.5	0.034	0.234	89%	0.328
20130707_125944	R	S	Prefrontal	Open MCC	915	0.5	1.0	274	2022	10%	89.6%	0.7%	-0.1 ( -9.3 to 4.0 )	11	13.7	56.3	0.093	0.305	59%	3.667
20150830_130524	R	S	Not associated Near front (~50km)	Open MCC	867	0.7	1.5	151	1754	98%	1.6%	0.0%	0.5 ( -4.7 to 4.2 )	13	13.2	35.9	0.079	0.390	91%	0.957
20131011_074911	O	W		No MCC	853	0.7	1.5	276	266	91%	3.8%	5.6%	2.1 ( -0.8 to 7.6 )	13	13.6	16.9	0.076	0.112	60%	0.112
20130707_073753	O <sup>5)</sup>	W	Prefrontal	Open MCC	766	1.6	2.3	320	377	32%	50.4%	17.2%	-10.3 ( -13.2 to 6.7 )	15	15.4	20.6	0.155	0.234	49%	0.363
20140630_070840	O	W	Prefrontal	Not identified	693	N/A	N/A	259	899	50%	46.8%	3.1%	-9.5 ( -10.3 to -8.4 )	15	13.4	14.2	0.105	0.120	5%	0.046
20150804_121910	O	W	Prefrontal	Open MCC	667	N/A	N/A	279	496	14%	80.2%	5.6%	-11.0 ( -12.0 to -9.6 )	17	14.0	15.8	0.140	0.184	27%	0.267
20130815_122404	R	SW	Ridge	Disorganiz ed MCC	778	0.9	2.0	302	1380	65%	35.1%	0.0%	-4.5 ( -6.9 to 5.6 )	18	11.2	11.3	0.072	0.076	10%	0.007
20130702_101141	O	W	Near front (~120km)	No MCC	853	1.0	2.1	275	1728	35%	55.3%	9.9%	0.1 ( -7.3 to 4.9 )	19	14.2	45.6	0.137	0.422	83%	3.250
20140903_124321	R	S,SW	Ridge	Open MCC	801	1.2	2.0	224	694	70%	29.3%	0.7%	-2.3 ( -9.2 to 7.4 )	21	14.0	19.0	0.173	0.231	37%	0.412
20130628_130139	R	SW	Ridge	Open MCC	871	0.7	1.6	194	1338	93%	6.7%	0.0%	-0.6 ( -4.5 to 8.0 )	21	14.2	23.3	0.190	0.306	85%	0.441
20140912_124317	R	S	Not associated	Open MCC	809	1.4	1.9	264	1433	69%	29.2%	1.4%	-1.2 ( -11.4 to 5.0 )	21	14.0	18.8	0.195	0.388	47%	3.160
20130614_133658	R	SE	Not associated Near front (~50km)	Open MCC	882	1.0	1.4	145	1201	99%	1.4%	0.0%	0.0 ( -5.2 to 2.6 )	23	13.1	20.3	0.159	0.275	62%	1.002
20140806_150804	O	W	Near front (~400km)	No MCC	666	2.0	3.3	264	556	9%	90.8%	0.0%	-8.6 ( -9.4 to -7.8 )	28	12.1	15.2	0.169	0.217	34%	0.496
20130921_113331	O	W		No MCC	656	2.2	2.5	257	189	88%	12.2%	0.0%	-8.4 ( -10.1 to -2.1 )	28	9.8	9.5	0.101	0.101	0%	0.0
20131011_132432	R	S	Postfrontal	Disorganiz ed MCC	804	0.7	2.4	273	1904	82%	16.6%	0.9%	-1.3 ( -25.2 to 8.4 )	29	11.2	21.3	0.130	0.219	44%	1.112
20130907_122442	R	SW	Postfrontal	Open MCC	804	0.6	1.9	257	1742	49%	51.0%	0.0%	-6.4 ( -10.9 to 5.8 )	34	13.2	24.0	0.257	0.422	58%	1.788
20130806_151347	R	W	Postfrontal	Open MCC	810	1.0	2.5	249	355	95%	5.4%	0.0%	-6.0 ( -13.6 to -2.7 )	40	11.3	12.2	0.201	0.202	0%	0.0
20151001_123025	R	S	Postfrontal	Closed MCC Stratiform closed	779	1 3.4	1.8 4.3	260	803	68%	32.0%	0.2%	-1.6 ( -18.7 to 9.1 )	80	8.5	8.5	0.172	0.173	4%	0.007
20130723_130219	R	S	Ridge		904	0.8	1.2	183	679	100%	0.0%	0.0%	-0.1 ( -3.2 to 4.0 )	89	8.2	8.2	0.165	0.165	0%	0.0
Research Flights	-	-	-	-	-	-	-	-	15305	70%	29.6%	0.4%	-	33	12	22	0.157	0.263	51%	1.046
Operational Flights	-	-	-	-	-	-	-	-	5052	36%	58.0%	6.3%	-	18	13	21	0.114	0.203	47%	0.608
Closed MCC	-	-	-	-	-	-	-	-	1482	83%	17.3%	0.1%	-	84	8	8	0.169	0.169	2%	0.004
Open MCC	-	-	-	-	-	-	-	-	11412	63%	35.6%	1.2%	-	21	14	25	0.164	0.294	65%	1.206
Disorganised MCC	-	-	-	-	-	-	-	-	3284	75%	24.4%	0.5%	-	23	11	16	0.101	0.148	31%	0.559
No MCC	-	-	-	-	-	-	-	-	3280	35%	58.6%	5.9%	-	19	12	24	0.103	0.217	65%	0.837
Total (mean)	-	-	-	-	-	-	-	-	20,357	61.5%	36.7%	1.8%	-	27	12.5	21.4	0.140	0.239	49%	0.733

---

<sup>1)</sup> Flight type: R (Research), O (Operational) <sup>2)</sup> Approximate distance from the front is indicated in the parenthesis <sup>3)</sup> Cloud type: MCC (Mesoscale cellular convection) <sup>4)</sup> Approximate bounds from soundings, when available. Note that the cloud fields were not horizontally homogeneous, and multiple layers commonly were observed <sup>5)</sup> No seeding activities were conducted.

---

## 2.1.2 Aircraft instrumentation

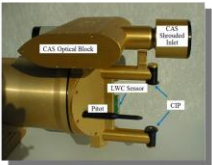
Ambient and dew point temperatures are measured with a Meteolabor TP-3S (Meteolabor AG, Switzerland) mounted inside a reverse-flow housing to protect the instrument from hydrometeors.  $N_d$  and  $r_{eff}$  of liquid water clouds derived from measurements with a Droplet Measurement Technologies (DMT) Cloud, Aerosol and Precipitation Spectrometer probe (CAPS: Baumgardner *et al.*, 2001), which consisted of a hot-wire liquid water sensor (LWC-100), a Cloud Aerosol Spectrometer (CAS) that measures particles from 0.5 to 50  $\mu\text{m}$ , and a Cloud Imaging Probe (CIP) that is used for larger particles from 25  $\mu\text{m}$  to 1.55 mm. For all the calculations, we omit the measurements from the first three bins of the CAS (bin sizes less than  $\sim 0.68 \mu\text{m}$ ) and the first two bins of the CIP (bin sizes less than  $\sim 62.5 \mu\text{m}$ ) given the high uncertainties in the measurements.

For the CIP data processing, the ‘System for Optical Array Probe Data Analysis (SODA)’ software developed at the National Center for Atmospheric Research (NCAR) was used. We note that the DMT CAPS was not equipped with Korolev anti-shattering tips (Korolev *et al.*, 2013) for all flights during 2013. As such, a shattering correction (Korolev, 2007), was applied with the SODA software to remove any potential shattered ice particles or artifacts due to splashing of precipitation drops on the tips. The details of the CIP data processing including the ‘water processing’ and ‘shattering correction’ are described in the appendix.

Bulk liquid and total water concentrations were also measured with a Science Engineering Associates Inc. (SEA) WCM-2000 Multi Element Water Content System (Lilie *et al.*, 2005). The WCM-2000 has two independent hot-wire elements (0.5 and 2 mm) in diameter for liquid water content (LWC) and a scooped 4 mm element for total water (ice + liquid) content (TWC). These three instruments are conventionally called

the LWC021, the LWC083 and the TWC156, respectively. Measurement uncertainties and limitations of the WCM-2000 are described in ‘Error estimates’ section in the appendix. The instruments are summarized in Table 2.2.

Table 2.2. The major instruments used for the research and their ranges for measurements.

<i>Composition</i>	<i>Range</i>
<ul style="list-style-type: none"> <li>• CAPS (Cloud Aerosol &amp; Precipitation Spectrometer)</li> </ul>  <ul style="list-style-type: none"> <li>• <b>CAS</b> (Cloud &amp; Aerosol Spectrometer)</li> <li>• <b>CIP</b> (Cloud Imaging Probe)</li> <li>• <b>LWC-100</b> (Hotwire Liquid Water Content Sensor)</li> </ul>	<ul style="list-style-type: none"> <li>0.5~50 <math>\mu\text{m}</math></li> <li>12.5~1550<math>\mu\text{m}</math></li> <li>0.01~3 <math>\text{g}/\text{m}^3</math></li> </ul>
<ul style="list-style-type: none"> <li>• WCM-2000 Multi-Element Water Content System</li> </ul>  <ul style="list-style-type: none"> <li>• TWC156 (Scoop shaped)</li> <li>• LWC 083 (2mm)</li> <li>• LWC 021 (0.5mm)</li> <li>• Derived IWC = TWC - LWC</li> </ul>	<ul style="list-style-type: none"> <li>0~10 <math>\text{g}/\text{m}^3</math></li> </ul>

In this study, cloud was defined by a total water content (TWC) threshold of  $0.01 \text{ gm}^{-3}$  (Korolev *et al.*, 2003; Wood and Field 2011; Boutle *et al.*, 2014) as measured by the TWC156 and the CAPS (CAS + CIP). Following Korolev *et al.* (2003), liquid water clouds were separated from mixed phase and ice clouds when the ice-water fraction,  $\mu_3$ , was less than 0.1 with  $\mu_3$  defined as  $W_{ice} / (W_{liq} + W_{ice})$  with liquid water content ( $W_{liq}$ ) and ice water content ( $W_{ice}$ ) derived from measured LWC and TWC from the LWC083 and TWC156. Calculation of liquid and ice water content is described in detail in ‘Error estimates’ section in the appendix. Calculations of ice water content (IWC) using LWC and TWC hot-wire instruments have been used in many studies (Mazin *et al.*, 1992; Korolev and Isaac 1998, 2000; and Cober *et al.*, 2000, 2001).

---

Quality control of the thermodynamic data (e.g. pressure, temperature and humidity) was performed. Several independent measurements and derivations of LWC and TWC with the DMT CAS, CIP, LWC-100 and the WCM-2000 were made, and the data were selected when the instruments showed reasonably comparable results.

## **2.2 Meteorology**

The meteorology of the Southern Ocean is primarily defined by the circumpolar storm track (Simmonds and Keay 2000; Hoskins and Hodges 2005). In the vicinity of Tasmania and southeast Australia, cold fronts are commonly anchored in mid-latitude cyclones and cut-off lows (e.g. Figure 2.2) and they are the main cause of wintertime precipitation (Risbey *et al.*, 2009; Chubb *et al.*, 2011). Commonly, pristine conditions (e.g. Yum and Hudson, 2004; Gras, 1995) are encountered to the west and south of Tasmania during post-frontal periods that can last for one to four days. In the space between cold fronts, a mid-latitude ridge often becomes the dominant synoptic feature. This feature can also force pristine SO air mass towards Tasmania, especially when the ridge is present to the west of Tasmania.

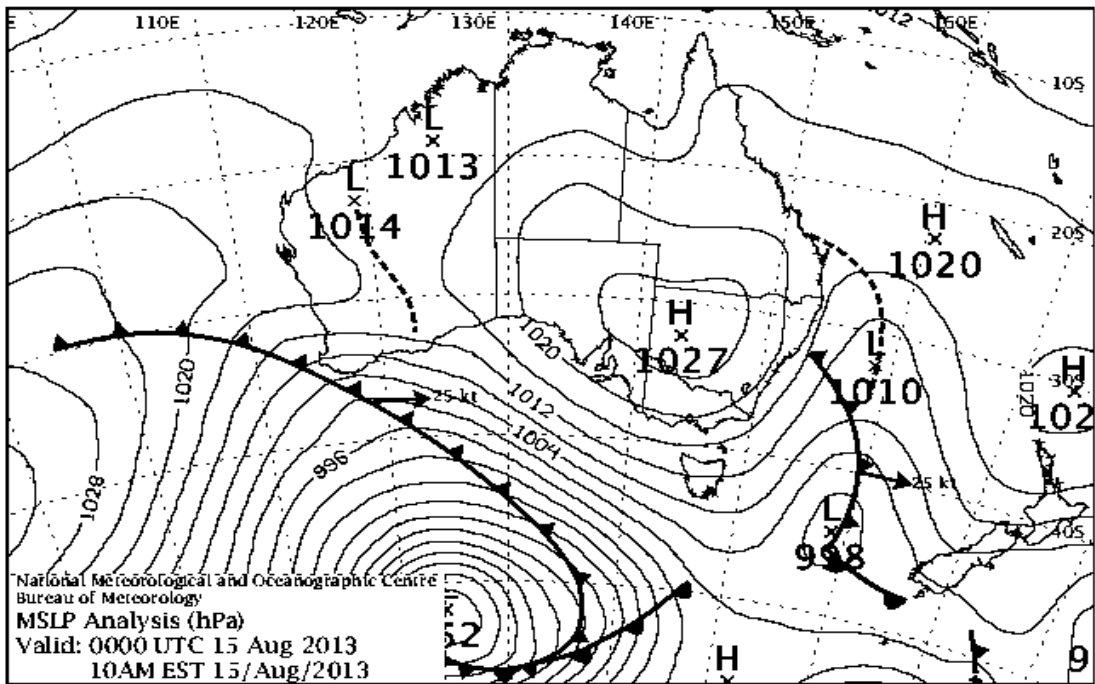


Figure 2.2. Mean sea level pressure (MSLP) from 15<sup>th</sup> August, 2013 00 UTC.

The majority of the SOCEX I flights (Boers *et al.*, 1996, 1998) were conducted when such a ridge was prominent and produced a well-defined boundary layer with boundary layer clouds. In contrast to the SOCEX I flights, operational cloud seeding flights are typically flown shortly after the passage of the cold front (6-24 hours) when supercooled liquid water is readily encountered at much higher elevations (up to 4 km) (Morrison *et al.*, 2010). The research flights were made under various meteorology, although no flights were conducted in the midst of a cold front due to a potential of lightning hazard. Table 2.1 details the dominant synoptic features for each flights.

When the observations were limited to low to mid-level clouds only, it was also possible to identify the structure of the mesoscale cellular convection (MCC) (if any) following Wood and Hartmann (2006) (Figure A6). MODIS visible and infrared images with a time window as close as the flight time were employed for this classification (Table 2.1

---

and Figure A7). Most of the observations made shortly after the passage of a cold front are found to be of open MCC. Muhlbauer *et al.* (2014) illustrated that during winter open MCC occurs more frequently than closed MCC in the lower latitudes of the SO. This is opposed to the closed MCC, more commonly found when a high pressure ridge is the dominant meteorological feature, as observed during SOCEX I.

Table 2.1 also details the average thermodynamic characteristics (cloud phase fractions, temperatures, pressures) of the clouds sampled for all 20 flights. While the aircraft did, on occasion, observe mid-level clouds with average pressures as low as 667 hPa, the vast majority of observations were made in low-level cloud (pressures greater than 700 hPa). The average in-cloud temperature reveals that the pristine segments of operational cloud seeding flights spent the majority of time ferrying in clouds between -8 and -10 °C; research flights observed clouds over a far greater range of meteorological conditions, although the temperature range was commonly between -6 and 0 °C.

Estimated cloud top and base heights are also presented in Table 2.1, as recorded during the aircraft sounding on site. We note, however, that these observations may be of limited value given that the clouds did not reside in horizontally homogeneous fields, especially for open and disorganised MCC. Observations of cloud top height, cloud base and cloud thickness often varied substantially over the course of an hour.

### **2.3 Cloud thermodynamic phase**

Table 2.1 further details the time spent in cloud for each flight. Using the ice-water fraction,  $\mu_3$ , the cloud samples were sorted in ‘liquid’ clouds ( $\mu_3 \leq 0.1$ ), ‘mixed phase’ clouds ( $0.1 < \mu_3 < 0.9$ ) and ‘ice’ clouds ( $0.9 \leq \mu_3$ ), following Korolev *et al.* (2003). The percentage of time spent in these conditions is presented for each flight along with the percentage over all 20 flights. Overall, ice clouds were only sampled 1.8% of the time

---

but mixed phase clouds were encountered 36.7% of the time. 19 of the 20 flights recorded the presence of ice (mixed-phase or ice) at some point in these pristine clouds over the open ocean, which is a very different picture from that illustrated by SOCEX I. Boers *et al.* (1996) lists a single flight that encountered mixed phase clouds, which was subsequently removed from the analysis. Not surprisingly, the percentage of time in liquid clouds is correlated with the average in-cloud temperature; liquid clouds are more common at warmer temperatures, and mixed-phase and ice clouds are more common at colder temperatures including the range of -3 and -8 °C necessary for the Hallett-Mossop process of ice multiplication.

The sensitivity of the ice-water fraction,  $\mu_3$ , to the ambient temperature can be explored in a means similar to Korolev *et al.* (2003) (Figure 2.3). All in-cloud observations were sorted into 5 °C bins. At temperatures greater than 0 °C, clouds are predominantly liquid with  $\mu_3$  always less than 0.1. At temperatures between 0 °C and -5 °C,  $\mu_3$  is less than 0.1 roughly 76% of the time with much of the remaining cloud having at small values ( $0.1 < \mu_3 < 0.5$ ). At colder temperatures ( $-10 \text{ °C} < T < -5 \text{ °C}$  and  $-15 \text{ °C} < T < -10 \text{ °C}$ ), the frequency of liquid clouds drops to less than 40% while mixed phase samples ( $0.3 < \mu_3 < 0.7$ ) become dominant. Heavily glaciated clouds ( $\mu_3 > 0.7$ ) are rarely encountered at any of the temperature bands.

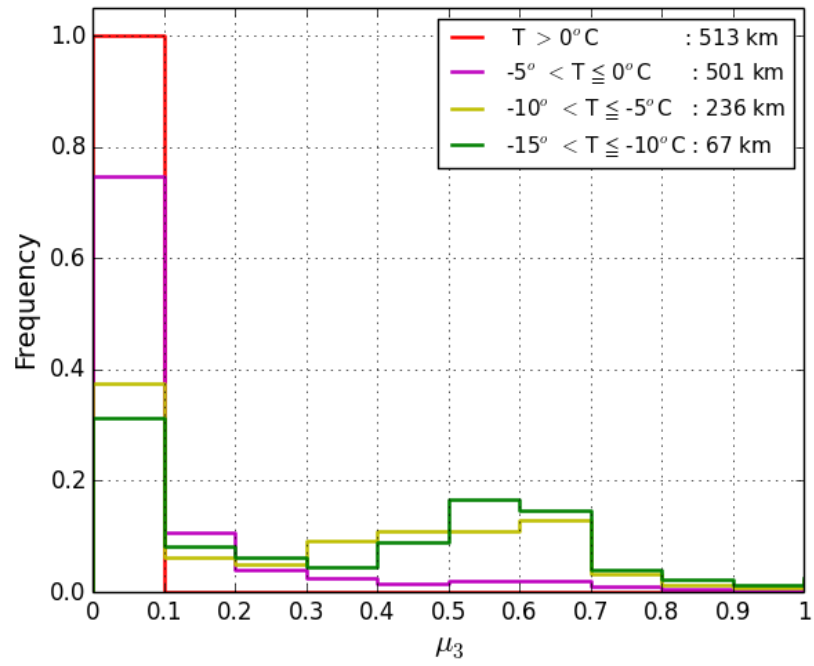


Figure 2.3. Fractions of cloud phase coefficient ( $\mu_3$ ) for different temperature intervals for 20 flights of three consecutive winters (Jun - Oct, 2013 - 2015).

The durations of the sampled data are indicated in the legend next to the temperature bins.

As discussed before, heavily glaciated clouds may be under sampled in this study as deep, frontal clouds were intentionally avoided in both the research and operational cloud seeding flights. Nevertheless, such distributions are notably different from those reported in Korolev *et al.* (2003) where observations were taken from five different field campaigns across Canada (Figure 2.4) although instrumentation and time in clouds were different from ours. The mixed phase clouds sampled across Canada were found to be primarily liquid or primarily glaciated with a minimum for  $0.2 < \mu_3 < 0.7$  for temperature bands below  $0^\circ\text{C}$ . For the  $-15^\circ\text{C} < T < -10^\circ\text{C}$  temperature band, ice clouds were observed nearly 40% of the time in the Canadian flights opposed to  $\sim 1\%$  for the pristine SO clouds examined in our study. Such differences in ice fractions support the argument of Burrows *et al.* (2013) that there are fewer active ice nuclei over the Southern Ocean at these temperatures.

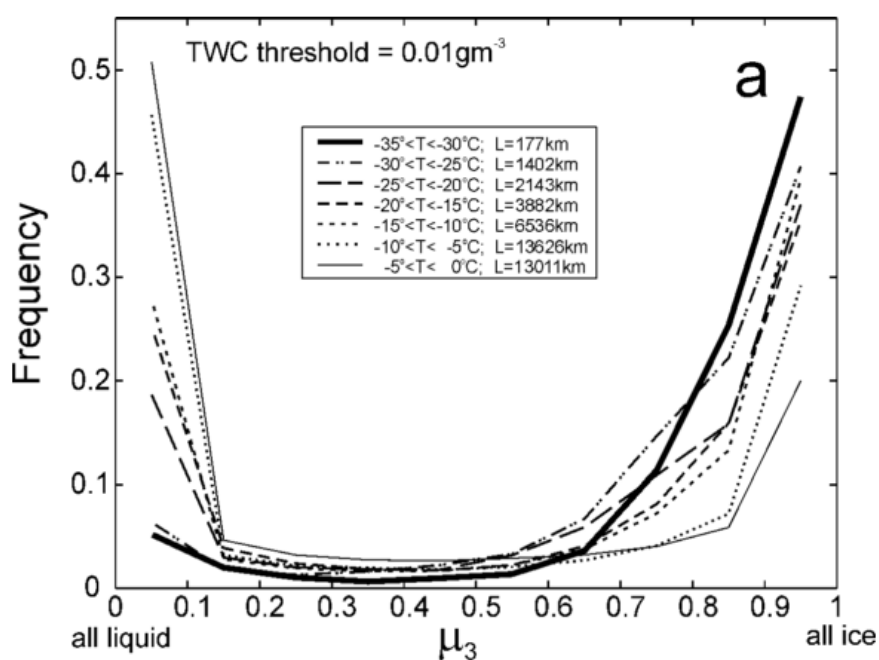


Figure 2.4. Fractions of cloud phase coefficient ( $\mu_3$ ) for different temperature intervals for 5 different field campaigns across Canada (Adapted from Korolev *et al.*, 2013).

---

The quantitative values reported in this work (including differences in the ice fraction,  $\mu_3$ ) are a function of both the instruments and the thresholds employed. It is hard to estimate what extent the difference in the frequency of phase fraction is caused by differences in meteorology, instruments and processing techniques that are used by Korolev et al. (2003). We can and have, however, highlighted the differences in the meteorological conditions between our work and the Korolev papers. Most notably we commonly observed maritime clouds, as opposed to terrestrial boundary layer clouds. We commonly observed open MCC as opposed to stratiform clouds. The data used in Korolev et al. (2003) are from different projects in different areas and times with different instruments, but all observations were not made in summer. The bulk of the data was collected in stratiform clouds (St, Sc, Ns, As, Ac), usually associated with frontal systems. During the BASE and FIRE.ACE projects, a number of flights sampled cirrus clouds.

The scale of spatial averaging is about 100 m (1 s) as our study, and the TWC threshold,  $0.01 \text{ gm}^{-3}$  for clouds is the same as our study. Different instruments were used in different experiments, but they are mostly FSSP-100 (2 – 90  $\mu\text{m}$ ), 2DC (25 – 100  $\mu\text{m}$ ), PVM-100, King LWC (- 50  $\mu\text{m}$ ), OAP probes (25 – 6400  $\mu\text{m}$ ), Nevzorov LWC/TWC probes for LWC and TWC. Therefore, it will be difficult to describe all the differences of instruments and processing technique. But the basic technical mechanism to measure LWC and TWC are the same as DMT CAPS (CAS, CIP) and hot wire probes in our study used. Also, the data processing technique is exactly the same as our study employed that from Korolev 2003. The only difference in data processing can be the SODA software usage in our study.

## **2.4 Mean microphysical characteristics of liquid clouds**

Hereafter we limit our attention on liquid clouds ( $\mu_3 \leq 0.1$ ) only when considering  $r_{eff}$ ,

$N_d$  and liquid water content (LWC). Accordingly, the number of cloud samples is reduced from 20,357 to 12,520. The average for each individual flight (representative average) in Table 2.1 is calculated following Boers *et al.* (1998), which first averages  $r_{eff}$  and  $N_d$  separated into 10 hPa pressure bands. The values in each pressure band are then averaged to define the representative average. The first two rows in Table 2.3 are calculated from the 20 representative averages and are comparable to those reported for SOCEX I. A simple time average  $N_d$  from all 1-second liquid cloud samples from all flights is  $28 \text{ cm}^{-3}$  with a standard deviation of  $30 \text{ cm}^{-3}$  (Table 2.3).

Table 2.3. Overall averages of the liquid-only cloud average microphysical properties for 20 flights' observations of three consecutive winters (Jun - Oct, 2013 - 2015). 'Boers method' is average of representative averages (Table 2.1) of all flights. 'Simple average' is average of all cloud samples from all flights. 'Consistent liquid average' is average for consistent liquid clouds which are consistent over a minimum time period of 5 minutes ( $\sim 30 \text{ km}$ ). The numbers in parentheses are standard deviations (s.d.).

Different method/source of average	$N_d$ [ $\text{cm}^{-3}$ ] (s.d.)	$r_{eff}$ [ $\mu\text{m}$ ] (s.d.)	LWC [ $\text{gkg}^{-1}$ ] (s.d.)
Boers method (CAS only)	27 (21)	12.5 (2.0)	0.140 (0.054)
Boers method (CAS + CIP)	27 (21)	21.4 (12.5)	0.239 (0.103)
Simple average (CAS only)	28 (30)	12.5 (2.9)	0.146 (0.167)
Simple average (CAS + CIP)	28 (30)	21.6 (25.7)	0.268 (0.897)
Consistent liquid average (CAS only)	40 (41)	11.4 (3.0)	0.122 (0.122)
Consistent liquid average (CAS + CIP)	40 (41)	22.4 (28.2)	0.227 (0.494)
SOCEX I average (FSSP only)	28 (11)	12.4 (1.8)	0.129 (0.03)

The SOCEX I wintertime range for  $N_d$  ( $10 - 40 \text{ cm}^{-3}$ ) holds for 17 of the 20 flights (Table 2.1). One flight (03 Aug 2013) recorded a lower average  $N_d$  of  $7 \text{ cm}^{-3}$ , and the

---

remaining two flights recorded  $N_d$  at 80 and 89  $\text{cm}^{-3}$ , respectively. The liquid clouds sampled for the low  $N_d$  flight (3 Aug 2013) may be anomalous in that they were relatively cold and sparse. The majority of the clouds encountered on this day were mixed-phase (79.1%). The observations from the two high  $N_d$  flights (denoted as CASE A for 23 Jul 2013 and CASE B for 01 Oct 2015), however, are believed to be robust. They are also unique, being the only encounters of closed MCC and are examined in more detail in the next section. When sorted by MCC structure, the difference between open and closed MCC clouds is evident (Table 2.1). The two remaining classes (unorganised and no structure) have microphysical properties much closer to open MCC than closed MCC clouds.

Turning to the effective radius (CAS only), the average over all liquid cloud samples (Table 2.3, simple average) is 12.5  $\mu\text{m}$  with a standard deviation of 2.9  $\mu\text{m}$ , with 18 of the 20 flights having  $r_{eff}$  in the range of 9.8 to 15.4  $\mu\text{m}$ . These values are comparable to those reported for SOCEX I. The two high  $N_d$  flights have the lowest values of  $r_{eff}$ (CAS) at 8.2 and 8.5  $\mu\text{m}$  (Table 2.1). When the larger droplets from the CIP are included, the average effective radius over all liquid cloud samples,  $r_{effT}$ , increases to 21.6  $\mu\text{m}$  with a standard deviation of 25.7  $\mu\text{m}$ . The average liquid water content (CAS + CIP) is 0.268  $\text{gkg}^{-1}$  with a standard deviation of 0.897  $\text{gkg}^{-1}$ . The two high  $N_d$  flights had relatively low LWCs (CAS+CIP) at 0.173 and 0.165  $\text{gkg}^{-1}$ , respectively.

It may be argued that these average liquid cloud properties may not represent ideal liquid clouds given that mixed phase samples are intermixed on numerous flights. This is explored by recalculating the properties after filtering out any liquid cloud observations that are near (within five minutes) a mixed phase or ice sample, leaving only isolated liquid cloud samples from eight “consistent-liquid” flights (Table 2.3). The two high  $N_d$  flights are included in these eight. Overall, the total number of 1-second liquid cloud samples was reduced from 12,520 to 3,258. The average  $N_d$  increases to 40  $\text{cm}^{-3}$  with a standard deviation of 41  $\text{cm}^{-3}$ , as the two high  $N_d$  flights

---

were largely retained in this calculation. The effective radius dropped to 11.4 ( $\pm 3$   $\mu\text{m}$ ) for the CAS-only, and 22.4 ( $\pm 28.2$   $\mu\text{m}$ ) for the CAS+CIP calculation. The LWC (CAS+CIP) is 0.227 ( $\pm 0.494$   $\text{gkg}^{-1}$ ). This information is summarised in Table 2.3 along with comparable averages from SOCEX I (Boers *et al.*, 1996), although it was not possible to analyse the four ‘baseline’ flights of SOCEX I in an identical manner.

It is also of interest to test the sensitivity of these values to the ambient temperature as Gultepe and Isaac (1997), Gultepe *et al.* (2002), and Gultepe and Isaac (2004) did in their great efforts to relate microphysical properties (e.g.  $N_d$  and LWC) and temperature to improve microphysical modeling studies. Much like the analysis of the ice-water fraction, these liquid cloud properties are now sorted into temperature bands of 5  $^{\circ}\text{C}$  from -15  $^{\circ}\text{C}$  to 10  $^{\circ}\text{C}$  (Figure 2.5). The liquid only cloud samples of all twenty flights (12,520 one-second samples) have been compiled for these calculations. Approximately 73% of all samples were in the two bands between -5  $^{\circ}\text{C}$  and 5  $^{\circ}\text{C}$  (Figure 2.5 (a)). Approximately 6% of the samples were from clouds warmer than 5  $^{\circ}\text{C}$  and 20% of the samples were at temperatures below -5  $^{\circ}\text{C}$ . This sharp drop in fractional cloud cover at colder temperatures is consistent with the climatology of Huang *et al.* (2012b) using satellite observations.

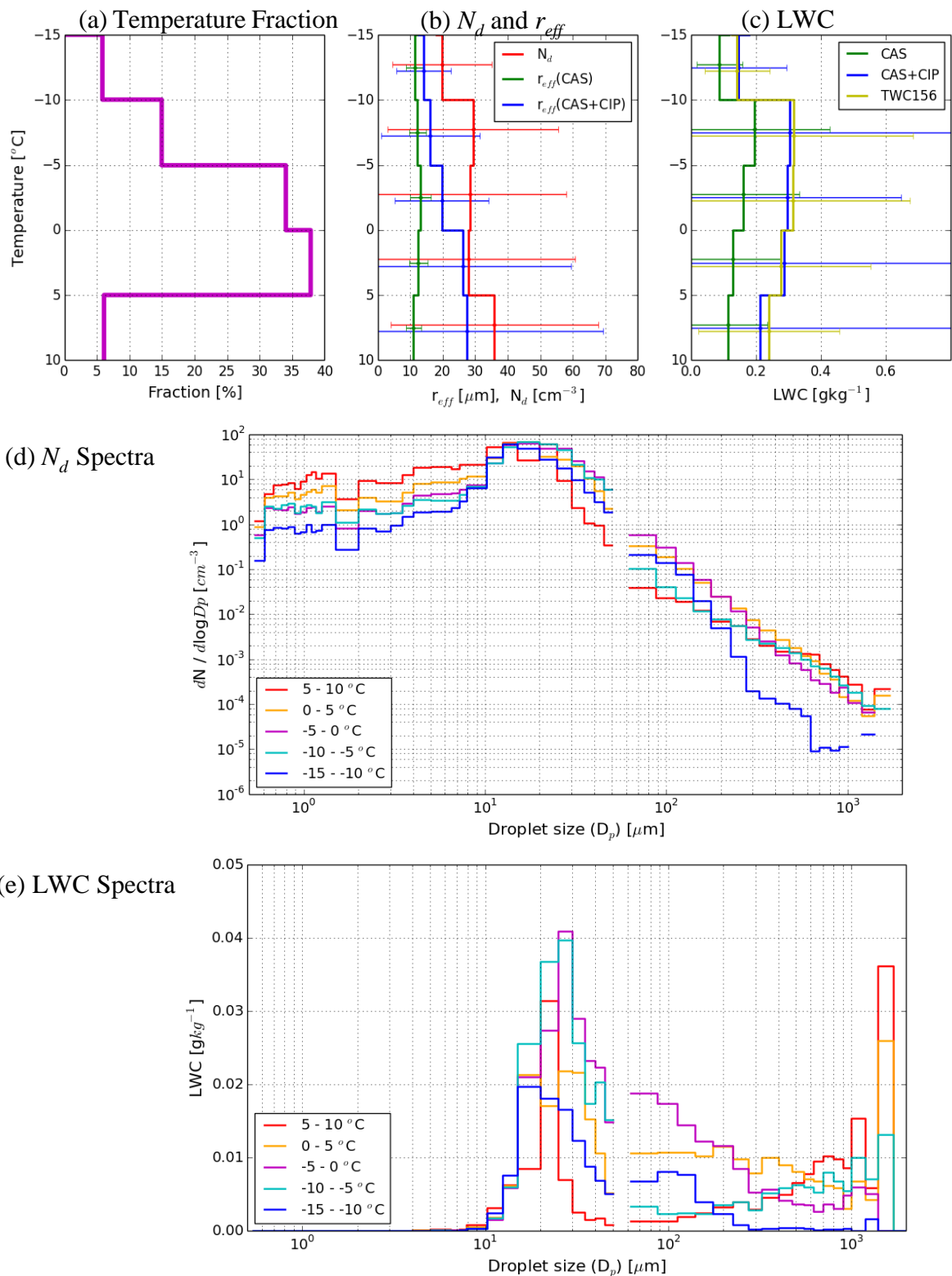


Figure 2.5. Averaged microphysical properties and spectra by temperature for liquid clouds from 20 flights observations of three consecutive winters (Jun - Oct, 2013 - 2015).

---

(a) Fraction by temperature, (b)  $r_{eff}$  and  $N_d$  by temperature, (c) LWC by temperature, (d) cloud number concentration spectra by temperature, and (e) LWC spectra by temperature. (b) and (c) The horizontal error bars are standard deviations.

When the liquid cloud observations are aggregated in this manner, there is no significant difference in  $N_d$  and  $r_{eff}$  of clouds from -10 to 5 °C although warmer clouds (5 °C < T < 10 °C), presumably lower elevation clouds, has greater values of  $N_d$ , and colder clouds (-15 °C < T < -10 °C) has lower values of  $N_d$  (Figure 2.5(b)).

When the effective radius is calculated from only the CAS probe,  $r_{eff}$ , no significant variation is observed over different temperature bands (Figure 2.5 (b)). If, however, the CAS+CIP effective radius, (i.e.  $r_{effT}$ ) is used, then a positive trend is observed with increasing temperature. We suspect that this trend is largely a reflection of drizzle developing in these clouds as drizzling clouds have a higher portion of large (greater than 15  $\mu\text{m}$ )  $r_{eff}$  (CAS+CIP), as shown in Figure 3.2 (b) which is described in section 3.2.

The LWC (CAS) (Figure 2.5 (c)) is between 0.13 – 0.2  $\text{gkg}^{-1}$  for temperatures greater than -10 °C, with very little LWC differences from the CAS+CIP and TWC probe. This confirms that ~20% over-estimation from the CIP LWC from out of focus effects is well corrected by Korolev (2007) as described in 'CIP data processing' section in the appendix.

Similar to the bulk measurements, the spectra of particle size from the CAS and CIP measurements can be aggregated into 5 °C temperature bands (Figure 2.5 (d)). The warmest clouds have the largest contribution of small droplets ( $D_p < 10 \mu\text{m}$ ), while the coldest clouds have the fewest in this range. If drizzle developed in the warmest clouds, then we might expect the small droplets to be removed by coalescence. This large contribution of small droplets at warmer temperatures actually reflects the relative

---

contribution of the two high  $N_d$  flights, in which much of the cloud sampled was at warmer temperatures (Table 2.1).

Gultepe et al. (2002) and Gultepe and Isaac (2004) aggregated data observed *in-situ* on Arctic clouds, maritime boundary-layer clouds, and winter storms over Canada in three different field projects and they found  $N_d$  and LWC decreased with decreasing temperature. This trend has not been found in our study although the amount of our flight data is relatively small (~20% of theirs in the temperature range between -10 °C and 5 °C) and  $N_d$  in 5 °C - 10 °C is 6 cm<sup>-3</sup> higher than  $N_d$  in -10 °C – -5 °C.

Figure 2.5 (d) shows droplet  $N_d$  spectra by temperature. Most droplets are found in the range of 10 – 40 μm where the droplet spectra of -10 °C < T < 5 °C are similar. Accordingly, the average  $N_d$  is ~27 cm<sup>-3</sup> for all cloud samples between -10 °C to 5 °C. For the clouds warmer than 5 °C, small droplets (< 10 μm) contribute to the higher average  $N_d$  (~36 cm<sup>-3</sup>, Figure 2.5 (b)).

Figure 2.5 (e) accounts for the decreasing trend of LWC by temperature. The spectra of liquid cloud samples in the -10 °C and 0 °C temperature range (aquamarine and magenta), which are SLW, are dominated by droplets in the 15 – 110 μm size range. These droplets contribute to the LWC relatively more higher than those from warm cloud samples in the 5 °C – 10 °C temperature range.

To summarize, our clouds are mostly in the range of -10 °C to 5 °C. We believe that the Hallett-Mossop process, which is temperature dependent, plays a major role in the microphysics of these clouds. In this temperature range, the mean effective radius ~15 μm, and the number concentration ( $N_d$ ) and mass (LWC) are found to be independent on the ambient temperature. In addition, the SLW droplets in the size range of 15 – 110 μm heavily contribute to the LWC. These values of  $N_d$  and LWC are notably different to those from the NH where the average  $r_{eff}$  is only 6.8 μm (Gultepe *et al.* (2002); Gultepe and Isaac (2004)). It should be also noted that the average LWC (~0.3 gkg<sup>-1</sup>) of our study is higher than comparable observations of the NH (0.12 – 0.18 gkg<sup>-1</sup>).

---

Focusing on larger droplets and drizzle, some variation is evident at the extreme temperature bands; at the colder temperatures, a strong drop off is evident in the number of larger drops ( $D_p > 200 \mu\text{m}$ ), perhaps suggesting an absence of drizzle in these clouds. At warmer temperatures a drop off is evident in the number of droplets between 20 and 200  $\mu\text{m}$ . Not surprisingly, the LWC is largely defined by the drops over 20  $\mu\text{m}$  but less than 200  $\mu\text{m}$  (Figure 2.5 (e)). Only the clouds at the warmest temperatures show a significant contribution to LWC from the drops greater than 500  $\mu\text{m}$ .

## 2.5 Summary and discussion

The microphysics properties retrieved from the SOCEX I (Boers *et al.*, 1996) have long defined the wintertime  $N_d$  very low ( $10 < N_d < 40 \text{ cm}^{-3}$ ) and  $r_{eff}$  very large ( $10.8 < r_{eff} < 14.7 \mu\text{m}$ ) for the liquid clouds of this region. The maximum LWC for these flights was between 0.1 and 0.2  $\text{gkg}^{-1}$ . Such pristine conditions are unique in comparison with those of the North Pacific, North Atlantic or Arctic. For example, during the First International Satellite Cloud Climatology Project (ISCCP) Regional Experiment-Arctic Cloud Experiment (FIRE.ACE), the mean  $N_d$  over the Arctic Ocean in April for clouds of an air mass of Arctic origin was observed at  $91 (\pm 43) \text{ cm}^{-3}$  where the temperature was between  $-25$  and  $0 \text{ }^\circ\text{C}$  with LWC  $0.066 (\pm 0.042) \text{ gm}^{-3}$  (Gultepe and Isaac, 2002). Gultepe and Isaac (2002) detailed observations of air masses of North Pacific origin with a mean  $N_d$  of  $57 (\pm 41) \text{ cm}^{-3}$ , LWC of  $0.14 (\pm 0.128) \text{ gm}^{-3}$ , and  $r_{eff}$  of  $9.2 (\pm 4.6) \mu\text{m}$  in the same temperature range.

Ultimately only five flights taken over four days underpin the SOCEX I wintertime microphysical properties. Further, those flights were all made under a very specific synoptic setting, namely along the leading edge of anti-cyclonic ridges, which are commonly observed between the passages of cold fronts. The ridge largely inhibits mid-

---

level cloud and establishes a well-defined boundary layer inversion. In this work we greatly expand the wintertime microphysical properties of SOCEX I by analysing observations taken across a much broader representation of the meteorology; pre-frontal, post-frontal, and near frontal environments have also been sampled. In all, 20 flights taken over the course of three winters (June – October, 2013 - 2015) have been analysed. Liquid clouds were sampled up to heights of 5000 m, although this was relatively uncommon.

One immediate difference between this campaign and SOCEX I was the common presence of ice. 14 of the 20 flights had ice (either mixed phase or glaciated) present for at least 10% of all cloud samples. During SOCEX I only one flight observed mixed phase clouds, which was subsequently removed from any analysis. Of the total 20,357 one-second records spent in cloud in our observations, 38.5% were found to contain ice crystals, primarily in mixed-phase clouds (36.7%) rather than glaciated clouds (1.8%). The droplet spectra and temperature range suggest these clouds were ideal for the Hallett-Mossop ice multiplication process, which should come as no surprise, as this is the region where Mossop first encountered such clouds (Mossop *et al.*, 1970). The mixed phase samples observed commonly had an ice water fraction ( $\mu_3$ ) between 0.5 and 0.7, which is vastly different from those found in the neighbourhood of Canada as detailed in Korolev *et al.* (2003). These mixed phase and glaciated observations are not the primary focus of this study, leaving the analysis centred on liquid cloud observations.

Ultimately the mean microphysical properties from this new campaign remain consistent with those of SOCEX I; the average  $N_d$  was  $28 (\pm 30) \text{ cm}^{-3}$ , the average  $r_{eff}$  (CAS only) was  $12.5 (\pm 2.9) \mu\text{m}$ , and the average LWC (CAS+CIP) was  $0.268 (\pm 0.897) \text{ gkg}^{-1}$ . When the clouds were filtered to remove those near mixed-phase or glaciated samples (within 5 minutes or  $\sim 30 \text{ km}$ ), the average  $N_d$  was  $40 (\pm 41) \text{ cm}^{-3}$ , the average  $r_{eff}$  (CAS only) was  $11.4 (\pm 3.0) \mu\text{m}$ , and the average LWC (CAS+CIP) was  $0.227$

---

( $\pm 0.494$ )  $\text{gkg}^{-1}$ . When the synoptic and local meteorology is analysed for all 20 flights, no outstanding relationship between the meteorology and  $N_d$  was found except some high  $N_d$  flights encountered post frontal conditions more often.

---

## Chapter 3

# Drizzle in Southern Ocean Clouds and a Case Study



Figure 3.0 Broken, patchy and drizzling cloud imagery taken by the Gopro camera equipped on the Cessna Conquest aircraft at 14:35 AEST, 30-August-2015 heading north.

Bennartz (2007) employed MODerate-resolution Imaging Spectroradiometer (MODIS) observations of maritime clouds to examine their sensitivity to precipitation, concluding that  $N_d$  in non-drizzling clouds was about 2.5 times higher than that in drizzling clouds. Note that Bennartz (2007) was largely limited to latitudes lower than  $45^\circ\text{S}$  and did not account for artefacts arising from large solar zenith angles (Wood 2012). Consistent with Bennartz (2007), Wood *et al.* (2012) found that the presence of drizzle reduced  $N_d$  by a factor of 2 to 3. More recently, Huang *et al.* (2015b) used spatiotemporal collocated A-Train observations to reveal more distinct characteristics of the SO clouds, which are sensitive to the presence of precipitation. Chapter 2 described the examination of natural variability of the cloud microphysics observed by *in-situ*. In this chapter, the analysis further explores their sensitivity to the presence of drizzle.

---

### 3.1 Drizzle fraction and rain rate

As noted in Wood *et al.* (2012), the presence of drizzle can modify the cloud microphysics. Precipitation, even light drizzle, can result in the removal of smaller cloud droplets by collision and coalescence. In general, precipitation may leave clouds with smaller values of  $N_d$  and larger  $r_{eff}$ , or clouds with small  $r_{eff}$  are less likely to contain drizzle (Rosenfeld *et al.*, 2012). It is an open question as to whether precipitation drives to the very low values of  $N_d$  observed over the Southern Ocean. Boers *et al.* (1996) encountered active drizzle on some of the SOCEX flights and speculated that the other ‘baseline’ clouds had previously experienced light precipitation due to low  $N_d$  and sub-adiabatic LWC. Here we employ the CIP to define the presence of drizzle. For a liquid cloud, if the LWC from droplets with size greater than  $112.5 \mu\text{m}$  is greater than  $0.005 \text{ gm}^{-3}$  in clouds, then the sample was classified as drizzling. Rain rate was calculated using the fall speed of those droplets (Pruppacher and Klett 2010). As our flights avoided active cold fronts, our samples are primarily of drizzle or light precipitation. Further, mixed phase clouds are excluded in this analysis, although it is likely that the majority of these samples would be classified as being precipitating.

Overall, the liquid clouds observed in this study were drizzling 49% of the time (6135 samples, Table 2.1) and their mean rain rate was  $0.733 \text{ mmhr}^{-1}$ . The percentages for drizzle and rain rates for individual flights are also detailed in Table 2.1, which range from 91% to 0% and  $3.667 \text{ mmhr}^{-1}$  to  $0 \text{ mmhr}^{-1}$ , respectively.

It is interesting to examine the intermittency of drizzle (and non-drizzle) in these SO clouds which is indicated by the frequency of the duration of drizzling and non-precipitating ‘patches’ (Figure 3.1). This is important because many satellite retrieval algorithms assume some kind of horizontal homogeneity. Drizzle and non-drizzle patches of short one and two second durations (equivalent to  $\sim 100$  to  $200 \text{ m}$ ) are most

common. It was quite rare to observe solid segments of non-precipitating clouds for periods of greater than 10 seconds (1 km). While it was more common to observe this for drizzling clouds, it was still relatively rare. This may be due to a combination of the small size of these clouds (which are primarily open MCC and unorganised MCC) and the intermittent presence of mixed-phase and glaciated samples, as well as intermixed drizzling and non-drizzling samples, all of which lead to a high degree of inhomogeneity. Stretches of relatively homogeneous boundary layer cloud simply were not observed in these 20 flights except in CASE A, which is further examined in section 3.3.

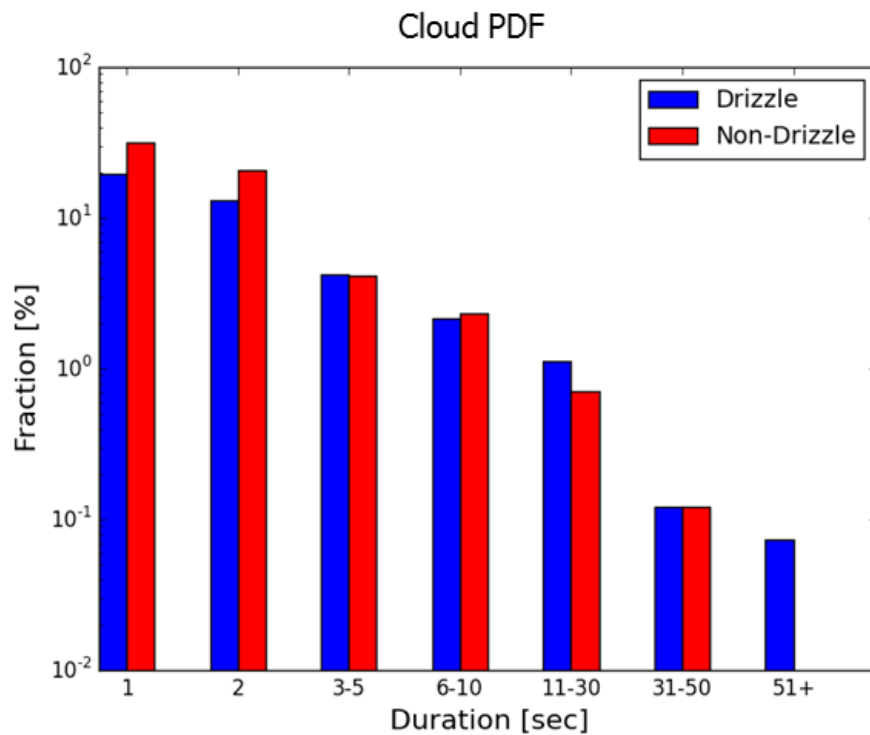


Figure 3.1. The probability density function (PDF) of drizzling and non-drizzling sections of liquid clouds from 20 flights observations of three consecutive winters (Jun - Oct, 2013 - 2015).

The cloud distributions are analysed by consistent drizzle or non-drizzle cloud sections for each time period (e.g. 11 - 30 s).

## 3.2 Mean microphysical properties of drizzling and non-drizzling clouds

In Table 3.1 the standard cloud properties have been recalculated based on the detection of drizzle. The average  $N_d$  of ‘drizzling’ liquid clouds drops to  $26 (\pm 18) \text{ cm}^{-3}$  and, correspondingly, the average in ‘non-drizzling’ clouds increases to  $36 (\pm 36) \text{ cm}^{-3}$ . The two high  $N_d$  flights contribute substantially to the non-drizzling clouds. Not surprisingly, the effective radius (CAS only) is larger for drizzling clouds ( $13.5 \pm 2.5 \mu\text{m}$ ) than that for non-drizzling clouds ( $10.6 \pm 3.5 \mu\text{m}$ ). Liquid water content is higher in drizzling clouds ( $0.185 \pm 0.179 \text{ gkg}^{-1}$ ) than non-drizzling clouds ( $0.126 \pm 0.151 \text{ gkg}^{-1}$ ). These differences are statistically significant according to K-S tests and T-Tests with  $p$ -values approaching 0 for  $N_d$ ,  $r_{eff}$ , and LWC.

Table 3.1. Summary of microphysical properties of 1 and 10 s consistent drizzle and non-drizzle sections of clouds from 20 flights’ observations of three consecutive winters (Jun - Oct, 2013 - 2015). The standard deviations (s.d.) are indicated in parentheses.

Cloud Properties		Non-drizzle (s.d.)	Drizzle (s.d.)	All Clouds (s.d.)
$N_d$ (CAS) [ $\text{cm}^{-3}$ ]	1 s	36 (36)	26 (18)	28 (30)
	10 s	43 (40)	25 (16)	26 (30)
$N_d$ (CIP) [ $\text{cm}^{-3}$ ]	1 s	0.007 (0.030)	0.18 (0.28)	0.09 (0.21)
	10 s	0.002 (0.01)	0.22 (0.32)	0.090 (0.217)
$r_{eff}$ (CAS) [ $\mu\text{m}$ ]	1 s	10.6 (3.5)	13.5 (2.5)	12.5 (2.9)
	10 s	9.5 (3.2)	13.6 (2.4)	12.9 (2.8)
$r_{effT}$ (CAS + CIP) [ $\mu\text{m}$ ]	1 s	11 (3.9)	32.8 (33)	21.6 (25.7)
	10 s	9.8 (3.5)	34.4 (28)	22 (27.5)
LWC (CAS) [ $\text{gkg}^{-1}$ ]	1 s	0.126 (0.151)	0.185 (0.179)	0.146 (0.167)
	10 s	0.109 (0.119)	0.172 (0.152)	0.139 (0.170)
LWC (CIP) [ $\text{gkg}^{-1}$ ]	1 s	0.002 (0.008)	0.244 (1.206)	0.122 (0.867)
	10 s	0.001 (0.003)	0.271 (0.578)	0.122 (0.932)
Temp [ $^{\circ}\text{C}$ ]	1 s	-2.8 (6.0)	-0.5 (3.9)	-1.7 (5.2)
	10 s	-1.8 (5.5)	0.5 (3.2)	-3.9 (6.4)

---

Given that drizzle was highly intermittent in these clouds, the data were further sampled to only consider ‘solid patches’ of drizzle, i.e. liquid cloud samples where drizzle was detected for at least 10 seconds. Similarly, ‘solid patches’ of non-drizzling clouds could be defined. We found that this refinement had a very minor effect on the average properties of drizzling clouds and a minor effect on the non-drizzling clouds (not shown). The ambient temperature of the samples was also averaged according to the presence of drizzle. While there is considerable variability, we note that on average drizzling clouds were warmer ( $-0.5\text{ °C} \pm 3.9\text{ °C}$ ) than non-drizzling clouds ( $-2.8\text{ °C} \pm 6.0\text{ °C}$ ). This temperature difference is statistically significant. This difference may be due to drizzle being at a more mature/advanced state at lower altitudes or warmer temperatures.

In Figure 3.2 (a), all 12,520 liquid cloud samples have been sorted into bins according to  $N_d$  to produce a probability density function (PDF). The bulk of the 1-second observations ( $\sim 83\%$ ) have  $N_d$  less than  $45\text{ cm}^{-3}$  and are split roughly equally between drizzling (49%) and non-drizzling (51%) samples. Only  $\sim 11\%$  of the samples have  $N_d$  between 45 and  $75\text{ cm}^{-3}$ , with little difference between drizzling and non-drizzling. Less than 5% of all samples have  $N_d$  between 75 and  $105\text{ cm}^{-3}$ . Approximately 5% of all samples have  $N_d$  between 105 to  $120\text{ cm}^{-3}$ , and these were almost exclusively from the two high  $N_d$ , non-drizzling flights. It is not possible to establish whether any of the non-precipitation observations are being sampled after they experienced precipitation. However, like the conclusions of Boers *et al.* (1996), we similarly speculate that if  $N_d$  is less than  $45\text{ cm}^{-3}$  for a non-drizzling cloud, then it is likely to have already experienced drizzle. For  $N_d$  greater than  $105\text{ cm}^{-3}$ , however, we assume that the non-drizzling cloud has not experienced any drizzle even though there is no direct means to observe this or infer the age of clouds.

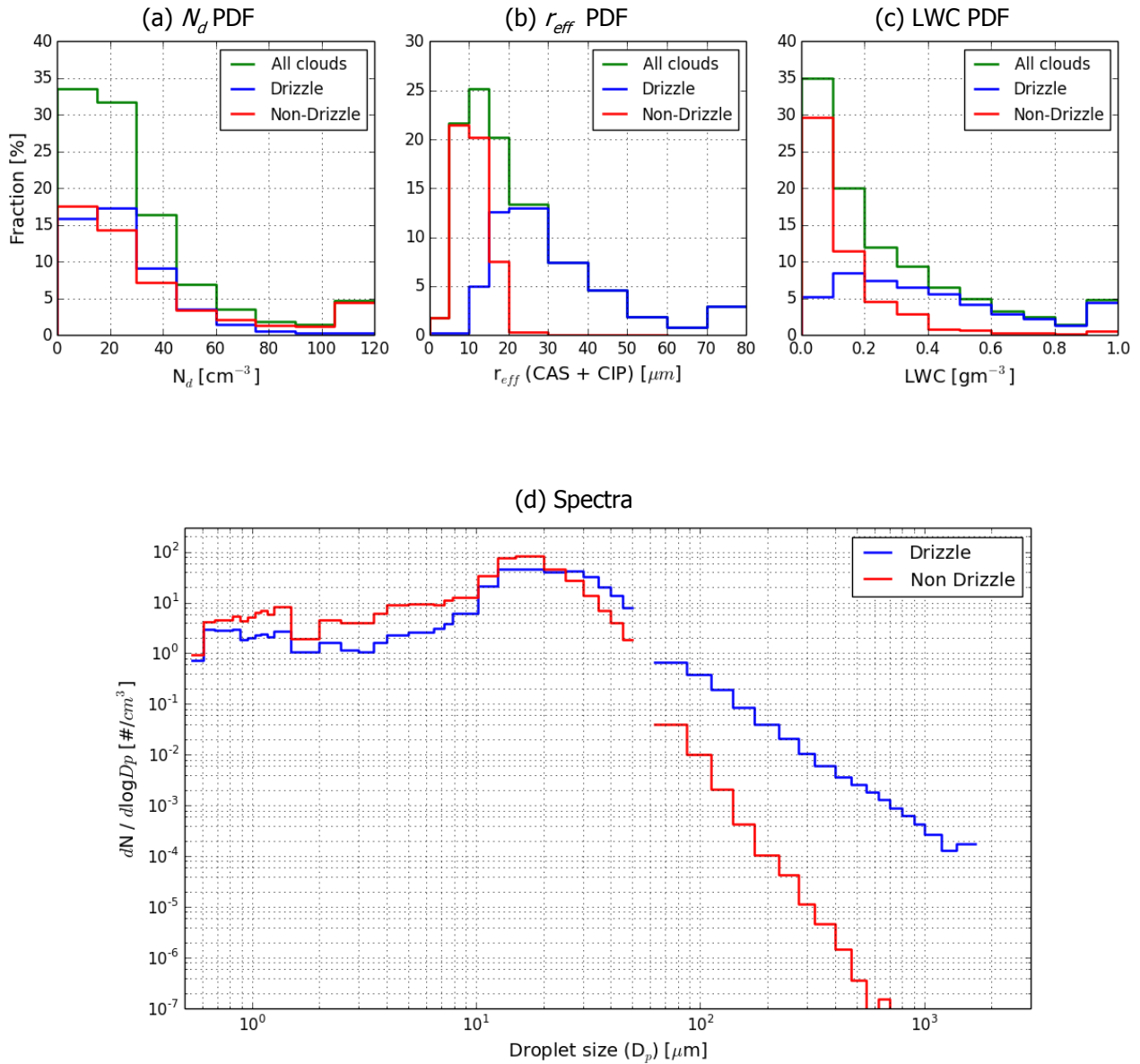


Figure 3.2. The probability density function (PDF) of (a)  $N_d$ , (b)  $r_{eff}$  (CAS + CIP), (c) LWC (CAS+CIP), and (d) the spectra of drizzling and non-drizzling liquid clouds from 20 flights' observations of three consecutive winters (Jun - Oct, 2013 - 2015).

Similarly, a PDF (Figure 3.2 (b)) can be produced for the combined effective radius,  $r_{effT}$  (CAS + CIP), with the fractional contribution much as expected; non-drizzling clouds generally have smaller effective radii. Almost none of non-drizzling samples had

---

an effective radius greater than 20  $\mu\text{m}$ . Consistent with Table 2.1, ~67% of all one second samples have  $r_{effT}$  between 5 and 30  $\mu\text{m}$ . Drizzling clouds dominate the contribution to average effective radius when  $r_{effT}$  was greater than 15  $\mu\text{m}$ . This carries forward to the LWC (Figure 3.2 (c)), reflecting the greater contributions of the large CIP droplets to this measurement. Non-drizzling samples are only dominant for thin/light clouds ( $\text{LWC} < 0.1 \text{ gkg}^{-1}$ ), although even these thin clouds can experience drizzle. The spectra for drizzling and non-drizzling clouds are as expected (Figure 3.2 (d)). In general, drizzling clouds have a greater concentration of larger droplets and a reduction of smaller ones (size  $< 10 \mu\text{m}$ ).

### 3.3 A Comparison of drizzle and non-drizzle cases

Overall, the average cloud properties examined in this study were very consistent with those established during SOCEX I. Pristine liquid wintertime clouds over the SO have a low droplet number concentration, large effective radius and, given their shallow depth, substantial LWC compared to those in the Northern Hemisphere (Han *et al.*, 1998; Isaac *et al.*, 2001; Gultepe and Isaac 2002; Dong and Mace 2003). Further, drizzle is quite common. Looking at the flights individually, two of the 20 flights fail to conform to this picture. The flights of 23 July 2013 (CASE A) and 01 October 2015 (CASE B) were characterised by relatively high  $N_d$ , small  $r_{eff}$  and very little drizzle (Figure 3.3). It should be noted that the vertical profiles do not indicate vertical variation through one cloud layer. It may be claimed that these two flights ‘distorted’ the average properties of non-drizzling and warm clouds. If these two flights were removed from the analysis, the differences between ‘drizzling’ and ‘non-drizzling’ samples were relatively weak; the  $r_{eff}$ ,  $N_d$  and LWC (CAS + CIP) for the remaining non-drizzling samples were 11.5  $\mu\text{m}$ , 23  $\text{cm}^{-3}$  and 0.128  $\text{gkg}^{-1}$ , respectively (not shown).

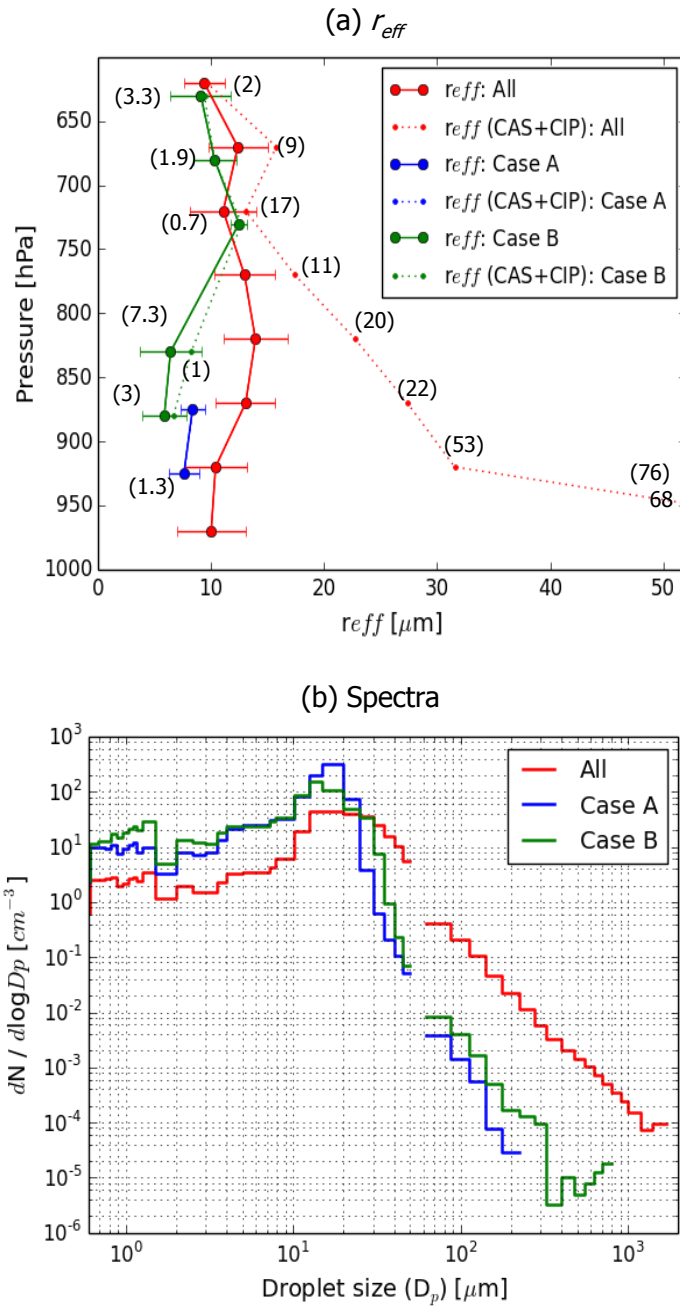


Figure 3.3. Comparison of  $r_{eff}$  and spectra for CASES A and B against all 18 flights. ‘All’ means all flights except CASES A and B.

(a) Mean  $r_{eff}$  and  $r_{effT}$  (CAS+CIP) by pressure. The  $r_{effT}$  (CAS+CIP) at the 1000 to 950 hPa is written on the plot as 68. The horizontal error bars on  $r_{eff}$  are standard deviations. The standard deviations of  $r_{effT}$  (CAS+CIP) are indicated in the parentheses (b) Particle size spectra of all flights and CASES A and B.

---

Further, CASES A and B were the only two flights that encountered closed mesoscale cellular convection (Table 2.1). It is of particular interest to appreciate not only how frequently such clouds exist over the SO, but also the synoptic and mesoscale processes that drive them. As a point of contrast, two ‘typical’ drizzling flights have been selected, which display low  $N_d$ , large  $r_{eff}$  and near constant presence of drizzle. The flights of 28 June 2013 (CASE C) and 30 August 2015 (CASE D) were research flights that encountered prolonged periods of lightly precipitating clouds (85% and 91%, respectively), low  $N_d$  and large  $r_{eff}$ . All four flights were primarily within relatively warm, low elevation clouds.

Table 3.2 details the local environment for the four flights, as observed by the aircraft. It is difficult to isolate any extreme conditions amongst these four flights. All four flights sampled low-elevation clouds of 500 - 600 m thickness with cloud top ranging from 1 to 1.3 km. The boundary layer clouds of the two high  $N_d$  flights were in particularly warm environments.

Figure 2.1 details the back-trajectories of these four flights. An initial inspection does not portray any immediate reason for the anomalous conditions. The high drizzle flight CASE D (30 August 2015) stands out for having an air mass origin from much higher latitudes. By contrast the high drizzle flight CASE C is unremarkable, having stayed in a mid-latitude band. Compared to many of the other back-trajectories this air mass is moving relatively slowly across the Southern Ocean, consistent with the local wind speed measurement. The back-trajectories for the two high  $N_d$  flights are also relatively unremarkable. Arguably CASE A air mass was moving slowly, presumably due to the high pressure system, while CASE B air mass was moving relatively quickly.

Table 3.2. Comparison of thermodynamic and microphysical properties and meteorology from the soundings for two non-drizzle dominant cases (CASES A and B, 23 July 2013 and 01 October 2015, respectively) and two drizzle dominant cases (CASES C and D, 28 June 2013 and 30 August 2015, respectively).

The standard deviations (s.d.) are indicated in parentheses for the cloud microphysical properties.

Category	Non-drizzle dominant flights		Drizzle dominant flights	
	CASE A (20130723)	CASE B (20151001)	CASE C (20130628)	CASE D (2015830)
Time in liq. clouds [s]	679	803	1,338	1,754
Drizzle %	0 %	4 %	85 %	91 %
Cloud top	1.2 km	1.8 km	1.6 km	1.5 km
Cloud base	0.8 km	1 km	0.7 km	0.7 km
CTT	-0.3 °C	0.7 °C	-2 °C	-2.6 °C
CBT	0.2 °C	5.9 °C	0.7 °C	0.1 °C
In cloud lapse rate	1.7 °C / km	8.7 °C / km	5.4 °C / km	3 °C / km
Inv. strength	5.5 °C	3 °C	2 °C	7 °C
Inv. height	0.9 km	1.5 km	1.4 km	1.4 km
Wind direction	S	SW	SW	SE
$N_d$ [ $\text{cm}^{-3}$ ] (s.d.)	89 (37.5)	80 (45.4)	21 (14)	13 (9.7)
$r_{\text{eff}}$ [ $\mu\text{m}$ ] (s.d.)	8.2 (1.2)	8.5 (2)	14.2 (2.4)	13.2 (2.3)
$r_{\text{effT}}$ [ $\mu\text{m}$ ] (s.d.)	8.2 (1.2)	8.5 (10.9)	23 (10.9)	36 (10.9)
LWC (CAS) [ $\text{gkg}^{-1}$ ] (s.d.)	0.165 (0.122)	0.172 (0.199)	0.190 (0.181)	0.079 (0.101)
LWC (CAS+CIP) [ $\text{gkg}^{-1}$ ] (s.d.)	0.165 (0.141)	0.173 (0.210)	0.306 (0.203)	0.390 (0.210)
Synoptic condition	high pressure ridge	post frontal	weak high pressure ridge	associated with low pressure system
MCC <sup>1)</sup>	stratiform closed MCC	closed MCC <sup>2)</sup>	open MCC	open MCC

<sup>1)</sup> MCC (mesoscale cellular convection). <sup>2)</sup> The interpretation of the MODIS image of this day is difficult due to the presence of multi-level clouds.

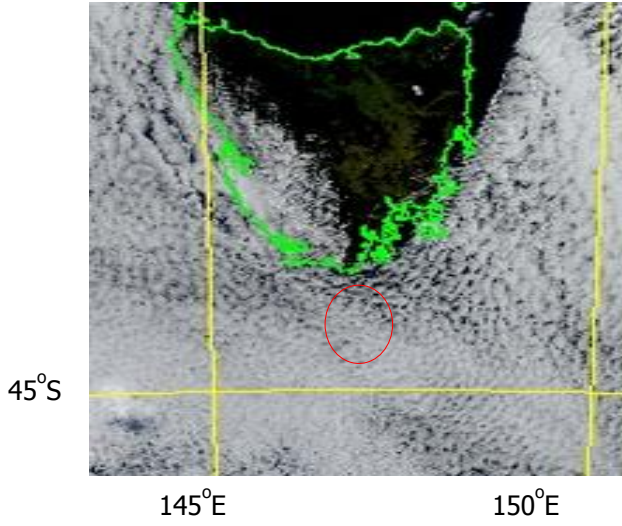
---

The daily meteorology was synchronised to these back-trajectories (Figure A5) to examine the potential role of fronts and cyclones. In particular, we examined whether either high  $N_d$  case encountered gale-force winds as described in Chubb *et al.* (2016), or pre-frontal conditions. Chubb *et al.* (2016) detailed observations of extremely high  $N_d$  (200 - 300  $\text{cm}^{-3}$ ) for the SO, and attributed the observations to sea spray driven from pre-frontal gale force winds. No such conditions were encountered over 72 hours for CASES A and B.

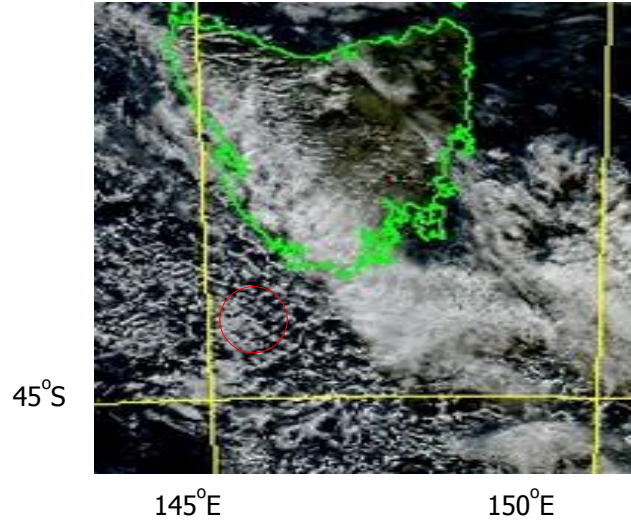
The synoptic meteorology of CASE A flight is more fully presented in Huang *et al.* (2015a). In summary, an intense anticyclone (1,034 hPa) was located near the coast of South Australia with a ridge extending to the southeast to roughly 50°S, 155°E. A small cut-off low was located in the Tasman Sea. The relatively unique conditions drove air from higher latitudes towards Tasmania. A Cloud-Aerosol Lidar with Orthogonal Polarization (CALIOP) overpass and MODIS image found that the free troposphere was largely free of clouds to the south of Tasmania, but solid boundary layer clouds persisted with a cloud thickness of roughly 0.4 - 0.6 km.

Conversely, the high  $N_d$  CASE B occurred in post-frontal conditions with a thick layer of clouds between 530 and 650 hPa (Figure 3.4), as shown by the aircraft sounding. A solid deck of low elevation clouds (pressure > 800 hPa) was also present that day and was the source of the high  $N_d$  samples. The upper layer clouds consist of 51% of mixed and ice phase and the lower layer is predominantly liquid phase of 98%. A MODIS image for the day reveals the complexity of the cloud field arising from the passage of a cold front. Below the mid-level cloud, closed mesoscale cellular convective clouds formed over a region of ~ 250km X ~200km. Ultimately, the synoptic meteorology of these two high  $N_d$  flights has little in common.

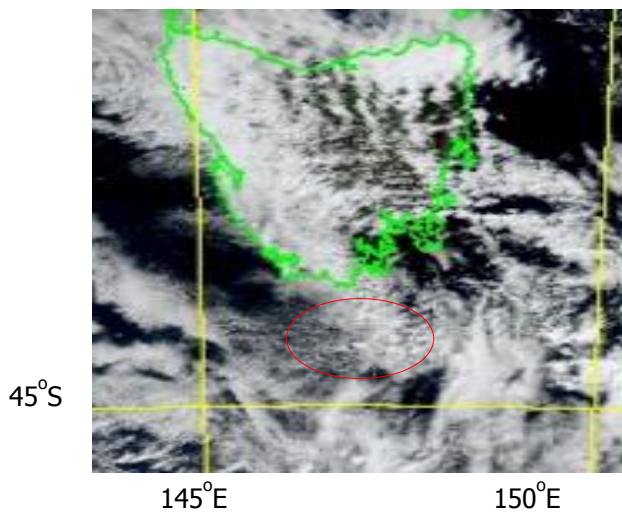
(a) CASE A



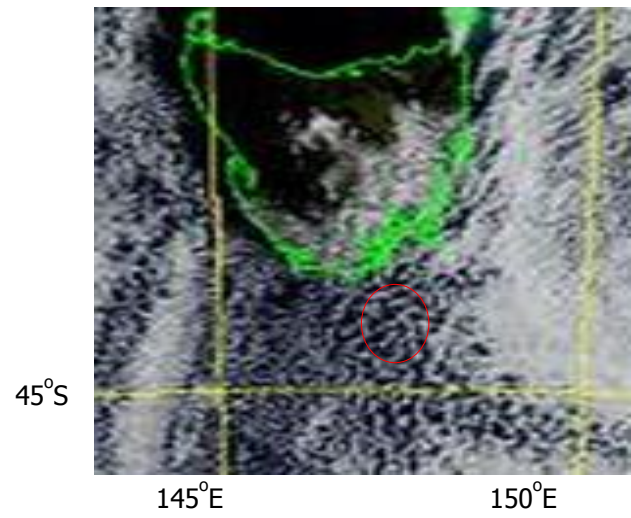
(c) CASE C



(b) CASE B



(d) CASE D



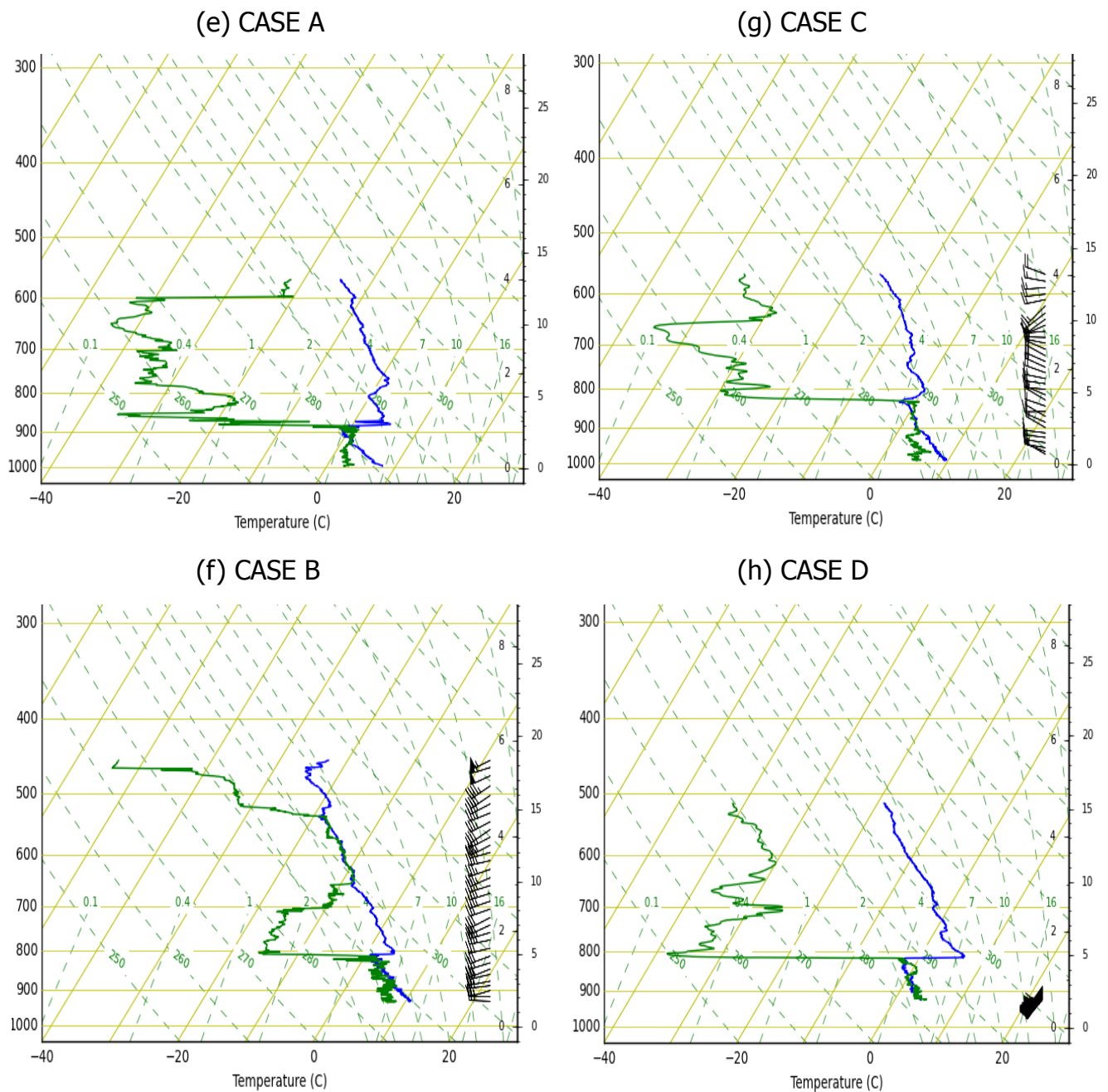


Figure 3.4. MODIS satellite images (a) - (d) and soundings (e) - (h) for two minimum drizzle cases, CASES A and B (23 July 2013 and 01 October 2015, respectively) and two heavily drizzle cases, CASES C and D (28 June 2013 and 30 August 2015, respectively).

(a) - (d) The locations where each flight was flown are indicated with a red circle. The times of the images taken are 1425, 1425, 1430, and 1425 AEST (UTC + 10h), respectively. (e) - (h) The times when the soundings made are about 1600, 1313, 1335, and 1342 AEST respectively.

---

The differences in the synoptic meteorology of the two high drizzle flights are much smaller than that for the high  $N_d$  flights. The MODIS images for CASE C and CASE D detail open mesoscale cellular convection to the southwest and south of Tasmania, respectively. The aircraft sounding for CASE C identifies an inversion at 820 hPa with a cloud deck extending down to 900 hPa. The mean-sea-level pressure (MSLP) analysis (not shown) suggests that a weak ridge was dominant over the region for this period of time. These boundary layer clouds were far removed from any frontal dynamics during the observation period. The aircraft sounding for CASE D identifies an inversion at 810 hPa with shallow cloud and relatively thicker cloud between 860 and 900 hPa. The MSLP analysis (not shown) displays a cut-off low (1001 hPa) present near 40°S, 158°E, and a strong high pressure system (1033 hPa) south of Tasmania (50°S, 145°E), leaving the Southern Ocean with a southerly airflow. Vertical profiles of cloud microphysical properties that correspond to the sounding profiles in Figure 3.4 are shown in Figure 3.5. Despite the high variability, it is evident that both average LWC and  $r_{eff}$  (CAS+CIP) for the two non-drizzling flights (CASE A and B) appear to increase with altitudes, which is consistent with a typical cloud profile described by an adiabatic cloud model.

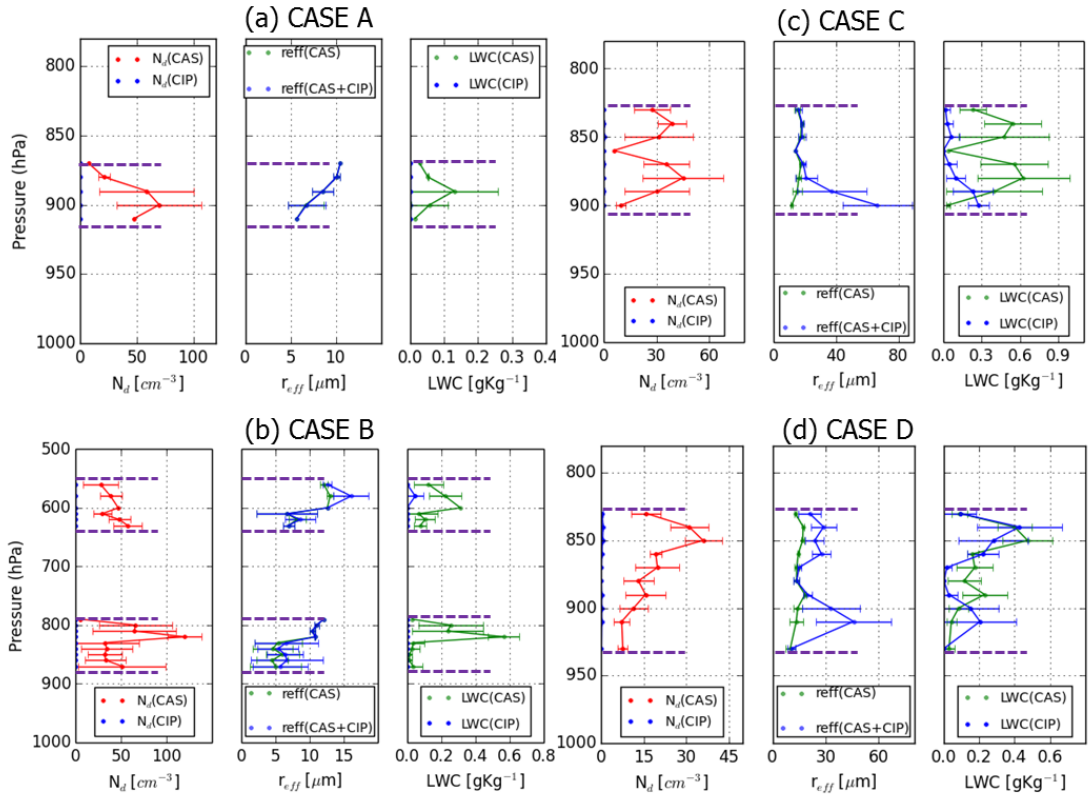


Figure 3.5. (a) – (d) Vertical profile of cloud microphysical properties ( $N_d$ ,  $r_{eff}$ , and LWC) from the soundings of non-drizzling cases (CASES A and B) and drizzling dominant (CASES C and D) flights in Figure 3.4 (e) ~ (h).

The estimated cloud base and top heights are indicated by the dashed lines. The error bars are standard deviations.

The profiles for the two drizzling flights (CASE C and D), on the other hand, behave differently. In particular, the  $r_{eff}$  (CAS+CIP) for CASE C and D (where heavy drizzle was present) increase dramatically towards cloud base (warmer temperatures), which is in support of our speculation on the positive trend with increasing temperature as seen in Figure 2.5 (b). These profiles also suggest that the drizzling clouds are much more inhomogeneous than the non-drizzling clouds.

In summary, an initial investigation into these four cases finds that the synoptic

---

conditions were not able to fully explain the generation of drizzle and the associated differences in  $N_d$  and  $r_{eff}$ . More dedicated in-situ observations and analysis are needed to further explore this issue.

### 3.4 Summary and discussion

Similar to SOCEX I, drizzle or light precipitation was frequently observed throughout this campaign. 49 % of all liquid cloud samples were observed to be precipitating. As drizzle samples were commonly in the neighbourhood of mixed phase or non-drizzling cloud samples, it was rare to observe solid patches of drizzle of greater than 10 seconds.

There were distinct observations of non-drizzling clouds with relatively high  $N_d$  ( $\sim 89 \text{ cm}^{-3}$ ) and small  $r_{eff}$  ( $\sim 8.5 \text{ }\mu\text{m}$ ) for two of the 20 flights (CASES A and B). These two flights, 11% of all liquid cloud samples, were largely responsible for the difference between the average liquid cloud properties and the average ‘consistent liquid’ cloud properties. These two flights were ultimately responsible for much of the difference between the drizzle and non-drizzle average properties, too. It is noteworthy that the average  $N_d$  for these two flights is roughly a factor of three greater than the overall average, which is largely consistent with the ideal model of Wood (2012) and suggests that these clouds have not yet experienced drizzle. Not surprisingly the drizzling samples were, on average, found to have lower  $N_d$  and greater  $r_{eff}$  than that of the overall average. It was further concluded that much of the non-drizzling samples (after the two anomalous high  $N_d$  flights were removed) have largely similar  $N_d$  values as the drizzling liquid cloud samples, suggesting that there is a possibility that these non-drizzling samples were the remains of clouds that had previously been drizzling (note that there is no direct means to infer cloud age from the limited observations). This suggestion was reached in Boers *et al.* (1996) for SOCEX I, as well.

---

The clouds from the two high  $N_d$  flights are unique, being the only observations of closed MCC. The average results according to the MCC structure in Table 2.1 shows the outstanding differences in microphysical properties between the closed MCC flights and other types of MCC flights. The link between non-drizzle and closed MCC is consistent with the observations made over the eastern Pacific during the Variability of the American Monsoon Systems Ocean-Cloud-Atmosphere-Land Study (VOCALS) experiment (Wood *et al.*, 2011). An initial, thorough examination of the local and synoptic environment for these two flights failed to identify any particular forcing that may have led to the unique microphysical properties with our limited instrumentation. It is plausible that a different source of cloud condensation and/or ice nuclei could contribute to such differences, although this is speculative.

While these new observations greatly expand the study of microphysical properties of SOCEX I, they are still of limited scope and do not produce a full climatology of the microphysical properties of liquid water clouds over the Southern Ocean. They do, however, highlight that greater variability of  $N_d$  exists in wintertime clouds over the SO when a wider range of synoptic meteorology is investigated. They further suggest that some cloud fields are being influenced by physical processes yet to be identified. This work also serves as a basis for future research on the evaluation of satellite products for effective radius and cloud droplet number concentration.

---

## Chapter 4

### A comparison of cloud microphysical properties derived from MODIS and CALIPSO with *in-situ* measurements over the wintertime Southern Ocean

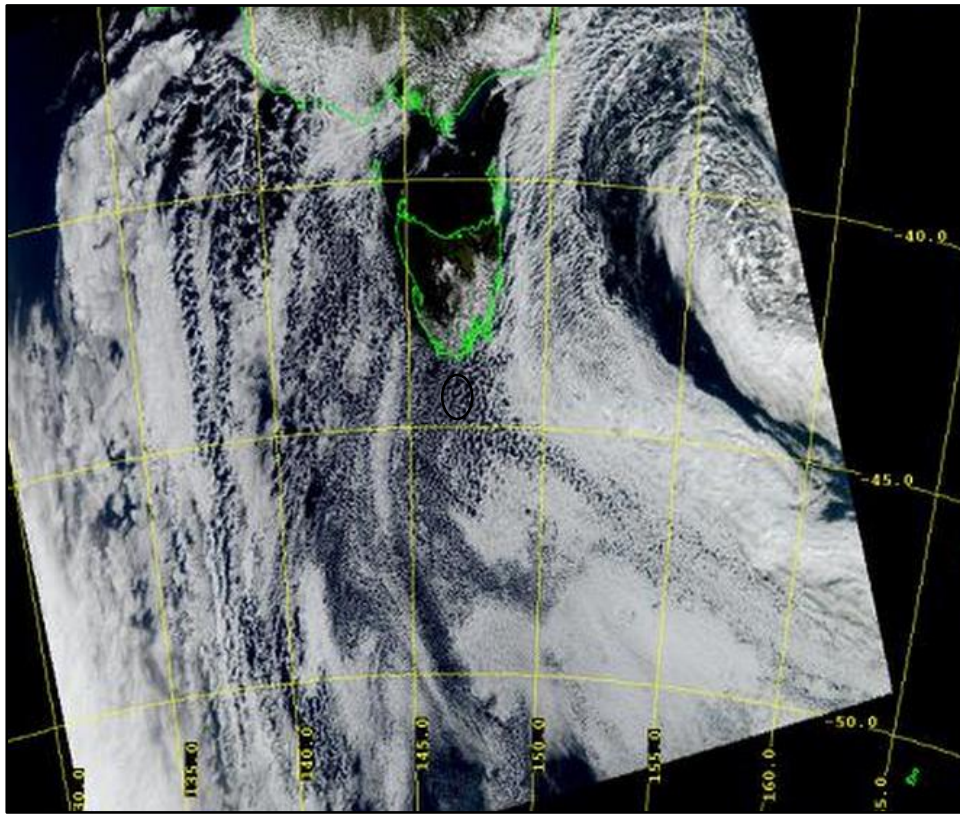


Figure 4.0 MODIS on board Aqua visible imagery at 14:25 AEST, 30-August-2015. Open MCC cloud is noticeable where the research flight was conducted at  $\sim 44.5^{\circ}\text{S}$ ,  $147^{\circ}\text{E}$  adjacent to closed MCC clouds near  $46^{\circ}\text{S}$  and  $148^{\circ}\text{E}$ .

---

## 4.1 Introduction

The unique nature of SO clouds and the lack of verification studies over this region, limit our confidence in satellite (e.g. MODIS, CALIOP) products. Huang *et al.* (2015a) illustrated substantial differences in the cloud-top thermodynamic phase classifications from the MODIS, CALIPSO and a merged radar-lidar product (DARDAR Mask; Delanoë & Hogan, 2010) over the remote SO. The uncertainty between these different products can be exacerbated during the winter months, if the observations, such as those from the MODIS (Wood *et al.*, 2012, Grosvenor & Wood, 2014), are sensitive to the solar zenith angle (SZA). In addition, the presence of drizzle together with small droplets near to cloud top, presumably caused by evaporation, has been found to affect the MODIS spectral retrievals (e.g., Chang & Li, 2002; Nakajima *et al.*, 2010a, 2010b; Suzuki *et al.*, 2010; Zhang & Platnick, 2011).

Given the unique nature of SO clouds, it is a necessary exercise to directly compare/evaluate satellite retrievals against *in-situ* observations, as has been done elsewhere. For example, Min *et al.* (2012) and King *et al.* (2013) employed *in-situ* observations made over the Southeast Pacific during the Variability of the American Monsoon Systems (VAMOS) Ocean-Cloud-Atmosphere-Land Study Regional Experiment (VOCALS-REx) to evaluate MODIS-based products for effective radius ( $r_{eff}$ ) and cloud droplet number concentration ( $N_d$ ), as well as liquid water path and cloud optical thickness (COT). These passive radiometer products are of immediate interest given their large spatial coverage and widespread use in radiative transfer models.

The  $r_{eff}$  calculated from the MODIS retrieval algorithm has consistently been found to overestimate *in-situ* observations by 15 - 20% (Painemal & Zuidema 2011), by up to 1.75  $\mu\text{m}$  (Zheng *et al.*, 2011), by up to 2.3  $\mu\text{m}$  (Min *et al.*, 2012) and by 13% (King *et al.*, 2013). MODIS-derived  $N_d$ , on the other hand, agreed well (Vaughan *et al.*, 2007) with *in-situ* observations (Painemal & Zuidema, 2011; Min *et al.*, 2012).

---

Beyond the microphysics, the dynamics of the open cellular clouds prevalent over the SO especially in wintertime (Muhlbauer *et al.* 2014) are also present challenges in employing remote sensing observations with confidence. Previous work has demonstrated that the cloud  $r_{eff}$  for broken clouds is more strongly overestimated than for overcast clouds (e.g., Barker & Liu, 1995; Oreopoulos & Davies, 1998; Coakley *et al.*, 2005) over a dark marine surface because of the reduced radiance at shortwave/midwave infrared due to the clear-sky contribution and to the use of plane-parallel forward models (e.g., Zhang & Platnick 2011; Zhang *et al.*, 2012). Wolters *et al.* (2010) supports this by showing that the overestimation of MODIS  $r_{eff}$  for a broken cloud regime over the Atlantic Ocean is up to 2.5 times higher than for inhomogeneous overcast clouds. On the other hand, it is surprising that Platnick *et al.* (2015) showed that for a certain month (April 2005), the Aqua MODIS (collection 6; hereafter C6) global monthly mean  $1^\circ$  gridded  $r_{eff}$  for the partly cloudy pixels was significantly smaller than that for the overcast pixels. The confidence of satellite retrievals of effective radius and cloud droplet number concentration over open MCC clouds needs to be further examined.

Eleven of the 20 flights detailed in chapter 2 were performed to coincide with A-Train overpasses. This research directly compares *in-situ* cloud thermodynamic and microphysical properties ( $r_{eff}$ ,  $N_d$ ) against MODIS and CALIOP products over the remote Southern Ocean. Further, we examine the sensitivity of the retrieved products to operational constraints (i.e. a high SZA) and cloud regimes (i.e. drizzle, mixed-phase clouds and partially cloudy pixels). Finally, we contrast our findings against similar studies over the Southeast Pacific (i.e. Min *et al.*, 2012; King *et al.*, 2013) to better appreciate the level of skill of these products over the SO.

---

## **4.2 Data and methodology**

### **4.2.1 Flight overview and aircraft measurements**

A full description of the meteorology and microphysical observations of the 20 wintertime flights over the Southern Ocean (43 – 45°S, 145 – 148°E) is detailed in chapter 2. The eleven research flights employed in this chapter were designed to coincide with A-Train overpasses. The coincided time, location, conditions of each flight are summarised in Table 4.1. The flight overview and aircraft measurements are detailed in section 2.1.

Table 4.1 Summary of the eleven flights from 2013 – 2015 spatiotemporally coincided with A-Train constellation (MODIS and CALIPSO). The average cloud properties are for liquid only (except ice fraction) by *in-situ* and MODIS observations. The MODIS  $r_{eff}$  is retrieved from the combined pixels with overcast and PCL. The standard deviation of  $r_{eff}$  is indicated in parenthesis. The drizzling flights are highlighted.

Flight Date	Coincide Start [UTC]	Coincide End [UTC]	Lat	Long	MCC <sup>1)</sup> type	Solar Zenith Angle [°]	CALIPOP availability	Drizzle Fraction	Rain Rate [mmhr <sup>-1</sup> ]	Ice Fraction	Aircraft $r_{eff}$ (std.) [μm]	$r_{eff\_1.6}$ (std.) [μm]	$r_{eff\_2.1}$ (std.) [μm]	$r_{eff\_3.7}$ (std.) [μm]	CM_SPI <sup>2)</sup> band1/ band2 [%]	$r_{eff}$ Retrieval Failure Rate
20130614	04:20	04:50	-43.66	148.3	open MCC	73.5 - 73.7	Yes	0%	0.001	1.3%	9.6 (1.5)	15.6 (7.4)	18.5 (4.9)	16.1 (3.3)	13/17	8%
20130628	04:19	04:49	-43.89	145.2	open MCC	73.4 - 73.9	Yes	86%	0.375	8%	23.3 (10.5)	17.1 (7.5)	23.4 (4.6)	18.5 (3.2)	13/18	27%
20130707	04:13	04:43	-44.59	146.98	open MCC	73.1 - 73.6	Yes	0%	0.001	85%	16.4 (2.7)	16.1 (7.2)	20.4 (5.2)	15.7 (3.3)	28/39	32%
20130723	04:12	04:42	-44.05	146.94	closed MCC	70.5 - 70.8	Yes	0%	0.000	0%	8.3 (1.1)	14 (6.2)	12.9 (3.1)	12.6 (2)	12/15	7%
20130806	04:30	05:00	-42.64	143.63	open MCC	66.2 - 66.5	Yes	39%	0.530	12%	16.9 (17)	15.2 (7.7)	20.2 (5.4)	17.1 (3.9)	23/31	35%
20130815	04:19	04:49	-42.9	144.64	disorganised MCC	63.8 - 64.1	Yes	8%	0.004	43%	12.7 (3)	22.1 (6.3)	25.1 (3.2)	20.8 (2.6)	11/15	12%
20131011	04:12	04:42	-44.58	147.08	disorganised MCC	49.3 - 49.7	Yes	1%	0.002	54%	9.3 (2.9)	18.7 (6.4)	22.2 (4.4)	18 (2.9)	14/18	13%
20140903	04:19	04:49	-44.01	145.28	open MCC	59.7 - 60.3	Yes	14%	0.097	24%	17.8 (18.2)	18.2 (7.3)	22.6 (4)	18.3 (2.9)	13/17	13%
20140912	04:27	04:57	-44.86	147.04	open MCC	57.9 - 58.1	No	40%	0.043	18%	16.9 (6.4)	17.9 (6.9)	20.9 (4.4)	16.1 (3.3)	8/10	16%
20150830	04:11	04:41	-44.2	146.78	open MCC	61.1 - 61.4	Yes	88%	0.980	3.1%	35.4 (14.5)	16.4 (7.2)	25.8 (3)	23 (3)	22/29	37%
20151001	04:12	04:42	-44.3	146.46	closed MCC	51.7 - 52	No	0%	0.001	0.8%	7.5 (4.9)	15.1 (8)	20.3 (5)	12.7 (1.6)	16/19	19%

<sup>1)</sup> MCC: Mesoscale Cellular Convection <sup>2)</sup> CM\_SPI: MODIS Cloud\_Mask\_SPI (subpixel heterogeneity index) SDS for 2.1 μm channel. Band 1 (0.66 μm) and band 2 (0.86 μm).

---

### 4.2.2 MODIS data

MODIS level-2 (L2) cloud top and optical product (earth science data set MYD06 for Aqua) is employed for cloud properties at a 1 km x 1 km spatial resolution at nadir. Notable changes to the C6 cloud property retrieval algorithms (Platnick *et al.*, 2017) pertinent to this study include: 1) improved shortwave-derived cloud thermodynamic phase; 2) separate cloud effective radius retrievals from the 1.6, 2.1, and 3.7  $\mu\text{m}$  channels; 3) processing partly cloudy pixels and cloud edges; 4) a new cloud radiative transfer look-up table including for more optically thin clouds; and 5) retrieval failure metrics that provide diagnostic information for the failure. A comprehensive description of the collection 6 reprocessing for Aqua MODIS can be found in Platnick *et al.* (2015; 2017).

It is necessary to determine the cloud-top thermodynamic phase initially, to remove mixed phase and glaciated clouds before moving on to analyse  $N_d$  and  $r_{eff}$ . MODIS C6 products include two cloud phase algorithms; a solely tri-spectral infrared (IR) based algorithm (Baum *et al.*, 2012) reportable for both daytime and night-time and a daytime-only product (cloud phase optical property (CPOP) that uses a combination of visible, shortwave IR and IR channels (Marchant *et al.*, 2016). The IR algorithm uses brightness temperature and emissivity ratios from three different band pairs (8.5, 11, and 12  $\mu\text{m}$ , Baum *et al.*, 2012). The tri-spectral IR algorithm of C6 has become more sensitive than previously and is reported to be better able to discriminate optically thin ice clouds and low-level clouds comprised of supercooled liquid water and mixed phase (Baum *et al.*, 2012). The tri-spectral IR based algorithm runs in parallel with the cloud top property retrievals. Compared to C5, the CPOP algorithm has been completely rewritten to improve the phase discrimination skill for a variety of cloudy scenes (e.g., thin/thick clouds, over ocean/land/desert/snow/ice surface, etc.) (Marchant *et al.*, 2016). The CPOP algorithm uses a simple voting methodology that takes into account all available phase information such as cloud-top temperature, effective radius, 1.38- $\mu\text{m}$  cloud mask

---

test, and IR phase decision (Marchant *et al.*, 2016) and provides the final cloud phase decision. The C6 cloud phase decided by this algorithm is reported to be greatly improved over C5, especially for low maritime broken cloudy scenes (Marchant *et al.*, 2016). The improvements are mainly due to a variety of shortwave-infrared based tests, in addition to information from cloud top and IR phase retrievals and phase test thresholds optimized via continual evaluation with the collocated CALIOP cloud products.

The MODIS clear sky restoral (CSR) algorithm provides four categories for cloud mask; overcast (CSR = 0), partially cloud-covered (CSR = 1), at cloud edge (CSR = 3), and clear sky (CSR = 2). C6 has a newly defined modifier “partly cloudy” (PCL) which indicates the pixel being either ‘CSR = 1’ or ‘CSR = 3’. Earlier versions did not distinguish between cloud edge and partially cloud-covered. Cloud edge pixels were excluded in C5 MODIS retrievals, while C6 attempts to retrieve cloud optical and microphysical properties on these pixels (Platnick *et al.*, 2017).

Cloud top and optical properties examined in this study include cloud-top temperature (CTT), cloud-top pressure (CTP), and cloud-top height (CTH). Cloud effective radius ( $r_{eff}$ ) is the major cloud optical and microphysical property used. Cloud phases have been investigated with the cloud phase infrared (IR) and cloud phase optical property (CPOP). The science data set (SDS)s providing critical information for analysis are solar zenith angle (SZA), cloud multi-layer flag (CMLF), cloud mask sub-pixel heterogeneity index (CM\_SPI) that is used to examine cloud heterogeneity and retrieval failure metric. The Level-1 geolocation products (MYD03) are also used to align the longitude and latitude at a 1 km x 1 km spatial resolution.

To infer cloud droplet number concentration ( $N_d$ ) which is not directly retrieved from the MODIS observations, equation (1) is used (Grosvenor & Wood, 2014; Huang *et al.*, 2016). This method is modified from that used in Boers *et al.* (2006) and Bennartz

---

(2007).

$$N_d = \frac{2\sqrt{10}}{k\pi Q^3} \left( \frac{c(T,P)COT}{\rho_l r_{eff}} \right)^{\frac{1}{2}} \quad (1)$$

$$k = \left( \frac{r_v}{r_{eff}} \right)^3$$

where  $r_{eff}$  and  $r_v$  are the cloud top effective and volume mean radius, respectively.  $Q$  is scattering efficiency. Constants, 0.8 for  $k$  and 2 for  $Q$ , are adopted for the calculation as in Bennartz (2007), Grosvenor and Wood (2014) and Huang *et al.* (2016).  $\rho_l$  is liquid water density ( $1.0 \text{ kgm}^{-3}$ ); and  $c$  is the temperature and pressure-dependent condensation rate. The  $c^{1/2}$  curve in the supplement material in Huang *et al.* (2016) is used.

### 4.2.3 CALIOP data

In addition to the MODIS IR and CPOP thermodynamic phase products, this study also examines cloud top phase retrievals from CALIOP (Winker *et al.*, 2009). The CALIOP payload aboard CALIPSO was launched in April 2006 and consists of a near-nadir viewing two wavelength polarization-sensitive lidar. It measures the backscatter at 532 and 1064 nm and linear depolarization ratio at 532 nm. The depolarization of the lidar backscatter signal is found to be highly efficient in discriminating the ice and water phases of cloud due to their different depolarization behaviors (Hu *et al.*, 2009). This study uses CALIPSO version 4.1 (V4) lidar level 2 cloud layer products (Vaughan *et al.*, 2017). Layers in the 1-km horizontally-resolved product are identified as clouds by the Cloud Aerosol Discrimination (CAD) algorithm. Layers identified as clouds are further classified according to thermodynamic phase as either water, randomly-oriented ice (ROI), horizontally-oriented ice (HOI) or unknown phase. Among the improvements in V4 over the previous version are cloud subtyping and ice-water phase determination as well as the elimination of known retrieval artefacts.

---

#### 4.2.4 Collocation methodology

Given that the A-train satellites move at a far greater speed than the aircraft, they are roughly collocated for only an instant. To make the comparison statistically robust, both the satellite and *in-situ* observations are considered over an extended period. Aircraft observations are extended to a 30-minute window centred at the time of the A-train overpass. This 30-minute window is, typically, a much shorter period of time than the full records used in chapter 2 and 3. We note that Min *et al.* (2012) employed a 60-minute window, but the aircraft could be relatively far away from the A-train overpass over such a long period. Horizontally, MODIS pixels up to 10 km away from the aircraft are considered for comparison with the *in-situ* observations (Figure 4.1 (b)). Vertically, the MODIS pixels within  $\pm 50$  hPa and  $\pm 500$  m of the 30-minute aircraft track are considered to be collocated. Menzel *et al.* (2008) estimate an error in CTH/CTP of up to 1 km (or 50 hPa) using airborne lidar, CALIOP and High Resolution Infrared Radiometer Sounder (HIRS, Wylie & Menzel, 1999); Holz *et al.* (2008) estimated the error in CTH to be  $1.4 \pm 2.9$  km using CALIOP. The spatiotemporally coincident images of a flight track and MODIS retrievals are shown in Figure 4.1 (b), (d) and (f) with MODIS ‘overcast’, ‘PCL’ and ‘overcast + PCL’ pixels. The liquid (red) and mixed phase/ice (blue) cloud samples on the flight track suggest that the cloud was primarily liquid; mixed phase/ice was only observed 8% of the time (Table 4.1). The MODIS pixels are within  $\pm 50$  hPa and  $\pm 500$  m vertical distance from the aircraft altitude with  $\pm 25$  hPa vertical resolution.

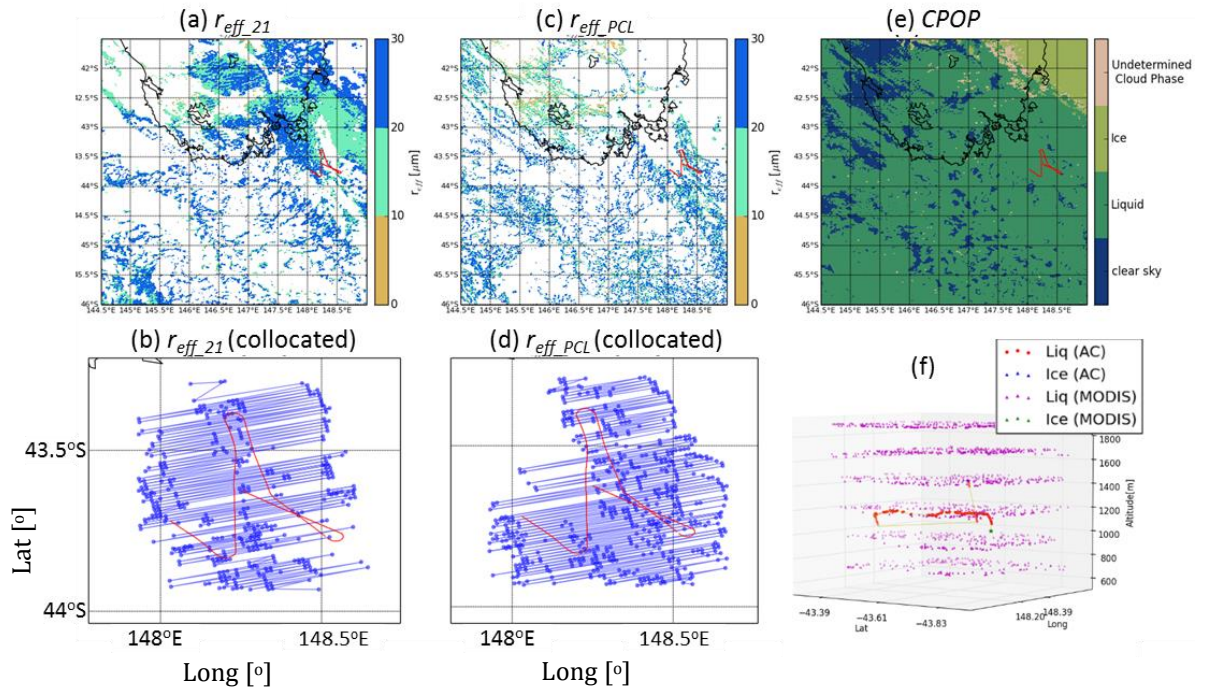


Figure 4.1. Composite images of longitude-altitude cross section of aircraft flight track for 20130614 on spatiotemporally coincided Aqua MODIS retrieval map.

The flight track is plot in red on the MODIS retrieval map of (a)  $r_{eff\_21}$  (overcast) and (c)  $r_{eff\_21}$  (PCL). When the MODIS pixels are spatially aligned with aircraft altitudes as described in section 4.2.4 Collocation methodology, the coposite images are in (b) and (d) for MODIS overcast and PCL pixels respectively. (d) The MODIS cloud phase optical properties (CPOP) is illustrated with aircraft track. (f) The 3-D image of flight track indicated with the cloud thermodynamic phase composited with MODIS CPOP pixels of overcast + PCL.

Most of analysis has been made on pressure levels rather than altitude given that pressure is the first retrieval parameter for MODIS while the altitude needs to be derived from the pressure. For convenience, many of the figures in this study are illustrated with altitude as the vertical variable.

For a comparison of cloud thermodynamic phase with CALIPSO, the same 30 minute *in-situ* records are employed. As CALIOP actually lags MODIS by  $\sim 135$  seconds, we have adjusted the CALIPSO observations accordingly. Like MODIS, a  $\pm 10$  km along-track window is used

---

### 4.3 Cloud thermodynamic phase

Table 4.2 summarises the compositions of cloud thermodynamic phase from aircraft measurements and the retrievals from the CALIOP, MODIS IR and MODIS CPOP products for each flight. Although the table is presented quantitatively, differences in the sampling volume and measurement platforms limit any direct comparison. A qualitative analysis may be more appropriate. The differences in the sampling volume for all eleven flights are provided in the appendix (Figure A3.)

As in section 2.3, the ice-water fraction,  $\mu_3$ , is employed to define the level of glaciation within a cloud sample. Again, following Korolev *et al.* (2003), liquid clouds and mixed phase/ice clouds are sorted by  $\mu_3 \leq 0.1$  and  $\mu_3 > 0.1$ , respectively. The frequency of heavily glaciated cloud samples ( $\mu_3 > 0.5$ ) is also noted. The two closed MCC flights record little, if any, ice. Conversely, three of the eleven flights (20130707, 20130815 and 20131011) contain ice throughout with over 40% of the cloud samples recording  $\mu_3 > 0.1$ . These flights are conventionally called ‘widely iced’ cases, and the ‘substantially iced’ case for the 20140903 flight which has ice of 24% frequency. The ‘substantially iced’ flight was observed to be heavily glaciated 12.5% of the time. The CIP images where ice particles are recorded for these four flights are illustrated in Figure A4 in the appendix.

Table 4.2. Compositions of cloud phase for the eleven flights from 2013 – 2015 discriminated by aircraft measurements, CALIOP retrievals, and MODIS IR and CPOP product. The MODIS cloud phase is separated with single-layer cloud and all clouds including multi-layered clouds determined by MODIS Cloud Multi Layer Flag SDS. Cloud top temperature (CTT) and cloud top height (CTH) are the average values for the ice phase clouds for all cases. The three ‘widely iced’ cases are highlighted.

Flight Date	AC			CALIOP			Single layer						All clouds (single layer + multi layer)					
	samples	Ice [%]		PP	Ice [%]	UD [%]	IR			CPOP			IR			CPOP		
		$\mu_3 > 0.5$	$\mu_3 > 0.1$				PP	Ice [%]	UD [%]	PP	Ice [%]	UD [%]	PP	Ice [%]	UD [%]	PP	Ice [%]	UD [%]
20130614	451	0.0	1.3	34	0.0	5.9	1302	4.5	0.0	1302	0.0	0.0	1567	10.3	0.0	1567	0.0	0.0
20130628	1274	0.3	8.0	56	0.0	1.8	533	8.3	0.1	533	2.1	0.0	1351	10.4	0.1	1351	0.9	1.2
20130707	873	56.0	85.2	51	13.7	2.0	965	31.6	24.8	965	10.7	3.4	3132	43.4	15.0	3131	15.3	7.1
20130723	538	0.0	0.0	142	0.0	0.0	1411	2.1	0.0	1411	0.0	0.0	1464	5.3	0.0	1464	0.0	0.0
20130806	387	1.0	11.6	41	2.4	2.4	680	21.3	9.9	680	6.2	0.6	1193	26.2	9.9	1185	6.3	4.4
20130815	851	9.3	42.7	51	0.0	17.6	1468	81.2	5.4	1468	44.0	3.2	2518	77.3	5.4	2518	25.8	8.0
20131011	291	28.5	54.0	51	0.0	0.0	1423	25.3	42.0	1423	3.5	0.2	4091	63.9	17.8	4091	1.8	3.1
20140903	392	12.5	24.0	71	5.6	1.4	2072	23.3	8.2	2072	2.9	0.4	4107	26.8	5.6	4037	2.0	2.2
20140912	533	0.9	17.6	-	-	-	795	2.9	0.0	795	0.0	0.0	1174	2.3	0.0	1150	0.0	0.0
20150830	893	0.1	3.1	84	0.0	7.1	249	0.0	0.0	249	0.0	0.0	1898	0.1	0.0	1898	0.0	0.0
20151001	261	0.0	0.8	-	-	-	1859	4.2	4.7	1859	0.0	0.0	3437	4.5	3.6	3437	0.0	0.0
CTT [°C]			-5					-2.5			-3			-6.1			-5.4	
CTH [m]			1941					2071			2100			2698			2469	

$\mu_3$ : Cloud Phase Coefficient, PP (pixel population), UD (undetermined)

---

### 4.3.1 CALIOP

The CALIOP cloud phase product was available for only nine of the eleven flights as indicated, and the CALIOP vertical cross-sections for these nine flights are presented in Figure 4.2. Both the full profile and a zoomed profile of the target altitudes are presented. For three of the nine flights, CALIOP intermittently observed randomly oriented ice (possibly cirrus clouds) between the altitudes of 8 and 10 km. These clouds were not sampled by the aircraft. Focussing on the lower altitude clouds that were being sampled by the aircraft, it is evident that liquid water was the primary cloud phase observed by CALIOP for all nine flights. For two of the nine flights (20130723 and 20131011) liquid water was the only cloud phase returned. This is fully consistent with the *in-situ* observations for flight 20130723, where the clouds were at low altitude and the cloud temperature was above freezing, as detailed in chapters 2 and 3. The sampled clouds were observed with closed MCC.

For flight 20131011, however, multi-layered clouds were presented. CALIOP observed cloud top heights at altitudes of 4 to 4.5 km. These clouds were at temperatures far below freezing ( $-15\text{ }^{\circ}\text{C}$ , Figure 4.3) and widespread ice was recorded by *in-situ* observations often with  $\mu_3$  greater than 0.5. The majority of the *in-situ* observations were actually made at a much lower elevation ( $\sim 1500\text{ m}$ ). The CALIOP signal was fully attenuated by the liquid clouds at the higher altitude and did not observe the underlying clouds observed by the aircraft, which may help explain the difference in the phase observations. Flight 20130707 was another ‘widely iced’ flight and has similarities with 20131011. This flight also observed clouds at  $\sim 2000\text{ m}$  and temperatures below freezing. Again, liquid cloud phase is dominant in CALIOP retrieval although a few randomly oriented ice (ROI) and unknown/not determined (UK/ND) classes were recorded. It is interesting to note that a section of ROI is found directly underneath the overlying clouds. Huang *et al* (2012a) noted that the CALIOP cloud phase classification

---

of low level clouds over the SO was sensitive to the presence of overlying ice clouds.

The third ‘widely iced’ flight, 20130815, is once again predominantly seen as liquid by CALIOP, although some UK/ND is observed. No ROI was observed by CALIOP, contrary to the *in-situ* observations. It is evident that even when ice is widely present through the low-level clouds over the SO, CALIOP predominantly returns liquid as the cloud phase. Because the aircraft did not make comprehensive observations of the cloud phase, it is not clear whether this issue with CALIOP occurs consistently.

The remaining five flights have a relatively low occurrence of mixed phase cloud samples ( $\mu_3 > 0.1$ ). Here again, CALIOP predominantly returns liquid as the cloud phase with UK/ND and ice being rarely recorded. The fraction of ice (either ROI or HOI) and UK/ND for all nine flights are provided in Table 4.2. As discussed, liquid is dominant. In general, the CALIOP retrievals do not agree well with aircraft ice observations for the three ‘widely iced’ flights when they are compared either quantitatively or qualitatively. CALIOP records ice in cloud for only one out of these three flights. While the sample size is quite small, there is no evidence of a strong relationship between the presence of *in-situ* ice particles and the CALIOP retrieval of cloud thermodynamic phase. The comparisons also illustrate that low-lying clouds over the SO may readily be missed by CALIOP due to extinction of the lidar signal through optically thick liquid clouds at higher altitudes (Huang 2012b; Chan and Comiso, 2011).

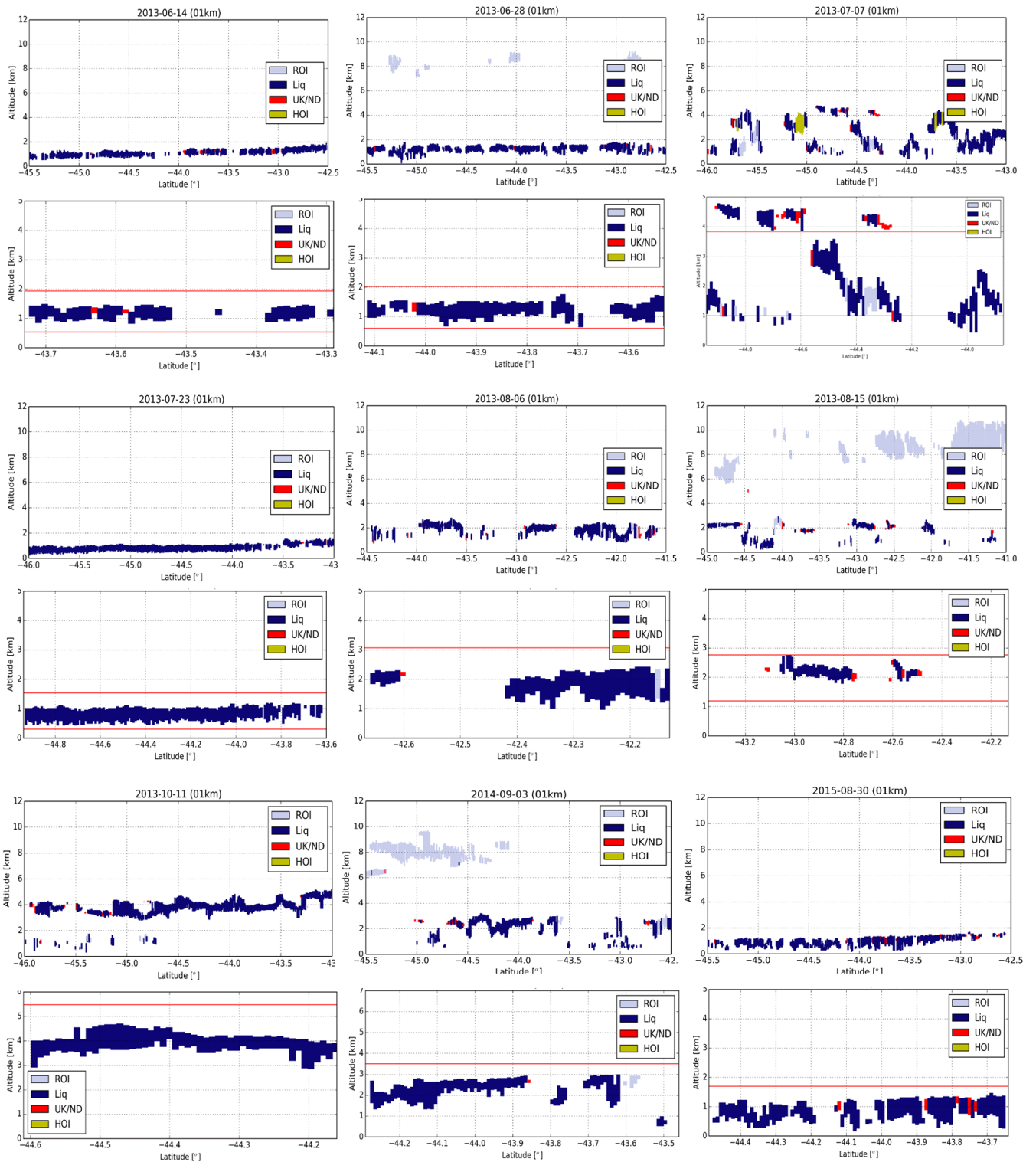


Figure 4.2. Vertical profiles of the CALIOP cloud phase for nine flights from 2013 – 2015. Each flight has two CALIOP profiles; first profile with high altitude and second profile with low altitude zoomed in the target coincided area. The red line on the second profile indicates the coincided altitudes with the aircraft track. ROI, HOI and UK/ND mean “randomly-oriented ice”, “horizontally-oriented ice”, and “unknown / not determined”.

---

### 4.3.2 MODIS

The MODIS cloud-top thermodynamic phase products (IR and CPOP) are compared with the *in-situ* observations. A further distinction between single cloud layer pixels and multiple cloud layer pixels is made as defined by the Cloud\_Multi\_Layer\_Flag (CMLF) (Pavolonis and Heidinger, 2004; Wind *et al.*, 2010; Joiner *et al.*, 2010). CMLF = 1 indicates a single-layer cloud, CMLF  $\geq 2$  indicates multi-layer clouds, and CMLF = 0 indicates no cloud. The pixel population (PP) for single-layer clouds versus all clouds (single and multi-layer) reveals that multi-layer pixels are, on average, more common for these 11 flights, although this varies considerably from flight to flight.

Firstly for the IR single-layer observations, a qualitative agreement is found with the *in-situ* observations. The three ‘widely iced’ flights have the greatest percentage of ice and undetermined (UD) pixels for the single-layer IR product. When combined, ice and UD pixels account for a minimum of 56% of the PP for each of these flights. Similarly, the fourth flight with substantial icing (20140903) also has 31.5% of the PP as ice and UD. Flights with less *in-situ* mixed phase cloud samples tend to have a smaller percentage of the PP recorded as ice and UD for the single-layer IR product. However, when only “ice” classified pixels are included with  $\mu_3 > 0.5$ , only one case (20130707) from the four iced cases has less (12.6%) frequent ice than *in-situ* observations and the rest three cases overestimate the aircraft measurements by  $\sim 2 - \sim 8$  times.

Next, for the CPOP single-layer retrievals, a much lower PP percentage of ice and UD pixels is observed compared to that of the IR product. For the three “widely iced” flights, the ice and UD PP percentage drops from 56.4 to 14.1%, 86.6 to 47.2% and 67.3 to 3.7%, respectively. Quantitatively, it did not agree well with *in-situ* observations although it showed a certain level of ‘internal’ consistency, qualitatively. That is, the ice fraction of the CPOP for the iced flights is higher than that for the other flights. The

---

CPOP product underestimated the *in-situ* ice like the CALIOP product. This is understandable as CALIOP observations have been employed in the development of the C6 MODIS dataset (Platnick *et al.*, 2015; 2017).

Among the iced flights, two have relatively small optical thickness, compared to the rest of the flights. While in one of the relatively thin cloud cases, 20130815 (COT ~8 in Figure 4.6), the MODIS CPOP product overestimated aircraft ice phase observations by 4.7 times, in the other case of 20140903 (COT ~10 in Figure 4.6), it underestimated the *in-situ* ice by 4.3 times in the condition of  $\mu_3 > 0.5$  with single-layer clouds. But in the other optically relatively thicker cases, 20131011 (COT ~18) and 20130707 (COT 50 - 60), it underestimated the aircraft ice measurements by ~8 times and ~5 times respectively. It is noted that the CTT from the MODIS is always higher than the aircraft's. Since the new C6 CPOP algorithm employs a voting methodology in which the weight of CTT is relatively high, the warm temperature (CTT > -4 °C) of the two ice-underestimated cases may have influenced the CPOP retrievals to return liquid rather than ice (Huang *et al.*, 2016), although potential errors from the CTT-CTH conversion in the MODIS product cannot be completely ruled out. These CPOP cloud phase results show that the algorithm still encounters a problem of determining cloud phase when there are relatively thin clouds over a warm surface.

The analysis is now expanded to consider all cloud pixels (single-layer + multi-layer). Focussing first on the IR product, the percentage of ice pixels increases for nine of the ten flights. In general, the percentage of UD pixels decreases when multi-layer pixels are included. Overall, this is still a rough agreement between the *in-situ* observations and the IR phase product. The three 'widely iced' flights have the largest percentage of ice pixels. For the CPOP product, the extension to include multi-level pixels produces an increase in the UD pixel percentage. It is of interest that there is not a systematic change in the ice pixels, as multi-layer clouds present a challenging situation for passive retrievals (Korolev *et al.*, 2017). Regardless of the CMLF flag, the

---

thermodynamic phase results from the IR product is closer to the *in-situ* observations, while those from the CPOP product is closer to the CALIOP product results.

#### 4.4 Cloud Microphysics

The cloud microphysics properties ( $r_{eff}$  and  $N_d$ ) are next considered, employing MODIS cloud property retrievals. To appreciate  $r_{eff}$  and  $N_d$  of the liquid cloud over the SO, it is worthwhile to first investigate the frequency and causes of failed MODIS cloud property retrievals (Cho *et al.*, 2015, hereafter Cho15). The cloud observations are filtered for liquid only observations for both *in-situ* measurements and MODIS retrievals using the cloud phase parameter,  $\mu_3$ , and the CPOP product, respectively. For MODIS property retrievals, only single-layer clouds are included to minimize the retrieval bias (Wind *et al.*, 2010; Huang *et al.*, 2016; Platnick *et al.*, 2017).

The single-layer liquid cloud pixel population detected by MODIS and the retrieval failure rates on  $r_{eff}$  are detailed in Table 4.3 for the 2.1 and 3.7  $\mu\text{m}$  channels. The 1.6  $\mu\text{m}$  channel is not detailed as its pixel population is relatively small (~25% of the 3.7  $\mu\text{m}$  pixel population). Also, observations from the 1.6  $\mu\text{m}$  channel on Aqua MODIS are reconstructed so it should be treated with greater caution. Beyond the photon vertical penetration depth, the pixel population (PP) for each channel may vary due to a number of channel-dependent sensitivities. The cloud inhomogeneity/sub-pixel variability (Zhang & Platnick, 2011; Zhang *et al.*, 2012), 3-D radiative effects (Davis & Marshak, 2010) and atmospheric transmittance corrections (Zhang & Platnick, 2011; Zhang *et al.*, 2012) may all affect the failure rate (Cho15). With 1 year of Aqua MODIS C6 product, Cho15 reported that the 3.7  $\mu\text{m}$  channel PP was approximately 7% greater than the 2.1  $\mu\text{m}$  PP. Our results are opposite to this although the difference is very small, with the 2.1  $\mu\text{m}$  PP (10004) being slightly greater than the 3.7  $\mu\text{m}$  PP (9882), a difference of approximately 1.2%.

The failure rate is defined as the ratio of the number of pixels retrievals failed to the cloud PP. Overall, the failure rate is 16.6% for the 2.1  $\mu\text{m}$  channel and 14.1% for the 3.7  $\mu\text{m}$  channel. The retrieval failure metric SDS provides the causes of retrieval failures such as “ $r_{eff}$  is too large” or “too small” or “COT retrieval failure”. The majority of the failures were attributed to  $r_{eff}$  being too large, similar to Cho15. As the existence of drizzle mode droplets significantly affects the microphysical properties, such as retrieval differences in each MODIS channel and its pixel population, (Nakajima *et al.*, 2010a, Lebsock *et al.*, 2011; Zhang *et al.*, 2012; Zheng *et al.*, 2011; Zhang & Platnick, 2011), flights were identified as drizzling or non-drizzling by the drizzle fraction and rain rate (Table 4.1).

Table 4.3. MODIS  $r_{eff}$  retrieval failure rates for drizzling/non-drizzling flights and cloud regime (overcast and PC) spatiotemporally aligned with *in-situ* observations from eleven flights from 2013-2015.

The failure rate is broken down with failure causes. All calculations are for single-layer liquid clouds determined by the MODIS CPOP product.

Channel	Drizzling/ Cloud regime	Cloud PP (Liq)	Failure Rate				$r_{eff}$ retrieval success PP
			$r_{eff}$ too large	$r_{eff}$ too small	COT failure	Total	
2.1 $\mu\text{m}$ channel	Drizzling Flights	4291	19.1%	1.1%	0.3%	20.5%	3412
	Non-drizzling Flights	7702	13.1%	1.0%	0.3%	14.4%	6592
	Total	11993	15.2%	1.1%	0.3%	16.6%	10004
	Overcast	8218				15.0%	6984
	PCL	3775				19.8%	3027
3.7 $\mu\text{m}$ channel	Drizzling Flights	4033	18.2%	1.3%	0.3%	19.8%	3235
	Non-drizzling Flights	7476	9.7%	1.1%	0.3%	11.1%	6648
	Total	11509	12.7%	1.1%	0.3%	14.1%	9882
	Overcast	7855				12.6%	6862
	PCL	3654				17.3%	3021

---

There are 6 non-drizzling (20130614, 2013077, 20130723, 20130815, 20131011 and 20151001) and 5 drizzling flights (20130628, 20130806, 20140903, 20140912 and 20150830). Note that in this analysis, drizzle does not include potential ice precipitation, which may occur in both non-drizzling (20130707 20130815 and 20131011) and drizzling cases (20130806, 20140903 and 20140912) (Table 4.2). For both the 2.1 and 3.7  $\mu\text{m}$  channels, the failure rate for drizzling flights is substantially greater than for non-drizzling flights. As drizzle arises from large droplets, it follows directly that the increased MODIS retrieval failure is attributed to  $r_{\text{eff}}$  being too large.

It is also readily possible to identify the sensitivity of the failure rate to cloud regime by sorting the cloud pixels into ‘overcast’ pixels and partly cloudy (PCL) pixels. Consistent with Cho15, the failure rate is greater for PCL pixels, although to a much less extent than their analysis over global marine liquid cloud. Our analysis shows the failure rate for PCL pixels is 1.3 times higher than overcast pixels, and that from Cho15 is 6.9 times. Note also the success PP ratio of PCL over overcast. When it is compared with global marine clouds from Cho15, the clouds we observed have a much higher ratio, which means having relatively more PCL than overcast pixels.

The failure rate of the MODIS algorithms has also been found to be sensitive to the cloud mask sub-pixel heterogeneity (Cho15), which is recorded in the C6 collection as CM\_SPI. Formally CM\_SPI is defined as a ratio of the standard deviation to the mean of the measured reflectances of the sixteen 250 m resolution sub-pixels within the 1 km MODIS footprint (Liang *et al.* 2009). The average CM\_SPI from band 1 (0.66  $\mu\text{m}$ ) and band 2 (0.87  $\mu\text{m}$ ) is also listed in Table 4.1. The greatest SPIs are recorded for flights 20130707, 20130806 and 20150830, all open MCC flights. They all have relatively higher retrieval failure rates than the rest of the flights (Table 4.1).

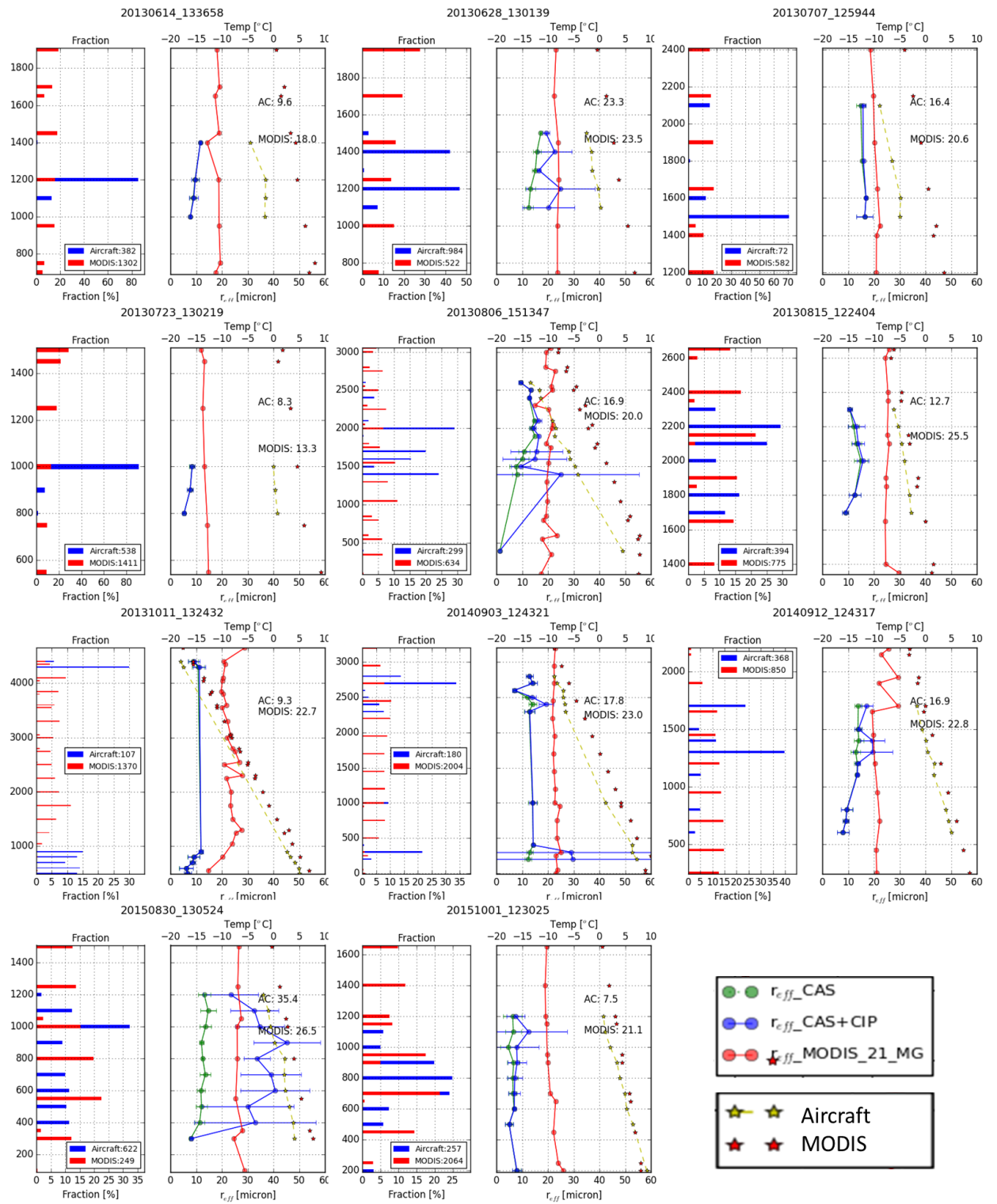


Figure 4.3. Vertical profiles of  $r_{eff}$  from spatiotemporally coincided aircraft measurements and MODIS retrievals for eleven flights from 2013 – 2015.

The  $r_{eff}$  for each altitude is average identified by closed circle and the standard deviation by error bars. The data fraction for each altitude are shown in the “Fraction” panel and

---

number of data samples for aircraft and MODIS pixels are indicated in the box. The MODIS  $r_{eff\_21}$  is retrieved from the combined pixels with overcast and PCL. The average temperature from the aircraft and the MODIS is also depicted with star shape of yellow and red colours respectively.

---

#### 4.4.1 MODIS Cloud $r_{eff}$

Limiting the sampling to liquid-only *in-situ* observations and MODIS pixels, a comparison can be made for  $r_{eff}$  (Table 4.1). Overcast and PCL pixels are combined for the MODIS calculations. For each flight, the mean MODIS effective radius is calculated for the 1.6, 2.1 and 3.7  $\mu\text{m}$  channels. In general, the *in-situ*  $r_{eff}$  is smaller than the MODIS products, although there are some exceptions: for 10 of the 11 flights, the *in-situ*  $r_{eff}$  is smaller than the  $r_{eff\_2.1}$ , for 7 of the 11 flights, the *in-situ*  $r_{eff}$  is smaller than  $r_{eff\_3.7}$  and  $r_{eff\_1.6}$ . The range of the average *in-situ*  $r_{eff}$  over the 11 flights is from 7.5 to 35.4  $\mu\text{m}$ , whereas the range of the  $r_{eff}$  for MODIS is much smaller ( $\sim 12.6$  to 25.8  $\mu\text{m}$ ). In all, except for one flight (20130723),  $r_{eff\_2.1}$  is greater than  $r_{eff\_1.6}$  or  $r_{eff\_3.7}$ . The  $r_{eff\_1.6}$  and  $r_{eff\_3.7}$  are broadly consistent, being within 20% of each other for 10 of the 11 flights.

It is appreciated that the photon penetration depth of the different channels is sensitive to the size of the droplets, which underpins differences between  $r_{eff\_2.1}$  and  $r_{eff\_3.7}$  (Nakajima *et al.*, 2010a; Suzuki *et al.*, 2010; Zhang and Platnick, 2011), especially for marine liquid clouds (Nakajima *et al.*, 2010b). Specifically,  $r_{eff\_3.7}$  has been found to be smaller than either  $r_{eff\_2.1}$  or  $r_{eff\_1.6}$  when small cloud droplets are located near cloud-top.

Like the *in-situ* observations, the MODIS  $r_{eff}$  is sensitive to the presence of drizzle, but not as strongly. Figure 4.4 illustrates the comparison between the *in-situ*  $r_{eff}$  for the three MODIS channels for overcast, PCL and combined pixels (overcast + PCL). In general, non-drizzling flights (circles) are clustered in the left side of the diagrams. On average, the difference between the *in-situ*  $r_{eff}$  and the MODIS  $r_{eff}$  is higher for the non-drizzling flights.

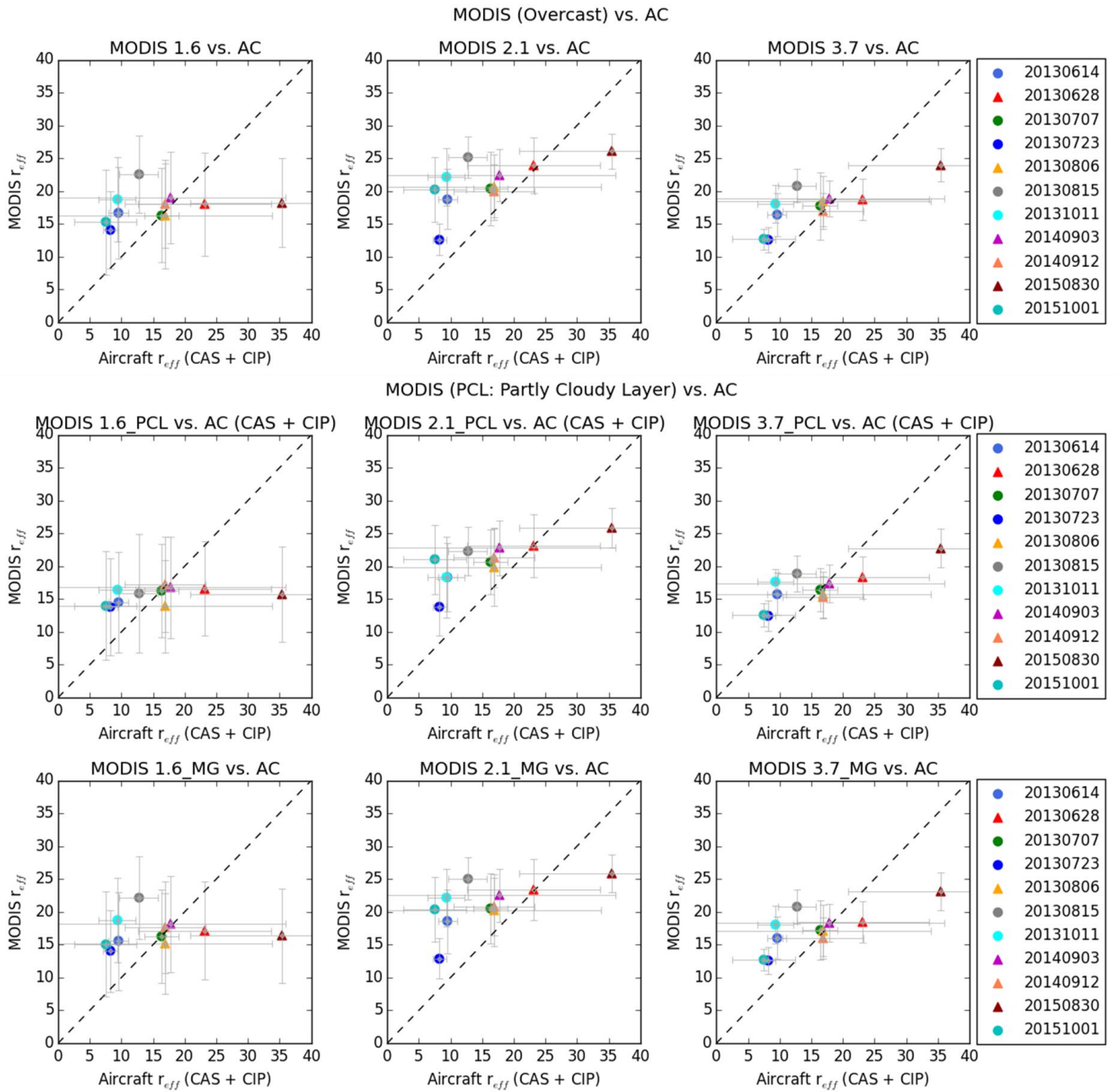


Figure 4.4. Comparison of liquid cloud effective radius ( $r_{eff}$ ) retrieved from Aqua MODIS with *in-situ* measurements from CAS + CIP. The MODIS  $r_{eff}$  is retrieved by channel (each column) and by cloud regime (each row).

The first row is for “overcast”, second row for “PCL”, and third row for “merged” (overcast + PCL) pixels. The horizontal bars and vertical bars represent standard deviations of cloud  $r_{eff}$  from CAS+CIP and MODIS, respectively. The dashed lines represent 1:1 lines. Non-drizzling flights and drizzling flights are indicated as circles and triangles, respectively.

---

The  $r_{eff}$  (CAS + CIP) for non-drizzling cases ranges from 7.5 – 16.4  $\mu\text{m}$  and for drizzling cases from 17 – 35  $\mu\text{m}$ . Whilst the MODIS  $r_{eff\_2.1}$  ranges from 12.9 – 25.1  $\mu\text{m}$  and 20.2 – 25.8  $\mu\text{m}$  for non-drizzling cases and drizzling cases, respectively. That is, the range of MODIS  $r_{eff}$  for drizzling cases is relatively smaller than that of the *in-situ* observations whereas the range of MODIS  $r_{eff}$  for non-drizzling cases is larger than that of the *in-situ* observations. Note that the MODIS look-up table limits the droplet effective radius to at most 30  $\mu\text{m}$  for liquid phase clouds, meaning that there is a built-in limitation to the effective radius that MODIS can retrieve. In general, the lightly drizzling flights record smallest differences between the *in-situ*  $r_{eff}$  and the MODIS  $r_{eff}$  with correlation coefficient of 0.959 and 0.891 for  $r_{eff\_2.1}$  and  $r_{eff\_3.7}$ , respectively. This is contrary to Zheng *et al.* (2011) who reported drizzle causes great uncertainty (Zhang & Platnick, 2011) and larger overestimation in the  $r_{eff}$  retrievals than non-drizzling clouds. Both of them used the MODIS C5 dataset.

MODIS  $r_{eff}$  bias may also be sensitive to the SZA, which becomes relatively large during the winter months. Five of the 11 flights have the SZA in excess of 65°, a threshold defined in Grosvenor & Wood (2014) for ‘large’. No systematic biases on  $r_{eff}$  from the SZA are evident from these 11 flights, although the sample size is small with many confounding processes. Further Grosvenor & Wood (2014) estimate that the mean bias is only ~1  $\mu\text{m}$ , which is much smaller than the differences between *in-situ*  $r_{eff}$  and MODIS  $r_{eff}$  for all 11 flights.

A potential constraint limiting a direct, quantitative comparison of the *in-situ* observations with the MODIS products, is the aircraft position within the cloud field, as the cloud droplet size is sensitive to it. While the MODIS (and CALIPSO) products tend to be more sensitive to the cloud-top properties, the aircraft was not constrained to fly near cloud top. In Figure 4.3, the effective radius as a function of altitude is detailed for the 11 flights. Variations in the *in-situ*  $r_{eff}$  with altitude are not identified for some

---

non-drizzling flights which have higher discrepancies with MODIS  $r_{eff}$ , while the magnitude of the *in-situ*  $r_{eff}$  is smaller than that of MODIS  $r_{eff\_2.1}$  across the in-cloud sampling altitudes, except for flight 20150830.

We acknowledge that observing potentially different clouds may lead to differences between the *in-situ* and MODIS  $r_{eff}$ . We also note that the *in-situ*  $r_{eff}$  is smaller at the higher altitudes in a number of flights, possibly a consequence of entrainment across cloud-top.

As discussed in chapters 2 and 3, the *in-situ*  $r_{eff}$  for the nine open/disorganised MCC flights was consistent with the wintertime observations of the SOCEX I (Boers *et al.*, 1998) and two closed MCC flights were highly consistent with the summertime observations (SOCEX II; Boers *et al.*, 1998). The same behaviour is found in the MODIS  $r_{eff}$ , too, particularly for the 3.7  $\mu\text{m}$  channel.

The largest differences between the *in-situ*  $r_{eff}$  and the MODIS occur on flights 20130614, 20130815, 20131011 and 20151001. The *in-situ*  $r_{eff}$  is smaller than 13  $\mu\text{m}$  for all four flights, and none of them experienced significant drizzle. Flight 20130723 also has a small *in-situ*  $r_{eff}$  and does not experience drizzle, but the MODIS  $r_{eff}$  values are in relatively good agreement with the *in-situ*  $r_{eff}$ . Flights 20151001 and 20130723 are the two flights that encountered closed MCC.

Among the non-drizzling flights, flights 20131011 and 20130815 have relatively high  $r_{eff}$ . It was previously noted that flight 20131011 had clouds at higher altitudes (above 4 km) frequently containing ice. Potentially, overlying cirrus can confuse the MODIS retrieval algorithms, if they are not optically thick, which allows retrievals to be comprised of a mix from pixels at different altitudes and temperatures (e.g. Dong *et al.* 2002). The large  $r_{eff}$  of flight 20130815 is also suspected of being affected by optically thin overlying cirrus/ice cloud.

---

The variability of effective radius may impact the satellite retrieval (Platnick and Valero, 1995). As Hansen and Travis (1974) suggested, the changes in the droplet size distribution can be assessed by the standard deviation of a lognormal droplet size distribution ( $s$ ) (e.g. Painemal and Zuidema (2011); King *et al.*, (2013)). The MODIS used  $s = 0.35$  to construct the  $r_{eff}$  look-up table. Chang and Li (2001) and Painemal and Zuidema (2011) showed that the  $r_{eff}$  differences between in-situ observations and MODIS retrievals are sensitive to  $s$ . The log-normal standard deviation in our in-situ observations ranges between 0.16 and 1.26 with mean value of 0.71. The high differences of  $s$  between the MODIS and our measurements may have affected the  $r_{eff}$  comparison.

#### 4.4.2 MODIS Cloud $N_d$

As with the  $r_{eff}$ , the MODIS-derived  $N_d$  can be compared against the *in-situ* observations (Figure 4.5). As discussed in chapter 2, the majority of the clouds sampled in this region have low  $N_d$  with the large  $r_{eff}$ . For nine of the 11 flights in this study, *in-situ* calculations of  $N_d$  were less than  $35 \text{ cm}^{-3}$ . Five of the 11 flights had  $N_d$  less than 20. The two high-concentration outliers are the two closed MCC cases (flights 20130723 and 20151011) with concentrations of 89 and  $80 \text{ cm}^{-3}$ , respectively. As discussed in chapter 2, these *in-situ* observations of low  $N_d$  are consistent with those of SOCEX experiments from 20 years earlier (Boers *et al.*, 1996; 1998).

The MODIS  $N_d$  calculated with the  $r_{eff}$  from the 2.1 and 3.7  $\mu\text{m}$  channels are largely consistent with the *in-situ*  $N_d$  with correlation coefficient (excluding the three outliers) of 0.735 and 0.808 for  $r_{eff_{2.1}}$  and  $r_{eff_{3.7}}$ , respectively. Larger differences are found for the 1.6  $\mu\text{m}$  channel, which can be traced to the high variability in the cloud optical thickness for the 1.6  $\mu\text{m}$  channel (Figure 4.6). As Painemal & Zuidema (2011) reported, a good agreement between the MODIS (2.1 and 3.7  $\mu\text{m}$  channel) and *in-situ*  $N_d$  is

remarkable given that MODIS systematically overestimates  $r_{eff}$ . Comparisons separated into PCL and overcast pixels are also analysed.

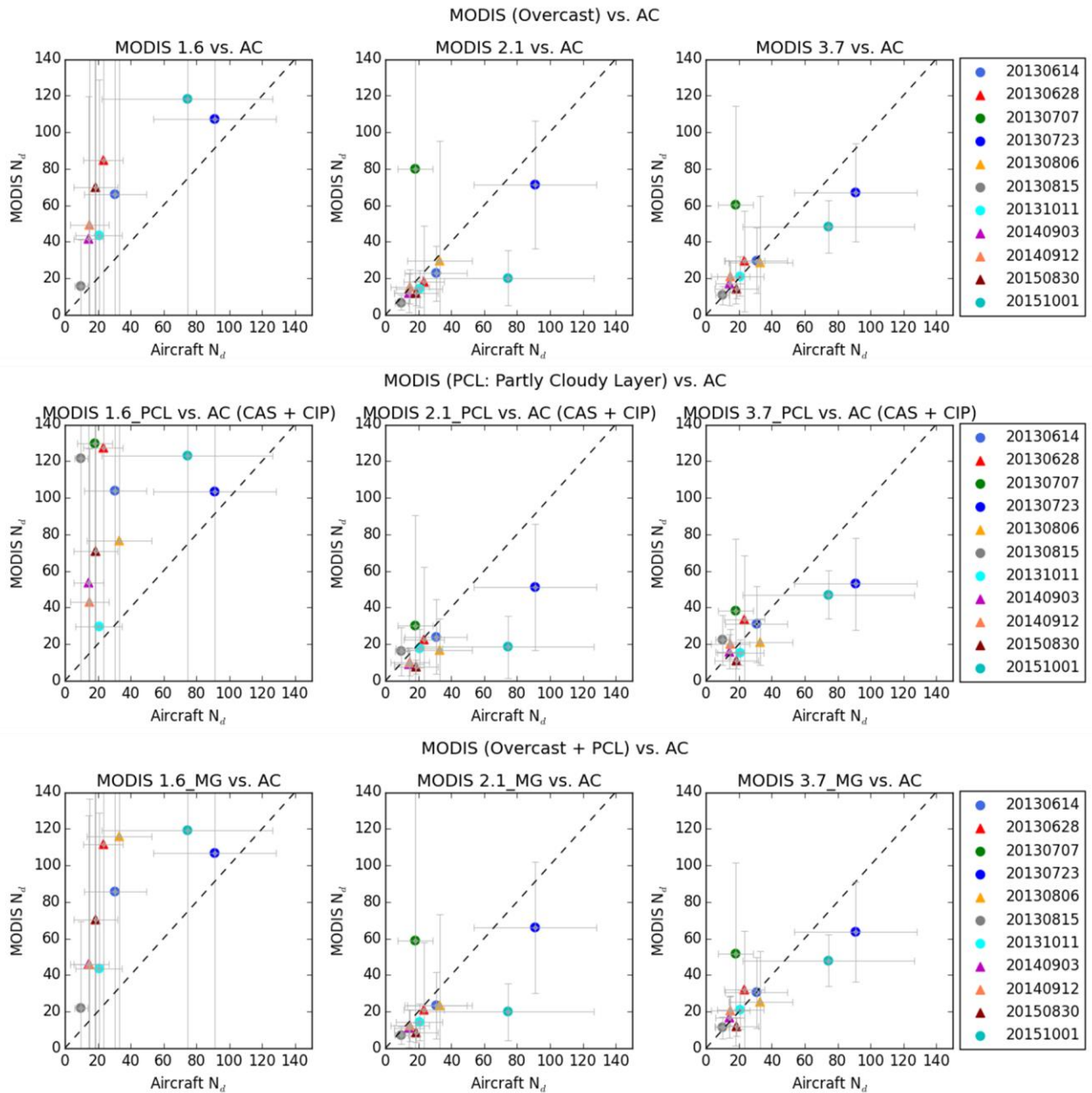


Figure 4.5. Same as Figure 4.4 but for  $N_d$  which is derived by the MODIS retrievals of  $r_{eff}$  and COT.

For eight of the 11 flights, the MODIS calculations more closely follow a one-to-one relationship with the *in-situ* observations for the overcast pixels, as would be expected, although large variability is noted. It is interesting that for the three remaining outlying flights, which include the two high  $N_d$  closed MCC flights, there is actually a better agreement between the MODIS and *in-situ* calculations for the PCL pixels, contrary to our expectations.

However, there are three outliers in the MODIS 2.1 and 3.7  $\mu\text{m}$  channel plots; 20130707, 20130723, and 10251001 cases, all non-drizzling. The large discrepancies of MODIS  $N_d$  for these flights to the *in-situ* are, in part, due to their overestimated  $r_{eff}$ . Overall, the 3.7  $\mu\text{m}$   $N_d$  has a closer agreement with the *in-situ* observations, due to a better agreement for the three outlier flights. It is also noted that for the eight low  $N_d$  flights, there is slightly more variability in the  $N_d$  for the 3.7  $\mu\text{m}$  channel in comparison to the 2.1  $\mu\text{m}$  channel.

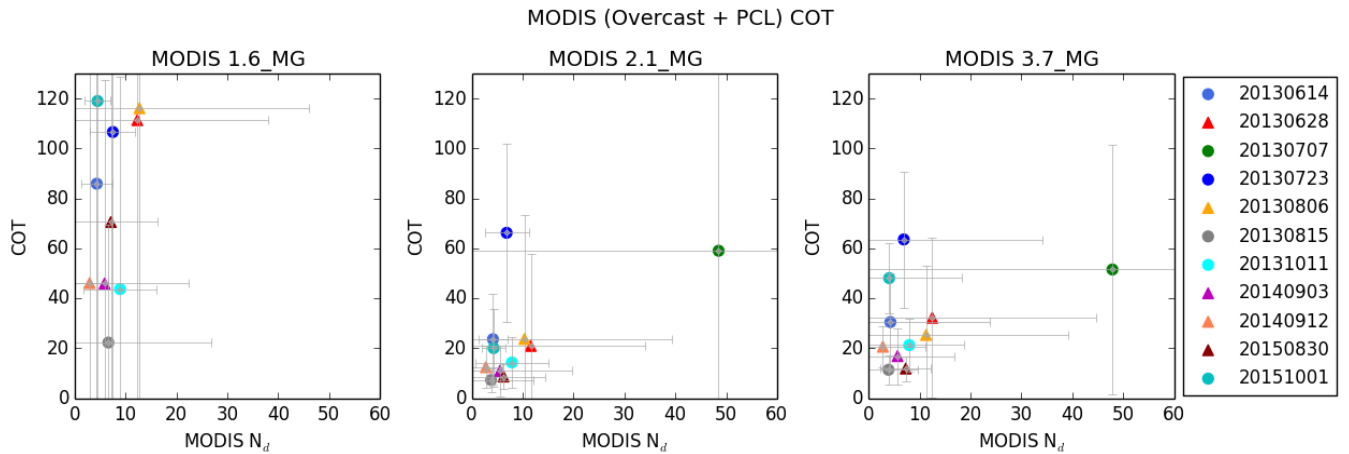


Figure 4.6. Cloud optical thickness (COT) as a function of  $N_d$  for “merged” (overcast + PCL) pixels retrieved from Aqua MODIS and derived from equation (1), respectively. The horizontal bars and vertical bars represent standard deviations of  $N_d$  and COT, respectively. Non-drizzling flights and drizzling flights are indicated as circles and triangles, respectively.

---

## 4.5 Discussions and Summary

The aim of this research has been to employ the *in-situ* observations to better appreciate the skill and limitations of satellite derived products for thermodynamic phase (MODIS and CALIPSO), effective radius (MODIS) and cloud droplet number concentration (MODIS). Such an exercise has been taken over the Southeast Pacific for research flights taken during the VOCALS-REx field campaign (e.g. Zheng *et al.*, 2011; Painemal & Zuidema, 2011; Min *et al.*, 2012; King *et al.*, 2013). We consider eleven research flights taken over three cold seasons (Jun - Oct, 2013-2015) that were timed/designed to pass under A-train observations. The *in-situ* analysis has been limited to a 30-minute window around the timing of the A-train overpass.

While many of the observations made during VOCALS-REx were of warm, boundary layer clouds defined by stratified clouds, the environment over the Southern Ocean is far different. The clouds observed in these flights over winter time have more open or unorganised MCC (Muhlbauer *et al.* 2014) and have a higher (~32%) portion of PCL pixels than global marine clouds (Cho15), meaning that the assumption of horizontal homogeneity is often invalid. Further, these clouds were frequently observed to contain ice, complicating the underlying assumptions. The *in-situ* observations suggest that satellite-based products may have difficulty in retrieving cloud properties over the SO. This was evident in the relatively higher (42% with 3.7  $\mu\text{m}$  channel) failure rate for the MODIS cloud optical property retrievals, compared to the global marine clouds (Cho15), although many of these failures were actually attributed to the droplet radius being too large.

Firstly, the thermodynamic phase of the MODIS IR and CPOP products was examined, as well as CALIOP. Three of the eleven flights encountered mixed phase and ice cloud with over 40% of the cloud samples with  $\mu_3 > 0.1$ . These flights are conventionally called ‘widely iced’ cases and other flight having ice frequency of 24% is called

---

‘substantially iced’ flight.

Out of these four iced cases, the CALIOP retrievals did not show any ice for two cases. One of the two cases had thick liquid cloud overlaid, and the other had overlaying cirrus. The remaining two cases underestimated the aircraft ice measurements ( $\mu_3 > 0.5$ ) by a factor of  $\sim 2 - 4$  times. The CALIOP product primarily returns liquid phase droplets, even at altitudes of 4 km and greater, and at relatively cold cloud-top temperatures ( $-15$  °C). This is consistent with the climatology of Huang *et al.* (2012b), who reported that CALIOP identifies a liquid water cloud-top phase for the majority of the boundary layer clouds over their SO study domain.

The MODIS CPOP phase product, which has been influenced by CALIOP phase discrimination in the C6 data set, behaves comparably; liquid phase is predominantly recorded at cloud-top. Three cases of the four iced ( $\mu_3 > 0.5$ ) flights were underestimated ice by a factor of  $\sim 4.3 - 8$  times by the MODIS CPOP product. However the CPOP product showed an ‘internal’ consistency qualitatively by showing the ice fraction of the CPOP for the ‘iced’ flights to be higher than that from the other flights. The CPOP product was seen to also be challenged for optically thin clouds.

The MODIS IR phase product, however, is in better agreement with the *in-situ* phase observations qualitatively than the CPOP product, but frequently records ice phase in a mixed-phase environment. The MODIS products were not particularly sensitive to whether a single-layer or multi-layer cloud structure was analysed.

Next, the *in-situ* observations were employed to evaluate the effective radius and cloud droplet number concentrations retrieved from the 1.6, 2.1 and 3.7  $\mu\text{m}$  channels on MODIS. The *in-situ* observations revealed that five of the eleven flights were drizzling, two heavily, and the remaining six flights were not observed to be drizzling significantly. Chapter 2 highlighted the common presence of precipitation in these

---

clouds. As would be expected,  $r_{eff}$  was greater and  $N_d$  was smaller for drizzling clouds, overall.

Over the eleven flights, the MODIS  $r_{eff}$  has a much smaller range than the *in-situ* observations. It underestimated  $r_{eff}$  for heavily drizzling clouds by 4.8 – 12.4  $\mu\text{m}$  and highly overestimated  $r_{eff}$  for non-drizzling clouds by 4 – 13  $\mu\text{m}$ . The MODIS  $r_{eff}$  bias was not observed to be particularly sensitive to the solar zenith angle for these flights, i.e. the natural variability of  $r_{eff}$  of the observed clouds was greater than the potential bias identified in Grosvenor and Wood (2014.)

For the six non-drizzling flights, each of the MODIS  $r_{eff}$  products overestimates the *in-situ*  $r_{eff}$  with the  $r_{eff}$  of the 3.7 and 1.6  $\mu\text{m}$  channels performing marginally better than 2.1  $\mu\text{m}$  channel. This is consistent with the observations made over the Southeast Pacific during VOCALS-REx (e.g. Zheng *et al.*, 2011; Painemal & Zuidema, 2011; Min *et al.*, 2012; King *et al.*, 2013), although the magnitude of the overestimate (4 – 13  $\mu\text{m}$ ) is greater (67%) for the observations over the Southern Ocean. In addition to systematic overestimation, part of the issue is assumed to be due to the ice contamination (e.g. Zheng *et al.*, 2011).

For the three lightly drizzling flights, the three MODIS  $r_{eff}$  roughly agree with the *in-situ* observations with high correlation coefficients, while for the two heavily drizzling flights, the MODIS  $r_{eff}$  underestimates the *in-situ* observations. For these two heavily drizzling clouds, droplets with effective radius larger than 30  $\mu\text{m}$  are present, which is an upper limit for the MODIS  $r_{eff}$  algorithm. Accordingly, large MODIS failure rates were noted for these two flights. These heavily drizzling events are likely to be problematic for the MODIS algorithms for a number of reasons. Consistent with King *et al.* (2013), the *in-situ*  $r_{eff}$  (12.8  $\mu\text{m}$ ) in our study was in better agreement with that of the 3.7  $\mu\text{m}$  channel (16.4  $\mu\text{m}$ ) than 2.1 (20.3  $\mu\text{m}$ ) for non-drizzling and lightly drizzling cases. However, for the two high drizzling cases,  $r_{eff_{2.1}}$  (25  $\mu\text{m}$ ) was closer to the *in-*

---

*situ* observations (29  $\mu\text{m}$ ) than that from 3.7  $\mu\text{m}$  channel (21  $\mu\text{m}$ ). We speculate that the 2.1  $\mu\text{m}$  channel captures the larger drizzle drops closer to the cloud base better than the 3.7  $\mu\text{m}$  channel (Nakajima et al. 2010a).

Lastly, the MODIS derived cloud droplet number concentration,  $N_d$ , is largely consistent with the *in-situ* observations in spite of the limitation in  $r_{eff}$ . Remarkably, skill was still evident for heavily drizzling, horizontally inhomogeneous, mixed phase clouds. The two closed MCC flights had the largest values of  $N_d$ , but still underestimated the *in-situ* observations. Overall the  $N_d$  of the 3.7  $\mu\text{m}$  channel was in better agreement with the observations than that of the 2.1  $\mu\text{m}$  channel. The 1.6  $\mu\text{m}$  channel performed poorly, which was attributed to limitations in the retrieval of the cloud optical thickness.

We inferred no specific bias was evident for MODIS retrievals made at large solar zenith angle ( $> 65^\circ$ ) although the sample size is quite limited. In the broken and patchy cloud field mixed with ice, liquid and large drizzling particles, cloud inhomogeneity/variability as well as ice contamination are assumed to play an important role in the  $r_{eff}$  retrieval biases.

---

## Chapter 5

### A Case Study for Drizzle over the Southern Ocean with *In-situ*, GPM, A-Train, and ACCESS Observations

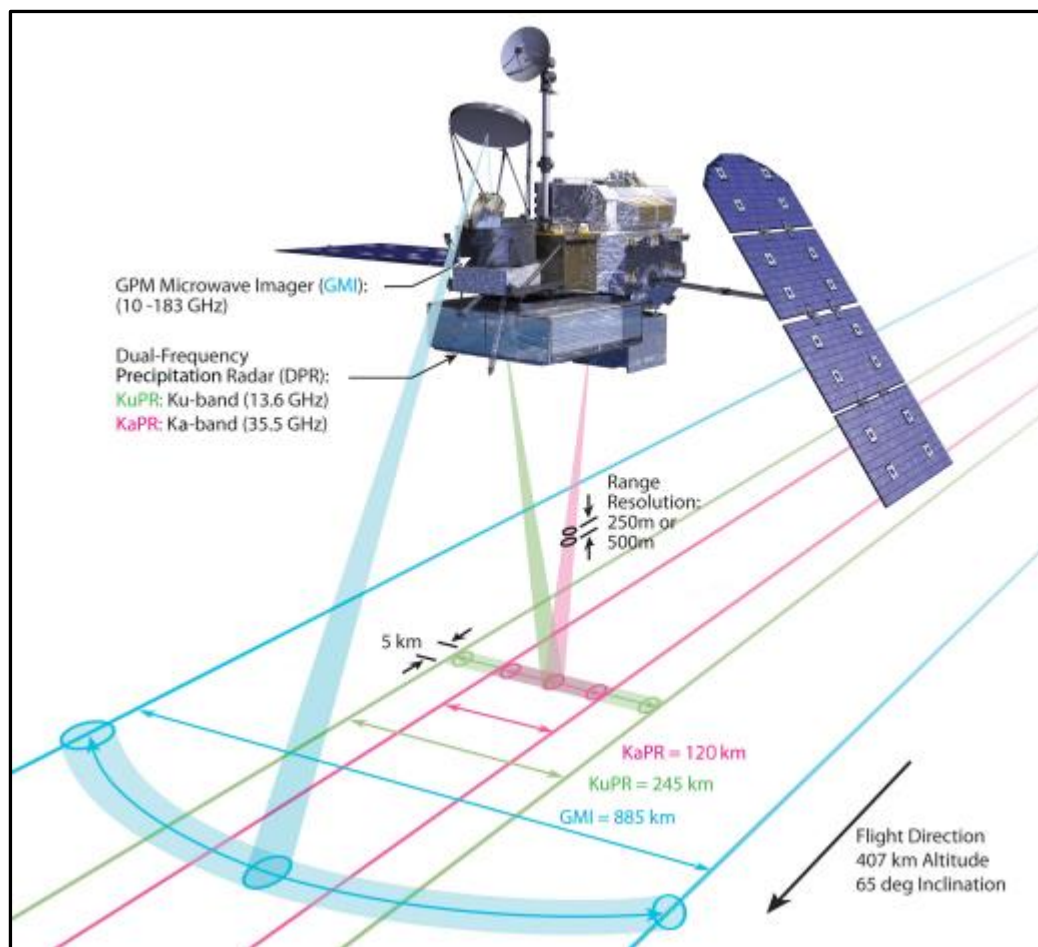


Figure 5.0 Diagram of the Global Precipitation Measurement (GPM) core observatory showing the GPM microwave imager (GMI) and dual-frequency precipitation radar (DPR) instruments. The swath for each sensor is also illustrated.

---

*The research presented in the present chapter is only a preliminary analysis as GPM observations are limited due to the unavailability of the essential Ku/Ka-band radar.*

## **5.1 Introduction**

Precipitation estimation at higher latitudes and over water is a major challenge to the climate community, especially over the Southern Ocean where various estimates differ most (Behrangi *et al.*, 2014). Yet accurate measurement of precipitation over the SO is necessary to close the regional water and energy budgets.

Wang *et al.* (2015) revealed that light precipitation (Rain Rate  $< 0.5\text{mmh}^{-1}$ ) dominates (~82%) the frequency of 3-h surface precipitation according to the ground based measurements on Macquarie Island (54.50 °S, 158.94 °E, 128 km<sup>2</sup> area, located in the midst of the Southern Ocean). This frequent, light precipitation (Ellis *et al.*, 2009) is a challenge to estimate for microwave sensors in satellites. Haynes *et al.*, (2009) and Behrangi *et al.*, (2012; 2014) showed a factor of two differences in the precipitation estimates between cloud radars (e.g., CloudSat) and microwave sensors (e.g., Aqua's Advanced Microwave Scanning Radiometer for Earth Observing System (AMSR-E; Wentz and Meisner, 2000)). The frequent presence of ice and various thermodynamic states such as ice, mixed phase and supercooled liquid water (Chubb *et al.*, 2013) in the clouds over the SO add further uncertainty to the satellite retrievals. Spaceborne precipitation products remain to be verified over this region where the microphysical processes are unique.

The CloudSat Cloud Profiling Radar (CPR; Stephens *et al.*, 2002) and Global Precipitation Measurement (GPM; Huffman *et al.*, 2015a) radar/microwave radiometer are state-of-the-art sensors which have been providing unprecedented estimates of precipitation from snow, drizzle and intense rainfall. The CPR (94 GHz), optimized for

---

vertically profiling clouds, is known to be highly reliable in retrieving ice clouds and light precipitation properties (e.g. Barker *et al.*, 2008; Protat *et al.*, 2010, Berg *et al.*, 2010). Yet, it only provides the limited insight for boundary layer liquid clouds due to the ground clutter effect at altitudes below 720m, and the low sensitivity to small liquid water droplets (e.g. Marchand *et al.*, 2008; Christensen *et al.*, 2013; Huang *et al.*, 2012a, b). Wang *et al.* (2015) compared the surface observations at Macquarie Island against the nearby CloudSat products and found the CloudSat products commonly underestimated the frequency of drizzle and light precipitation. They speculated that the CloudSat might be missing some precipitation from shallow clouds (Huang *et al.*, 2012b).

GPM, launched in 2014, makes frequent (every 2–3 hours) observations of Earth's precipitation and produces a global precipitation analysis. It is built on the successes of the Tropical Rainfall Measuring Mission (TRMM, Berg *et al.*, 2010) program. The GPM core observatory consists of a dual-frequency precipitation radar (DPR; the Ku-band at 13.6 GHz and Ka-band at 35.5 GHz) and a conical-scanning multichannel GPM Microwave Imager (GMI; 10 - 183 GHz, Draper *et al.*, 2015). The GPM sensors are more sensitive to light and solid precipitation than TRMM sensors (Hou *et al.*, 2014) as it has extended the sensor package, which had a single precipitation radar (PR) and a multichannel TRMM Microwave Imager (TMI; 10 - 85.5 GHz). The GMI instrument has 13 channels capturing a wide range of precipitation types. Each channel is sensitive to a different frequency of microwave energy naturally emitted from or affected by precipitation from heavy, moderate and light rainfall/snow and mixtures of both rainfall and snow.

The present case study occurred on 30 August 2015 when the in-situ observations were collocated with both A-Train (Stephens *et al.*, 2002) and GPM constellation overpasses. Both the A-Train and GPM observations were made within a 30-minute window during the mission. The aircraft encountered light to heavy patches of drizzle through the flight.

---

Full details of the microphysics of this ‘heavily drizzling’ flight (20150830) can be found in section 3.3.

In this chapter, the structures of the cloud and drizzle properties seen by airborne and spaceborne sensors are investigated and compared. The results are limited because the retrievals from the Ku/Ka-band radar were not available on this day and only the GMI retrievals were valid. Yet the present case study provides a fresh opportunity to evaluate the GMI capability, which is known to be the most sensitive microwave sensors to the light precipitation. This case study also includes a simulation of drizzle produced by the Australian Community Climate and Earth System Simulator (ACCESS) model. The ACCESS configuration is the same as in Huang *et al.* (2015a, hereafter H15).

## **5.2 Experimental Design and Data**

### **5.2.1 Experimental Design**

The flight for the case study (20150830) is one of the twelve ‘research-only’ flights conducted by the Cessna Conquest employed by Hydro Tasmania Ltd. (Huang *et al.*, 2014; 2015b). An open MCC cloud field was encountered during the flight. The full descriptions of the flight are detailed in section 2.1.

The research flight started 1 hour before the A-Train constellation overpass and stayed on the track until 1 hour after the GPM core satellite had passed. The coincided times for the A-Train and GPM are 0418 - 0432 UTC and 0505 - 0506 UTC, respectively. The composite images of the clouds on the day and the aircraft and satellite tracks are shown in Figure 5.1 (a) – (c). The domain settings for the simulation with the operational ACCESS model is illustrated in Figure 5.1 (d).

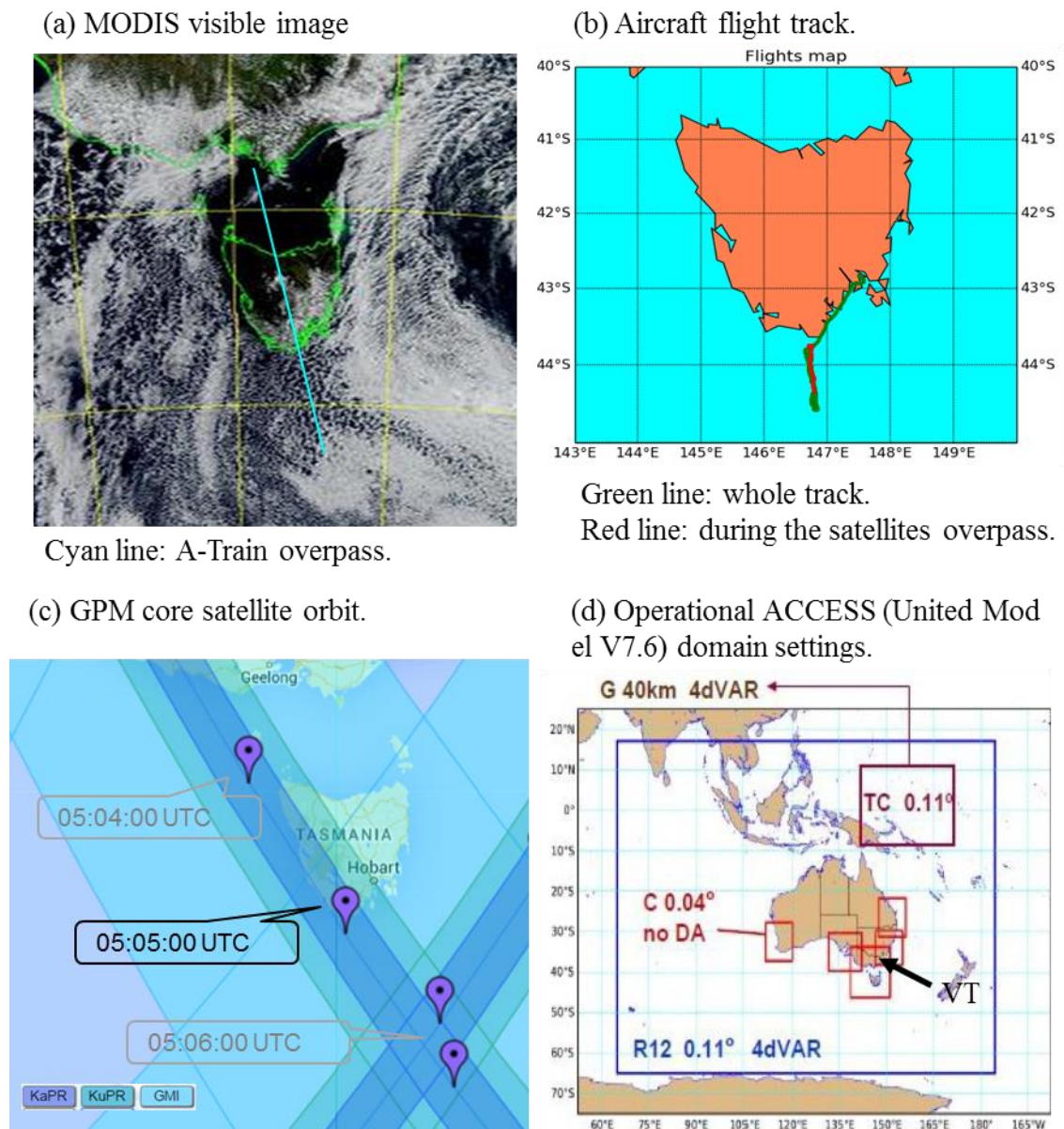


Figure 5.1. Experimental design for the case study for 30<sup>th</sup> August, 2015.

(a) MODIS visible image with A-Train constellation track. (b) Aircraft flight track identifying the points of collocation with the A-Train and GPM overpasses. (c) GPM core satellite orbit with flying time. (d) Operational ACCESS domain settings for the study.

---

## 5.2.2 Data

A full description of the aircraft instrumentation and data used for *in-situ* observations is detailed in section 2.1.2 Aircraft Instrumentation. The definition of drizzle observed by the aircraft is described in section 3.1 Drizzle Fraction and Rain Rate. Rain rate was calculated using the fall speed of the droplets with size greater than 112.5  $\mu\text{m}$  (Pruppacher and Klett, 2010).

MODIS level-2 (L2) cloud product (earth science data set MYD06 for Aqua; Platnick *et al.*, 2015) is employed for cloud top and optical properties. The level 2 Vertical Feature Mask (VFM) product (V3.1.1, Hu *et al.*, 2009) is used for the CALIOP data. The detailed descriptions of the MODIS and CALIOP data are found in section 4.2.

The CPR radar reflectivity is retrieved from the ‘2B-GEOPROF’ product (R04: Mace *et al.*, 2007), and the thermodynamic variables are from the ‘ECMWF-AUX’ (Partain, 2007) reanalysis product. The CPR precipitation is from the ‘2C-PRECIP-COLUMN’ (PC) product (R04: Haynes *et al.*, 2009) and the presence and intensity of the precipitation are derived from the path-integrated attenuation. The more recently developed ‘2C-RAIN-PROFILE’ (RP) product (R04: Mitrescu *et al.*, 2010; Lebsock and L’Ecuyer, 2011) was not available on that date. The CloudSat CPR classifies the precipitation column as ‘certain’, ‘probable’, and ‘possible’. While the rain rate algorithm of the PC product includes ‘probable’ columns, the RP product includes only ‘certain’ columns to avoid the drizzle that does not potentially reach the surface (Lebsock and L’Ecuyer, 2011).

As the first spaceborne Ku/Ka-band DPR of GPM, the Ku-band radar, similar to the precipitation radar (PR; the Ku-band at 13.8 GHz) onboard the TRMM satellite, covers a 245 km swath. The Ka-band radar is nested inside the Ku-band swath and scans a 120 km swath. The GMI has a swath 885 kilometers wide. The swath for each sensor is

---

illustrated in Figure 5.0. The GMI Integrated Multi-Satellite Retrievals for GPM (IMERG, Huffman *et al.*, 2015b) product provides 0.1° spatial and 30 min temporal resolutions. It is designed to leverage the international constellation of precipitation-relevant satellites to create a long record of uniformly time/space gridded precipitation estimates for the globe. The GPM precipitation data employed in the study is the latest IMERG half-hourly final run version 4 product (Huffman *et al.*, 2015c) which is widely used for research purposes.

ACCESS (Puri *et al.*, 2013) is an Australia's climate model based on the UK Met Office Unified Model/Variational Assimilation (UM/VAR) system. The model has been developed and tested by the Australian Bureau of Meteorology (BoM) and the Commonwealth Scientific and Industrial Research Organization (CSIRO). The ACCESS numerical weather prediction (NWP) system uses a four-dimensional variational data assimilation scheme (4DVAR) to provide a much improved use of observations. The system employs a diagnostic cloud scheme (Smith, 1990) which is based on conserved variables of liquid/frozen water temperature and total water content. The cloud amounts and water contents are derived using an assumed critical relative humidity and a sub-grid scale probability distribution of the conserved variables. Precipitation is simulated by a single-moment bulk microphysics scheme (Wilson and Ballard, 1999) with explicit calculation of transfers between vapour, liquid and ice phases.

The present study uses the operational ACCESS (United Model V7.6) system, which employs the BoM's operational configuration, Australian Parallel Suite version 1 (APS1, Figure 5.1 (d)). The ACCESS 'Victoria–Tasmania' (ACCESS-VT) domain is used, which covers the area of 33 – 46°S, 139 – 151°E and provides the resolution of 4 km grid-length horizontally and 70 levels vertically. The details of the domain settings and the physical parameterizations such as cloud, microphysics, convection, and boundary layer are described in Wilson and Ballard (1999) and Puri *et al.* (2013). The

present case study used the same time settings as H15 did as aforementioned: 1.67 min of the time step is used and the hourly outputs are retrieved from 36 h forecasts that are initialized at 1200 UTC.

### 5.2.3 Meteorology

The mean-sea-level pressure (MSLP) diagrams (Figure 5.2) at 0000 and 0600 UTC on the day show a cut-off low is present near 40°S, 158°E that is not budging during the 6 hours (0000 – 0600 UTC). Also, a strong high-pressure system is located south of Tasmania (50°S, 145°E) and expanding its area over this time. This synoptic pattern created a relatively uncommon southerly airflow across Tasmania. A pristine SO air mass was encountered (Figure 2.1 in section 2.1.1 Flight Overview) as the research aircraft flew over the ocean to the south of Tasmania, far from any frontal passage.

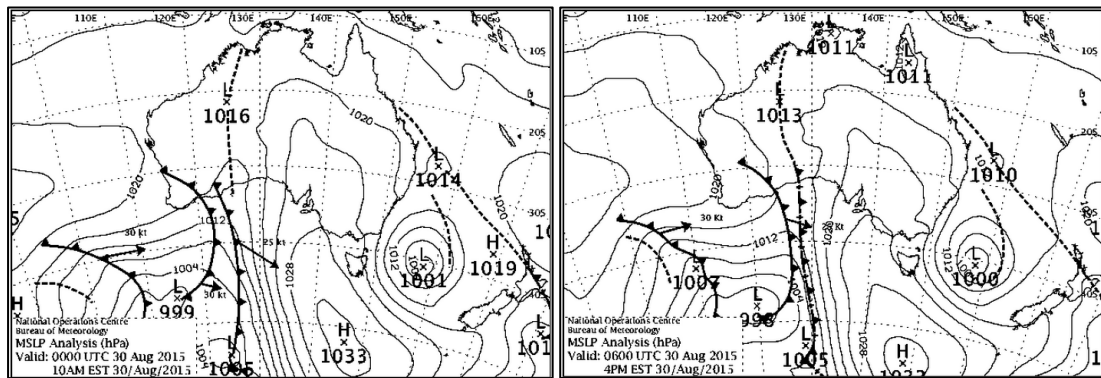


Figure 5.2. The mean-sea-level pressure (MSLP) diagrams for 0000 and 0600 UTC 30 August 2015.

The MODIS image in Figure 3.4 in section 3.3 shows open mesoscale cellular convection (MCC) is dominant to the south of Tasmania. The local meteorology for the case is detailed in the case study in section 3.3. The clouds were broken and patchy so

---

it was hard to define the cloud top and base precisely. According to the soundings at 0342 UTC (Table 3.2 and Figure 3.4), the heights of cloud top and base are 1.5 km and 0.7 km, respectively. The temperature of the cloud top and base is  $-2.6\text{ }^{\circ}\text{C}$  and  $0.1\text{ }^{\circ}\text{C}$  respectively. These clouds were consistently drizzling (91% of all cloud samples during the flight) as reported by the aircraft measurements.

### 5.3 Preliminary Results

The rain rates (RR) derived from the *in-situ* measurements of liquid clouds during the flight is shown in Figure 5.3 (a). This drizzle is mostly warm rain given that only 1.6 % (Table 2.1 in section 2.2 Meteorology) is mixed phase clouds. The coincided periods when the A-Train and the GPM overpassed are highlighted with light blue and pink shades, respectively, on the diagram. The intensity of drizzle varies from light to as heavy as  $6\text{ mmhr}^{-1}$ . The CIP images in Figure 5.3 (b) reveal the various size of drizzle and cloud droplets co-exist with a few ice crystals present.

The average RR that the aircraft observed during the A-Train overpass is  $0.98\text{ mmhr}^{-1}$  (30-minute window) and that from the GPM overpass is  $1.58\text{ mmhr}^{-1}$ . Note that the average *in-situ* RR can be biased by the flight path flown and may not represent a spatial average. The average *in-situ* RR during the whole flight is  $0.96\text{ mmhr}^{-1}$ . When the clouds are limited to very low-level near surface ( $> 900\text{ hPa}$ ), the average RR dropped to  $0.6\text{ mmhr}^{-1}$ .

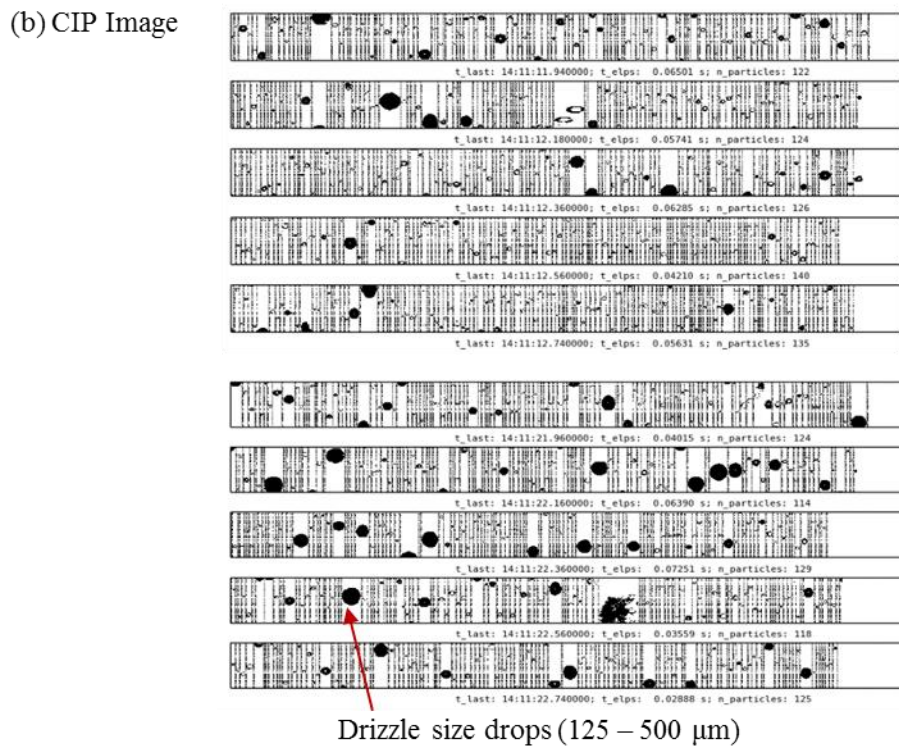
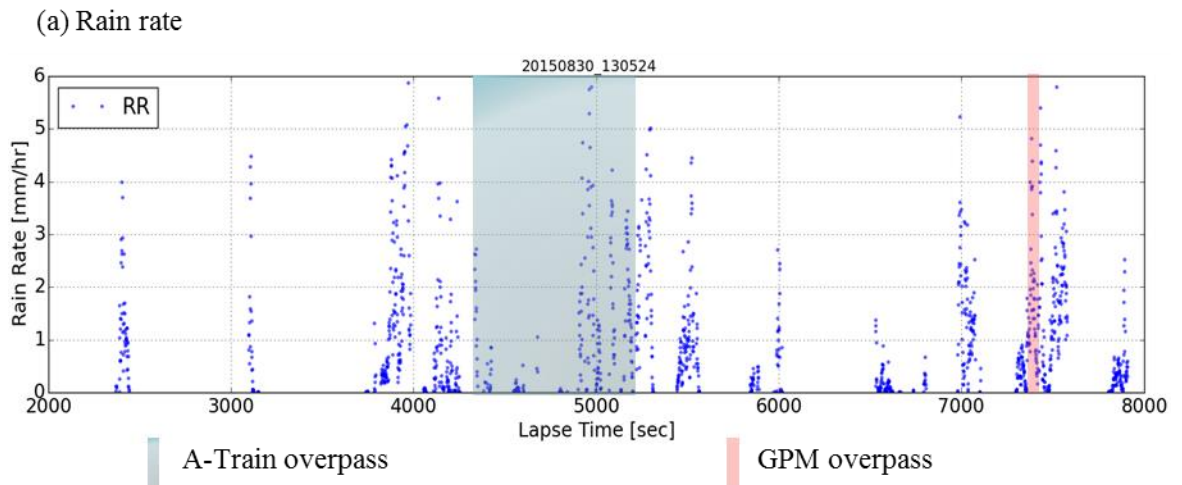


Figure 5.3. Time series of rain rate (RR,  $\text{mmhr}^{-1}$ ) and CIP image from aircraft observations during 30 August 2015 flight.

(a) The coincided period when the A-Train overpassed is highlighted with blue shade and the GPM, with pink shade. (b) The CIP images of drizzle and clouds droplets captured during the flight.

---

The cloud structure seen by CALIPSO and CloudSat is presented in Figure 5.4. The areas collocated with *in-situ* observations are highlighted with light blue shade. The targeted cloud field is liquid-dominant, and no overlying cirrus is found in the CALIOP and CloudSat CPR profiles (Figure 5.4 (a) and (b)). The thermodynamic phase retrievals from the MODIS infrared (IR) and cloud property optical phase (CPOP) products also show almost no sign of ice in either the single-layer or multi-layer clouds pixels (Table 4.2 and Figure A3). The CPR reveals shallow to mid-depth maritime cumulus below 1.2 km over the region of 43.8 – 44.5°S with the radar reflectivity between -20 and 0 dBZ (5.3 (b)).

The cloud top height (~1.2 km) and cloud base height (~0.4 km) from the lidar and radar profiles are in a reasonable agreement (200 - 300m differences) with the *in-situ* observations. However, the temperature from European Centre for Medium-range Weather Forecasts (ECMWF) overlaid on the profiles of Figure 5.4 (a) and (b) is 2 to 5 °C warmer than the *in-situ* measurements (Figure 4.3). It is noted that this bias of MODIS temperature in comparison with aircraft observations was also observed and was discussed in section 4.3 (Figure 4.3). Note that the cloud-top properties retrieved by MODIS are, in general, sensitive to the cloud-top temperatures, whereas the *in-situ* observations are commonly conducted below cloud-top.

The CloudSat profile (a single column) is generated over a 0.16 second interval, which corresponds to a 1.1 km along-track distance. With orbital motion, this produces a footprint of approximately 1.4 km (across-track) by 2.5 km (along-track). The rain rate is an average of the precipitation columns along the segments.

Only four precipitation (rain) columns ('certain' + 'probable') are identified with the CPR PC in the targeted area (Figure 5.4 (c)). This shows that the CPR PC detected the rain extremely infrequently compared to the aircraft measurements which showed 88% (not shown) of the time was drizzling.

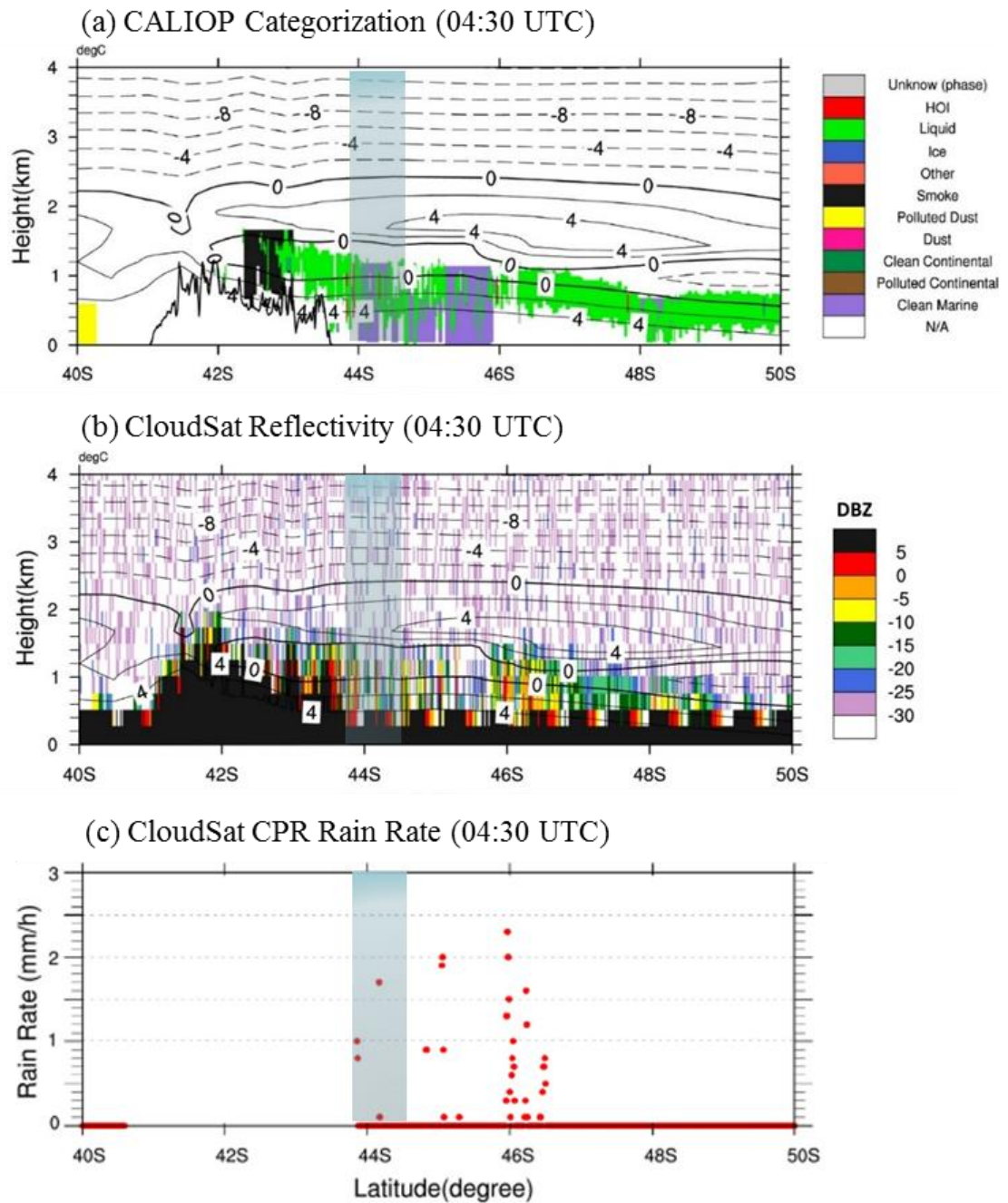


Figure 5.4. A-Train satellite observations at 04:30 UTC 30 August 2015. (a) CALIOP categorization. (b) CloudSat CPR reflectivities.

The temperatures from European Centre for Medium-range Weather Forecasts (ECMWF) are overlaid on (a) and (b). (c) Rain rate retrieved from the CloudSat CPR ‘2C-PRECIP-COLUMN’ (PC) product.

---

It is remarkable that the average rain rate for those four columns (0.93 mmhr<sup>-1</sup>) is very close to the aircraft measurements (0.98 mmhr<sup>-1</sup>).

Aforementioned, no level 2 data from the Ka and Ku band radars were available for this day: only the level 3 GMI IMERG product retrievals were available. IMERG provides rainfall estimates by combining the data from all constellation microwave (MW) sensors (Hou *et al.*, 2014). The intention of this algorithm is to calibrate, merge, and interpolate all satellite microwave precipitation estimates, including microwave-calibrated infrared satellite estimates, precipitation gauge analyses, and potentially other precipitation estimators. Figure 5.5 shows the final run of the 10 km × 10 km rainfall estimate (GPM 3IMERGHH v04 product) for 30 min (0500 - 0529 UTC). No surface precipitation is registered over the ocean around Tasmania except for a few grids to the east of Tasmania with the low RR of 0.2 – 0.45 mmhr<sup>-1</sup>.

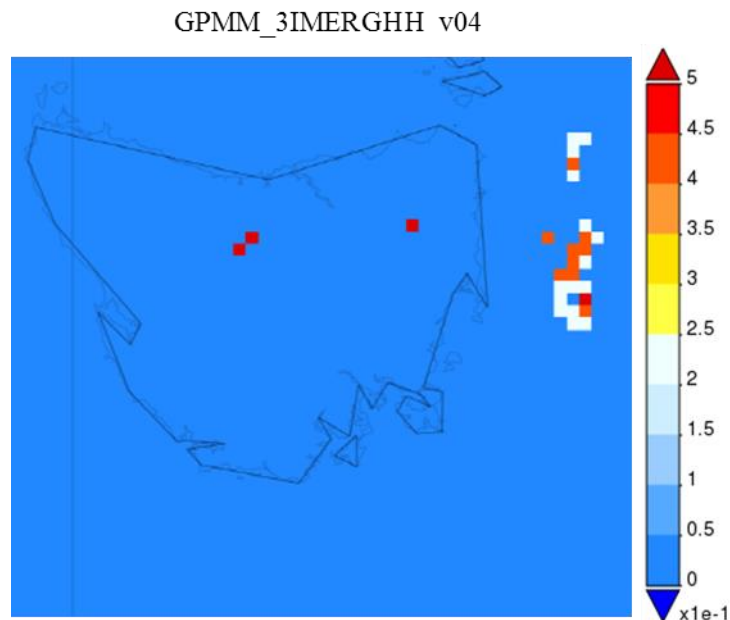


Figure 5.5. Time averaged map of GPM multi-satellite precipitation estimate [mmhr<sup>-1</sup>] over 0500 – 0529 UTC, 2015-08-30.

---

Another run with GPM over 0430 - 0529 UTC, effectively extending the time window, also registered no rainfall in the targeted region (Figure 5.6). This demonstrates the GMI IMERG algorithm which takes account of all passive microwave sensors did not capture any precipitation when the aircraft observed consistent and rather heavy drizzle ( $1.58 \text{ mmhr}^{-1}$  on average) over the ocean to the south of Tasmania.

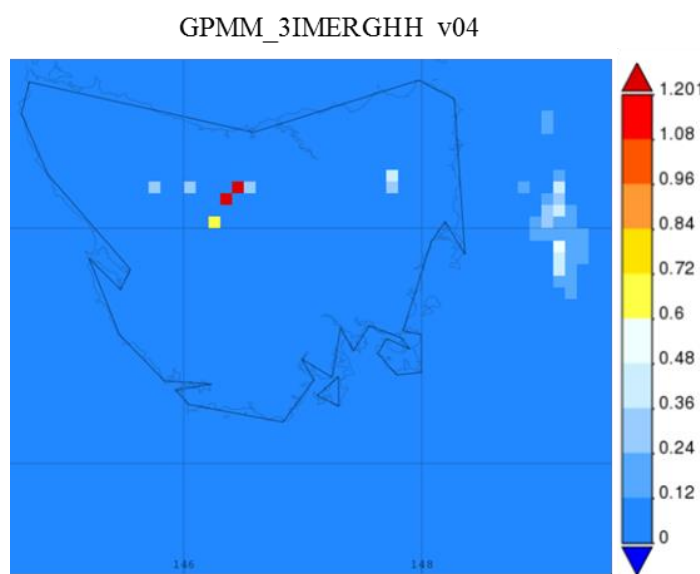


Figure 5.6. Time Averaged map of GPM multi-satellite precipitation estimate [ $\text{mmhr}^{-1}$ ] over 0430 – 0529 UTC, 2015-08-30.

Although an evaluation of the ACCESS precipitation product is not a part of the aims of the dissertation, it is of immediate interest to appreciate how well drizzle is simulated over the SO. The surface precipitation simulated by ACCESS at 0405 UTC is shown in Figure 5.7. The simulated precipitation ( $0.01 - 0.04 \text{ mmhr}^{-1}$ ) largely underestimates the *in-situ* and CloudSat rain rates. The ACCESS precipitation is variable across the ocean of Tasmania. The broad area average increased to  $0.10 \text{ mmhr}^{-1}$  but it is still less than the *in-situ* observations.

---

These results are the opposite of the similar analysis made in H15 (CASE A). During the flight in H15, very little drizzle was observed *in-situ*, but a fair amount of drizzle ( $0.178 \text{ mmhr}^{-1}$ ) was simulated by ACCESS, which suggested that the model drizzle production was too efficient. Note that the simulated precipitation was sensitive to a variety of settings, including the cloud condensation nuclei (CCN) concentrations. The study of the variability in the simulated precipitation would be of interest to further investigate.

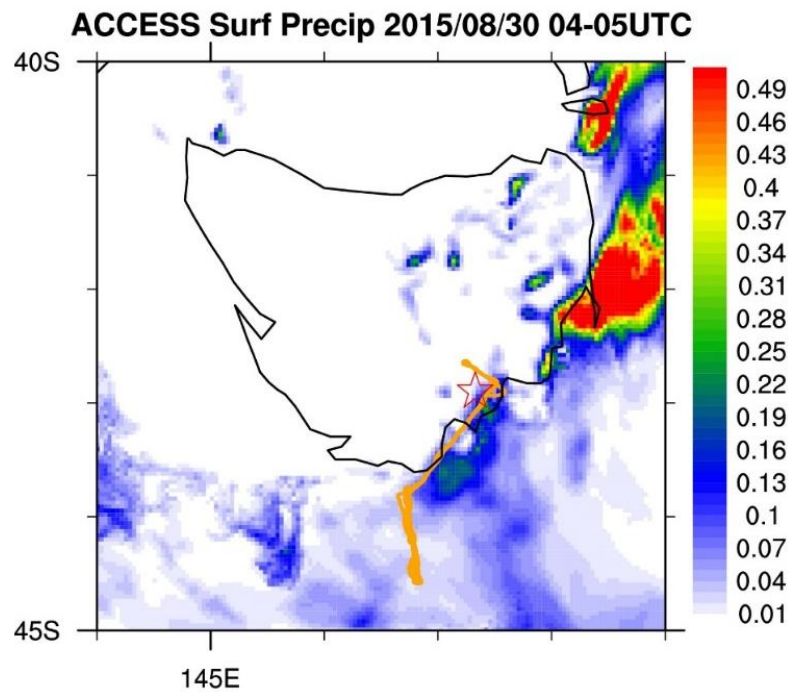


Figure 5.7. ACCESS simulated surface precipitation at 0405 UTC 30 August 2015 with aircraft tract overlaid.

## 5.4 Preliminary Conclusions

One preliminary case study (30 August 2015) was designed to evaluate satellite products with *in-situ* observations conducted to the south of Tasmania in a pristine air

---

mass. A-Train and GPM constellations overpasses were within a 30-minute window during the mission.

The clouds during the survey were predominantly patchy and drizzling where open MCC was commonly observed. CALIPSO, MODIS, and CloudSat, all showed the clouds were mostly liquid with no overlying cirrus. All remote sensors agreed well with the *in-situ* measurements for the cloud base and cloud top heights. But the cloud-top temperature retrieved by the MODIS were 2 - 5°C higher than that from the *in-situ* measurements.

The aircraft observed drizzle for 91% of all cloud samples during the whole flight with the average rain rate of 0.96 mmhr<sup>-1</sup>. When compared with the *in-situ* observations, the CloudSat CPR PC showed a high skill in estimating the precipitation intensity, but it highly underestimated the drizzle frequency even though the calculations include the rain columns of 'probable'. It is noted there are limitations in comparing the *in-situ* RR calculations with those from CloudSat as it is uncertain whether the drizzle observed *in-situ* in clouds reached to the surface and is accounted for the surface precipitation of CloudSat.

Due to the unavailability of GPM DPR, only GMI IMERG products were used to evaluate the GPM sensors. The final runs of the IMERG products during both 30 minutes and 1.5 hours were not able to capture any precipitation over the region where the aircraft observed consistent drizzle with the rain rate of 1.58 mmhr<sup>-1</sup>. This is a good example to demonstrate that the most advanced passive microwave sensors and algorithm still have a limitation to detect light precipitation in open MCC over the SO. The ACCESS model is able to simulate this drizzle to an extent, but its intensity was much too low, even across a wide area.

Considering the frequency and intensity of the *in-situ* drizzle was underestimated due

---

to its instrumental limitation (1550  $\mu\text{m}$  threshold for liquid water droplet size), the bias from the A-Train and GPM observations and the ACCESS simulation may be greater.

# Chapter 6

## Conclusions

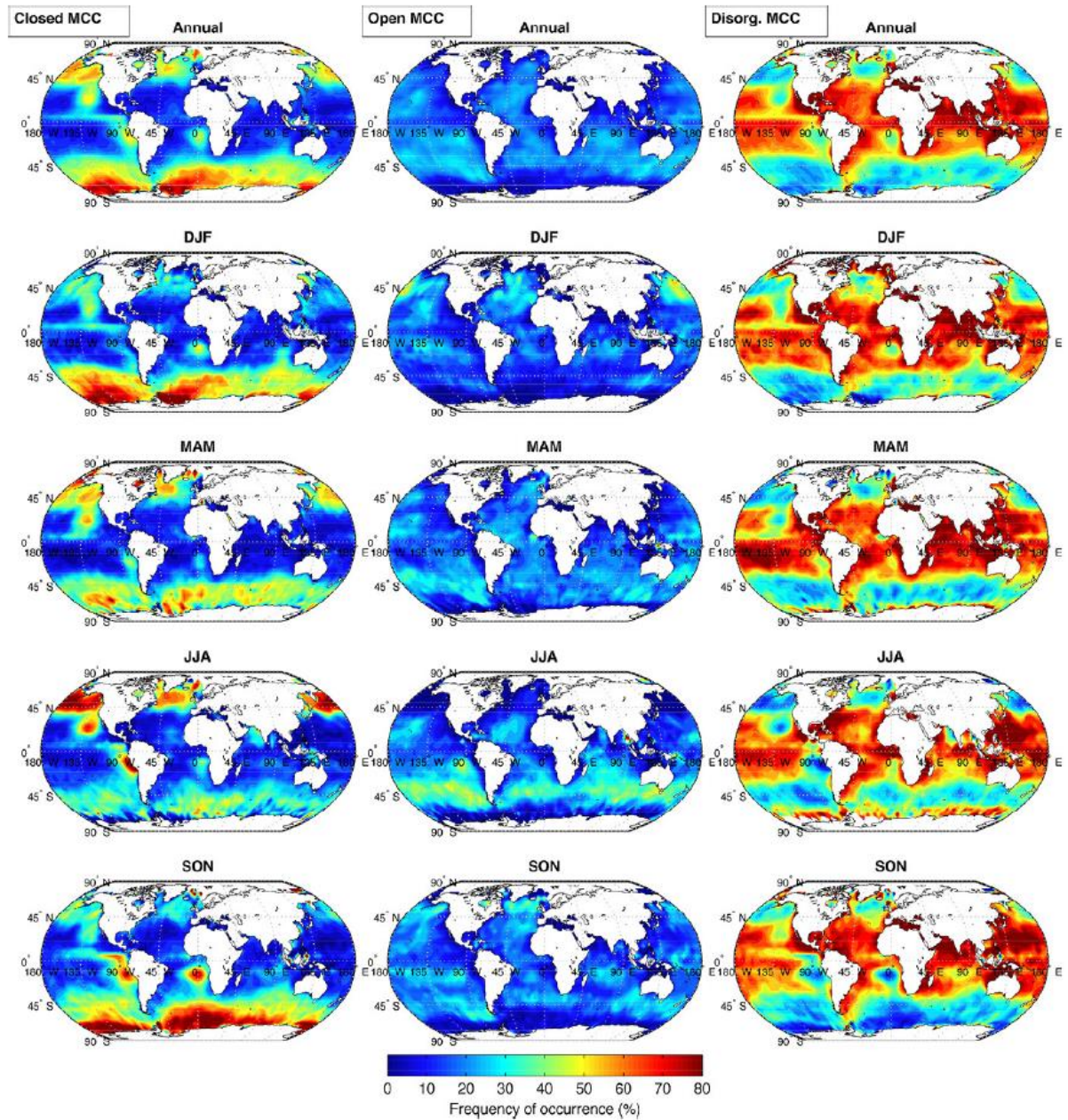


Figure 6.0 Global distribution of the frequency of occurrence of Mesoscale Cellular Convection (MCC) types over the ocean based on 1 year of MODIS Aqua observations from 2008.

Shown are closed MCC (left), open MCC (center) and cellular but disorganized MCC (right). The frequency of open MCC in Austral winter time is markedly higher compared to summer season over the Southern Ocean (adapted from Muhlbauer et al., 2014.)

---

## 6.1 Summary and Discussions

The central theme of this research has been to develop representative microphysical and thermodynamic properties of wintertime (Jun – Oct, 2013 - 2015), low-altitude clouds over the Southern Ocean (43–45°S, 145–148°E) based on new aircraft observations. It has greatly expanded the findings of the SOCEX I (Boers *et al.*, 1996) study on wintertime cloud microphysical properties by studying a greater variety of synoptic meteorology. The subsidiary theme has been to establish the sensitivity of the microphysical properties ( $N_d$ ,  $r_{eff}$  and LWC) and the thermodynamic phase to the synoptic and local meteorology including drizzle. To address the main and subsidiary themes, *in-situ* observations of clouds thermodynamic and microphysical properties were analysed in chapters 2. In chapter 3, the microphysical properties of these clouds were further explored of their sensitivity to drizzle and the differences between drizzling clouds and non-drizzling clouds were intensely examined through case studies. This research then goes on to evaluate A-Train satellite retrievals of the cloud microphysics against the *in-situ* observations. Such an evaluation is crucial over the SO given the lack of observations and the unique nature of SO clouds. Chapter 4 compares microphysical properties between *in-situ* and MODIS observations for liquid cloud samples and drizzle over the Southern Ocean. Although it is preliminary, a case study for drizzle with *in-situ*, GPM, A-Train, and ACCESS observations is included in chapter 6.

Of the total 20,357 one-second records spent in cloud in our twenty flights, 38.5% were found to contain ice crystals, primarily in mixed-phase clouds (36.7%) rather than glaciated clouds (1.8%). All samples were taken at temperatures warmer than -15 °C. The percentage of mixed-phase samples is very high in comparison to Morrison *et al.* (2011) who found only ~5% mixed phase occurrence, using MODIS, in the -15 – 5 °C range over the winter time SO. Fourteen of the 20 flights had ice (either mixed phase

---

or glaciated) present for at least 10% of all cloud samples. The droplet spectra and temperature range suggest these clouds were ideal for the Hallett-Mossop ice multiplication process. The frequency of mixed phase cloud samples is vastly higher than those found in the similar temperature range in the neighbourhood of Canada as detailed in Korolev *et al.* (2003).

The  $N_d$  from our observations of liquid clouds are primarily in the range 7 - 40  $\text{cm}^{-3}$ , which is consistent with that of SOCEX I ( $10 < N_d < 40 \text{ cm}^{-3}$ ), albeit our research explored a greater variety of synoptic meteorology. Such pristine conditions are unique in comparison with those of the North Pacific, North Atlantic or Arctic, where the average  $N_d$  has been observed to be 2 - 4 times higher. The  $r_{eff}$  of the SO clouds was in the range of 10.8 to 14.7  $\mu\text{m}$ , which is bigger than that from the Northern Hemisphere.

The synoptic and local meteorology were analysed for all 20 flights, but no outstanding relationship was found between the meteorology and  $N_d$ , except  $N_d$  tends to be higher in post frontal conditions than prefrontal conditions. Unlike in SOCEX I, there were two distinct observations of non-drizzling clouds with relatively high  $N_d$  ( $\sim 89 \text{ cm}^{-3}$ ) and small  $r_{eff}$  ( $\sim 8.5 \mu\text{m}$ ). One flight (20151001) encountered post frontal conditions, but the other (20130723) was far from any frontal systems and was on the ridge that was dominant over the ocean to the west and south of Tasmania (Figure A8).

Similar to SOCEX I, drizzle was frequently observed throughout this campaign. 49% of all liquid cloud samples were observed to be precipitating with an average overall  $0.733 \text{ mm h}^{-1}$  rain rate. Drizzling periods longer than 10s were rarely found as drizzle samples were commonly in the neighbourhood of mixed phase or non-drizzling cloud samples. The drizzling samples were, on average, found to have lower  $N_d$  and greater  $r_{eff}$  than that of the overall average. When the two anomalous high  $N_d$  flights were removed, the non-drizzling samples have largely similar  $N_d$  values as the drizzling liquid cloud samples.

---

The two, unique high  $N_d$  cases were thoroughly examined and compared to two drizzling cases in a case study. This effort failed to identify any particular forcing that may have led to the high  $N_d$ , although the analysis was limited by the aircraft instrumentation. It is plausible that a different source of cloud condensation and/or ice nuclei could have contributed to such differences, although this is strictly speculative. The cloud morphology is hypothesized to have a link to the high  $N_d$  observations as those two flights featured closed MCC, while the remaining 18 cases consisted of open, disorganized or no-MCC. The study of Muhlbauer *et al.* (2014) shows the open MCC is more common in winter over the SO, and closed MCC, in summer. The variance and standard deviation of  $N_d$  in SOCEX I and our research are about 119 and 11, and 452 and 21, respectively. The study highlights that greater variability of  $N_d$  exists in wintertime clouds over the SO when a wider range of synoptic meteorology is explored.

When we refer back to the conceptual diagram (Figure 1.2) detailing the internal feedbacks that influence the macrophysical and microphysical properties of a cloud, it is found that the two high  $N_d$  cases (and the rest of 18 cases) follow the relationship between  $N_d$  and precipitation. However, when the analysis is extended to SOCEX I and II (winter and summer time, respectively) and the parameters are quantitatively compared, it is no longer that simple. In the range of  $N_d$  (~90 - 100), the summer time clouds experienced drizzle in SOCEX II, but the winter time clouds we observed did not. Besides factors such as  $h$ ,  $LWP$  or/and  $f_c$ , it is evident from the droplet size distributions (Figure 3.3(b)) that these clouds are not efficient to collide to develop precipitation. These droplet size distributions suggest that the differences in the existence of drizzle need to be further explored.

The unique characteristics of our clouds are also substantiated by the MODIS retrievals. Eleven of the twenty flights were designed to coincide with an A-Train overpass. *In-situ* observations of cloud-top thermodynamic phase,  $r_{eff}$ , and  $N_d$  are compared to

---

derived products from MODIS and CALIOP observations. Compared to global marine clouds (Cho et al., 2015), our winter time clouds had relatively more MODIS partially cloud (PCL) pixels and a higher  $r_{eff}$  retrieval failure rate, as we investigated in chapter 4.

The cloud thermodynamic phase was firstly examined with CALIOP. Four of the eleven flights were largely ‘iced’ having ice and mixed phase cloud samples in excess of 24% of all samples. CALIOP recorded no ice for two of the four flights. Cloud phase discrimination by MODIS has been made with both the tri-spectral IR product and the CPOP product. The MODIS phase products were not particularly sensitive to whether a single-layer or all (single-layer + multi-layer) cloud samples were analysed. Although the MODIS IR phase product qualitatively agree with the *in-situ* observations, it overestimated the *in-situ* ice frequency by a factor of 2 – 8 times. On the other hand, the CPOP product underestimated the *in-situ* ice phase frequency by a factor of 4.3 – 8 times for three iced flights. The C6 MODIS IR and CPOP products showed an ‘internal’ qualitative consistency within the IR and CPOP data. That is, the ice fraction of the IR or CPOP for the iced flights is higher than that from the other flights.

We have taken extreme caution to evaluate the cloud phase discrimination from the remote sensors with the *in-situ* observations. It is not only challenging to temporally and spatially align the observations, but also to consider the different definitions/algorithms of cloud thermodynamic phase. The CALIOP, MODIS C6 IR and CPOP products for mixed phase cloud samples was particularly poor. To identify mixed-phase cloud samples (e.g. a thin layer of supercooled water on top of cold ice clouds), CALIOP requires a discontinuity in the vertical profile of depolarization (Liu *et al.*, 2005) of at least 30%. The current version of CALIOP cloud phase does not yet provide a ‘mixed phase’ classification, although the relationship between ‘integrated depolarization’ and ‘layer integrated backscatter’ for the ‘mixed phase’ is ready. The test of the ice-water algorithm (IWA) in Liu *et al.* (2005) shows some depolarization-

---

backscatter values for mixed phase cloud are mapped to ‘liquid’ phase. The author suspects that this mapping can contribute to CALIOP commonly identifying ‘liquid’ cloud samples for mixed phase and glaciated cloud samples.

The MODIS C6 IR cloud phase category also does not have a ‘mixed phase’ class, because its algorithm was found to ambiguously identify the presence of supercooled water or mixed-phase clouds in comparison with CALIOP cloud phase. In addition, in the comparison of IR phase discrimination between C5 and C6, many of the ‘uncertain’ granules, which include ‘mixed phase’ in C5, are identified as ‘ice’ in C6 (Baum *et al.*, 2012). From these factors, we infer that mixed phase clouds can be identified as either ice or unknown/not determined (UK/ND) granules.

In addition to the mixed phase issue, the CALIOP showed other limits as well. Under overlaying thick (~1km) liquid clouds, it could not capture any cloud, and under overlaying cirrus it displayed difficulty in identifying ice/liquid. The advanced MODIS IR and CPOP products did not show good results, either, in these conditions. The present thesis illustrates that discriminating cloud phase over the SO is highly challenging for both passive and active remote sensors due to very complex conditions: the clouds are commonly patchy, mixed phase and having large size droplets.

With liquid phase clouds, the *in-situ* observations were employed to evaluate  $r_{eff}$  and  $N_d$ , retrieved and derived from the 1.6, 2.1 and 3.7  $\mu\text{m}$  channels on MODIS. The 11 flights are separated as five drizzling (two heavily) and six non-drizzling flights. For non-drizzling cases, the *in-situ*  $r_{eff}$  is overestimated by 4 – 13  $\mu\text{m}$ . These results for non-drizzling clouds were consistent to those from the VOCALS-REX in that the *in-situ* average  $r_{eff}$  was in better agreement with that of the 3.7  $\mu\text{m}$  channel than 2.1. However, the magnitude of the overestimation is much (67%) higher than that from the VOCALS-REX. The high solar zenith angles ( $> 65^\circ$ ) of many observations was considered, but

---

could not explain the large overestimation.

For the three lightly drizzling clouds, the MODIS  $r_{eff}$  agrees well with the *in-situ* observations with high correlation coefficients (Chapter 4.5). In case of the two heavily drizzling flights, the MODIS  $r_{eff}$  underestimates the *in-situ* observations by 4.8 – 12.4  $\mu\text{m}$ , mainly due to the threshold limit (30  $\mu\text{m}$ ) for liquid clouds in the MODIS lookup table. The MODIS derived cloud droplet number concentration,  $N_d$ , is largely consistent with the *in-situ* observations in spite of the limitation in  $r_{eff}$  as the high correlation coefficients showed. The two closed MCC flights had the largest retrieved values of  $N_d$ , but still underestimated the *in-situ* calculations mainly due to the overestimation of  $r_{eff}$ .

As described earlier, the overestimation of MODIS  $r_{eff}$  for non-drizzling clouds is much higher over the SO compared to that of stratiform clouds over the Southeast Pacific. This is understandable as the systematic overestimation increases with increasing  $r_{eff}$  (Painemal and Zuidema, 2011). In addition to the systematic overestimation, further bias may be due to ice contamination (e.g. Zheng *et al.*, 2011). Cloud variability/inhomogeneity are assumed to contribute the errors for the  $r_{eff}$  retrievals, which should be explored further in the future. The MODIS overestimation was less in the lightly drizzling cases, while the MODIS  $r_{eff}$  underestimated the *in-situ* observations for heavily drizzling cases. This inconsistent behaviour of satellite observations is problematic over the Southern Ocean where drizzling and mixed phase clouds are frequent during wintertime.

The preliminary result with CloudSat and GPM constellation showed drizzle over the SO can be missed or underestimated even by the most sensitive remote sensors. As discussed, however, the results of the case study in chapter 5 was preliminary due to the unavailability of core Ku/Ka bands dataset.

---

## 6.2 Future Directions

Out of many questions arising from this research, there are several due to the limitations of the *in-situ* observations. The present research is limited to winter time observations with no opportunity to extend the analysis to the summer time, because the research flights were conducted in cooperation with Hydro Tasmania, which employed the aircraft only for the winter months. Summer time *in-situ* observations would provide valuable climatological information of these SO clouds, such as the seasonality of  $N_d$  and  $r_{eff}$  (Boers *et al.*, 1996; 1998). Only two out of the 20 flights were identified as having closed MCC, and they had high  $N_d$ . As closed MCC is more common in summer than winter over the SO (Muhlbauer *et al.*, 2014), the summer time observations would provide more enriched microphysical information about closed MCC. This complete set of observations of winter and summer may also provide a stronger link between  $N_d$  and MCC type.

Microphysical properties of drizzling cloud and non-drizzling clouds have been analysed and compared with each other using *in-situ* observations in chapter 4. This analysis was largely limited to the warm-cloud samples. Further analysis of the microphysics of the mixed-phase samples still remains. In chapter 5, the analysis of mixed-phase cloud samples by MODIS was studied in terms of the cloud pixel population by channel and cloud regime (overcast and PCL), as well as  $r_{eff}$  and retrieval failure rates. Having summer time observations would be of great interest and allow for a comparison of the properties of drizzling/non-drizzling clouds of different seasons/MCC types.

The synoptic and/or local forces that drove the two closed MCC (high  $N_d$  concentration) cases have not been fully explained in this study and warrant further investigation. The HYSPLIT back trajectories suggest that the air mass was pristine, and not immediately different than the other cases studied. It would have been of interest to have *in-situ*

---

aerosol concentrations, but this is beyond the capabilities of the aircraft. More reliable wind (speed and direction) measurements also would have been necessary for a more robust analysis, as strong gusts can be another factor to affect the cloud  $N_d$  over the SO (Chubb *et al.*, 2016).

A deeper appreciation of this research leads to several suggestions with respect to evaluating satellite retrievals over the Southern Ocean. First and foremost, given the patchy nature of clouds over the SO, it is essential to have a large set of in-situ observations dedicated to that purpose. High quality wind (speed and direction) observations should allow for the inter comparison time period to be expanded from 30 minutes to 60 minutes. If a 60 min (~120km) time period is chosen, then three 20-minute, along-track flight legs would be ideal. The flight path should be timed such that the satellite overpass coincides with the midpoint of the second leg. The satellite (e.g. MODIS) pixels should be selected to account for the advection of the cloud field. These horizontal legs should be flown as a ‘sawtooth’ across cloud-top with the altitude adjusting to any changes in the cloud-top altitude. We still recommend that two ‘full depth’ profiles (150 – 7000 m altitude) be made at the beginning and end of the horizontal sampling.

Mixed phase clouds are known to still be a challenge for state-of-art remote sensors and the results in chapter 4 highlighted it. This study showed that ice was underestimated by the MODIS CPOP product for three of four heavily glaciated flights (ice frequency of 12% – 56% of the cloud samples with  $\mu_3 > 0.5$ ), and CALIOP did not even capture any ice for two of these four cases. However, we cannot exclude the possibility that part of this difference in ice identification is due to differences in defining the mixed/ice phase cloud samples between the three algorithms. It was common to identify mixed phase cloud samples, as judged by the in-situ observations, labelled as either ‘ice’, ‘UK/ND’ or even ‘liquid’ phase by CALIOP and MODIS. Further, differences in the definition of ‘glaciated cloud’ have not been fully resolved between in-situ and satellite

---

observations. In-situ observations define ‘ice/mixed’ phase cloud by a ratio of ice and liquid water content, while CALIOP and MODIS employ the depolarization ratio and the spectral difference (as well as cloud temperature), respectively. There needs to be a measure to directly compare the cloud phase between in-situ and satellite observations. This would then allow for a means to convert the range/value of  $\mu_3$  employed in the in-situ observations to the ‘ice’ phase employed by CALIOP and MODIS.

A preliminary test was made to establish a relationship between the cloud mask sub-pixel heterogeneity index (CM\_SPI, indicated in Table 4.1), the cloud type (open/closed MCC) and drizzle. The initial results were not conclusive: no such relationship could be established with confidence. The cloud layer science dataset, cloud multi-layer flag (CMLF) needs to be further investigated. The cloud thermodynamic phase was not observed to be highly sensitive to the cloud layers parameter (single-layer or multi-layer) as discussed. A sensitivity study of the microphysical properties to the cloud layers parameter, combined with cloud sub-pixel heterogeneity could, however, provide new insight.

Lastly, extending the satellite evaluation work to the CloudSat products (precipitation strength and frequency) for the 11 research flights would be of interest. This analysis could then be extended further to MODIS precipitation algorithms.

---

## Reference

- Albrecht B. A. 1993. The effects of drizzle on the thermodynamic structure of the trade-wind boundary layer, *J. Geophys. Res.*, **98**, 327–7337.
- Austin P., Wang Y., Pincus, R., and Kujala, V. 1995. Precipitation in stratocumulus clouds: observations and modeling results, *J. Atmos. Sci.*, **52**, 2329–2352.
- Ayers GP and Cainey JM. 2007. The CLAW hypothesis: A review of the major developments. *Environ. Chem.* **4**: 366–374, doi: 10.1071/EN07080.
- Barker HW, Korolev AV, Hudak DR, Strapp JW, Strawbridge KB, Wolde M. 2008. A comparison between CloudSat and aircraft data for a multilayer, mixed phase cloud system during the Canadian CloudSat-CALIPSO Validation Project. *J. Geophys. Res.* **113**: D00A16, doi: 10.1029/2008JD009971.
- Barker HW and Liu D. 1995. Inferring optical depth of broken clouds from Landsat data. *J. Climate*, **8**, 2620–2630.
- Bates T. S., B. J. Huebert, J. L. Gras et al. 1998. International Global Atmospheric Chemistry (IGAC) Project's First Aerosol Characterization Experiment (ACE 1): Overview, *J. Geophys. Res.*, **103** (D13), 16297-16318.
- Baum B. A., P. F. Soulen, K. I. Strabala, M. D. King, S. A. Ackerman, W. P. Menzel, and Yang P. 2000. Remote sensing of cloud properties using MODIS Airborne Simulator imagery during SUCCESS: 2. Cloud thermodynamic phase, *J. Geophys. Res.*, **105**, 11,781–11,792.
- Baum B. A., W. P. Menzel, R. A. Frey, D. C. Tobin, R. E. Holz, S. A. Ackerman, A. K. Heidinger, and Yang P. 2012. MODIS cloud-top property refinements for Collection 6. *J. Appl. Meteor. Climatol.*, **51**, 1145–1163, doi:10.1175/JAMC-D-11-0203.1.
- Baumgardner D, S. Abel, D. Axisa, R. Cotton, J. Crosier, P. Field, C. Gurganus, A. Heymsfield, A. Korolev, M. Krämer, P. Lawson, G. McFarquhar, J. Z Ulanowski, J. Shik Um, 2016: Chapter **9**: Cloud Ice Properties - In Situ Measurement Challenges,

---

*American Meteorological Society Meteorological Monographs on Ice Formation and Evolution in Clouds and Precipitation: Measurement and Modeling Challenges*, Eds. D. Baumgardner, G. McFarquhar, A. Heymsfield, Boston, MA.

Baumgardner D, Jonsson H, Dawson W. 2001. The cloud aerosol and precipitation spectrometer: A new instrument for cloud investigators. *Atmos. Res.* **59–60**: 251–264, doi: 10.1016/S0169-8095(01)00119-3.

Behrangi, A., M. Lebsock, S. Wong, and B. Lambrigtsen, 2012: On the quantification of oceanic rainfall using spaceborne sensors. *J. Geophys. Res.*, **117**, D20105.

Behrangi, A., G. Stephens, R. Adler, G. Huffman, B. Lambrigtsen, and M. Lebsock, 2014: An update on oceanic precipitation rate and its zonal distribution in light of advanced observations from space. *J. Climate.*, **27**, 3957-65. doi:10.1175/JCLI-D-13-00679.1.

Bennartz R. 2007. Global assessment of marine boundary layer cloud droplet number concentration from satellite. *J. Geophys. Res.* **112**: D02201, doi: 10.1029/2006JD007547.

Berg W, L'Ecuyer T, Haynes JM. 2010. The distribution of rainfall over oceans from spaceborne radars. *J. Appl. Meteorol. Climatol.* **49**: 535–543, doi: 10.1175/2009JAMC2330.1.

Biter CJ, Dye JE, Huffman D, King WD. 1987. The droplet response of the CSIRO liquid water probe. *J. Atmos. Oceanic Technol.* **4**: 359–367. doi: [http://dx.doi.org/10.1175/1520-0426\(1987\)004<0359:TDSROT>2.0.CO;2](http://dx.doi.org/10.1175/1520-0426(1987)004<0359:TDSROT>2.0.CO;2).

Bodas-Salcedo, P. G. Hill, K. Furtado, K. D. Williams, P. R. Field, J. C. Manners, P. Hyder, and S. Kato, 2016: Large contribution of supercooled liquid clouds to the solar radiation budget of the Southern Ocean. *J. Climate*, **29**, 4213–4228, doi:10.1175/JCLI-D-15-0564.1.

Boers R, Acarreta, J. R., and Gras, J. L. 2006. Satellite monitoring of the first indirect aerosol effect: retrieval of the droplet concentration of water clouds, *J. Geophys. Res.-Atmos.*, **111**, D22208 doi:10.1029/2005jd006838.

---

Boers R, Jensen JB, Krummel PB. 1998. Microphysical and radiative structure of marine stratocumulus clouds over the Southern Ocean: Summer results and seasonal differences. *Q. J. R. Meteorol. Soc.* **124**: 151–168, doi: 10.1002/qj.49712454507.

Boers R, Jensen JB, Krummel PB, Gerber H. 1996. Microphysical and short-wave radiative structure of wintertime stratocumulus clouds over the Southern Ocean. *Q. J. R. Meteorol. Soc.* **122**: 1307–1339, doi: 10.1002/qj.49712253405.

Boutle IA, Abel SJ, Hill PG, Morcrette CJ. 2014. Spatial variability of liquid cloud and rain: Observations and microphysical effects. *Q. J. R. Meteorol. Soc.* **140**: 583–594, doi: 10.1002/qj.2140.

Breon F. M. and Colzy S. 2000. Global distribution of cloud droplet effective radius from POLDER polarization measurements. *Geophys. Res. Lett.*, **v27**, i24, 4065–4068, DOI: 10.1029/2000GL011691.

Breon F. M. and Doutriaux-Boucher M., 2005. "A comparison of cloud droplet radii measured from space," in *IEEE Transactions on Geoscience and Remote Sensing*, vol. **43**, no. 8, pp. 1796-1805, Aug. doi: 10.1109/TGRS.2005.852838.

Breon F.M., and Ph. Goloub. 1998. Cloud droplet effective radius from spaceborne polarization measurements. *Geophys. Res. Lett.*, **25**, 1879-1882.

Bretherton C. S., and Hartmann D. L. 2009. Large-scale controls on cloudiness. *Clouds in the Perturbed Climate System: Their Relationship to Energy Balance, Atmospheric Dynamics, and Precipitation*, J. Heintzenberg and R. Charlson, Eds., *MIT Press*, 217–234.

Burrows SM, Hoose C, Pöschl U, Lawrence MG. 2013. Ice nuclei in marine air: Biogenic particles or dust? *Atmos. Chem. Phys.* **13**: 245–267, doi: 10.5194/acp-13-245-2013.

Caldeira, K., and P. B. Duffy (2000), The role of the Southern Ocean in uptake and storage of anthropogenic carbon dioxide, *Science*, **287**, 620–622.

Chan M. A., and Comiso J. C. 2011. Cloud features detected by MODIS but not by

---

CloudSat and CALIOP, *Geophys. Res. Lett.*, **38**, L24813, doi:10.1029/2011GL050063.

Chang, F. L. and Li, Z. Q. 2001. The Effect of Droplet Size Distribution on the Determination of Cloud Droplet Effective Radius, *Eleventh ARM Science Team Meeting Proceedings*, Atlanta, Georgia, 19–23.

Chang F.-L. and Li Z. 2002. Estimating the vertical variation of cloud droplet effective radius using multispectral nearinfrared satellite measurements. *J. Geophys. Res.*, **107**, 4257, doi:10.1029/2001JD000766.

Charlson RJ, Lovelock JE, Andreae MO, Warren SG. 1987. Oceanic phytoplankton, atmospheric sulphur, cloud albedo and climate. *Nature* **326**: 655–661, doi: 10.1038/326655a0.

Chen T., W. B. Rossow, and Y. C. Zhang. 2000. Radiative effects of cloud-type variations, *J. Clim.*, **13**, 264–286.

Cho H.-M., and Coauthors. 2015. Frequency and causes of failed MODIS cloud property retrievals for liquid phase clouds over global oceans. *J. Geophys. Res. Atmos.*, **120**, 4132–4154, doi:10.1002/2015JD023161.

Christensen MW, Stephens GL, Lebsock MD. 2013. Exposing biases in retrieved low cloud properties from CloudSat: A guide for evaluating observations and climate data. *J. Geophys. Res. Atmos.* **118**: 12120–12131, doi: 10.1002/2013JD020224.

Chubb TH, Siems ST, Manton MJ. 2011. On the decline of wintertime precipitation in the Snowy Mountains of southeastern Australia. *J. Hydrometeorol.* **12**: 1483–1497, doi: 10.1175/JHM-D-10-05021.1.

Chubb TH, Jensen JB, Siems ST, Manton MJ. 2013. In situ observations of supercooled liquid clouds over the Southern Ocean during the HIAPER Pole-to-Pole Observation campaigns. *Geophys. Res. Lett.* **40**: 5280–5285, doi: 10.1002/grl.50986.

Chubb TH, Huang Y, Jensen JB, Campos T, Siems ST, Manton MJ. 2016. Observations of high droplet number concentrations in Southern Ocean boundary layer clouds. *Atmos. Chem. Phys.* **16**: 971–987, doi: 10.5194/acp-16-971-2016.

---

Coakley J. A., Friedman M. A., Tahnk W. R. 2005. Retrieval of cloud properties for partly cloudy imager pixels, *J. Atmos. Oceanic Technol.*, **22**, 3–17. <https://doi.org/10.1175/JTECH-1681.1>.

Cober SG, Isaac GA, Korolev AV. 2000. ‘Assessing the relative contribution of liquid and ice phases in winter clouds’. In *Proceedings of 13th International Conference on Clouds and Precipitation*, **14–18** August 2000. Reno, NV, pp. 689–693, doi: 10.1175/1520-0450(2001)040<1967:ACPC>2.0.CO;2.

Cober SG, Isaac GA, Korolev AV, Strapp JW. 2001. Assessing cloudphase conditions. *J. Appl. Meteorol.* **40**: 1967–1983, doi: 10.1175/1520-0450(2001)040<1967:ACPC>2.0.CO;2.

Davis A., and Marshak A. 2010. 3D transport of solar radiation in clouds. *Rep. Prog. Phys.*, **73**, 026801, doi:10.1088/0034-4885/73/2/026801.

Delanoë, J. and R. J. Hogan. 2010. Combined CloudSat-CALIPSOMODIS retrievals of the properties of ice clouds, *J. Geophys. Res.*, **115**, D00H29, doi:10.1029/2009JD012346.

Deschamps P. Y., F. M. Breon, M. Leroy, A. Podaire, A. Bricaud, J. C. Buriez and Seze G. 1994. The POLDER mission : Instrument characteristics and scientific objectives. *IEEE Transactions on Geoscience and Remote Sensing* **32**, 598-615.

Dong X and Mace GG. 2003. Arctic stratus cloud properties and radiative forcing derived from ground-based data collected at Barrow, Alaska. *J. Clim.* **16**: 445–461, doi: 10.1175/1520-0442(2003)016<0445:ASCPAR>2.0.CO;2.

Dong X., Minnis, P., Mace, G. G., Smith Jr., W. L., Poellot, M., Marchand, R. T., and Rapp, A. D.: Comparison of stratus cloud properties deduced from surface, GOES, and aircraft data during the March 2000 ARM Cloud IOP, *J. Atmos. Sci.*, **59**, 3256–3284, 2002.

Draper D. W., D. A. Newell, F. J. Wentz, S. Krimchansky and G. Skofronick-Jackson, 2015: The Global Precipitation Measurement (GPM) Microwave Imager (GMI): Instrument Overview and Early On-orbit Performance. *IEEE Journal of Selected Topics*

---

in *Applied Earth Observations and Remote Sensing*, **8**, 3452-3462, doi:10.1109/JSTARS.2015.2403303.

Draxler R, Hess G. 1998. An overview of the HYSPLIT\_4 modelling system for trajectories, dispersion and deposition. *Aust. Meteorol. Mag.* **47**: 295–308.

Ellis TD, L'Ecuyer T, Haynes JM, Stephens GL. 2009. How often does it rain over the global oceans? The perspective from CloudSat. *Geophys. Res. Lett.* **36**: L03815, doi: 10.1029/2008GL036728.

Feingold G., S. M. Kreidenweis, B. Stevens, and W. R. Cotton 1996. Numerical simulations of stratocumulus processing of cloud condensation nuclei through collision-coalescence, *J. Geophys. Res.*, **101**, 21,391–21,402, doi:10.1029/96JD01552.

Field PR, Heymsfield AJ, Bansemmer A. 2006. Shattering and particle interarrival times measured by optical array probes in ice clouds. *J. Atmos. Ocean. Technol.* **23**: 1357-1371, doi:10.1175/JTECH1922.1.

Fitzpatrick, M. F., and S.G. Warren (2007), The relative importance of clouds and sea ice for the solar energy budget of the Southern Ocean, *J. Clim.*, **20**, 941-954.

Gras JL. 1995. CN, CCN and particle size in Southern Ocean air at Cape Grim. *Atmos. Res.* **35**: 233–251, doi: 10.1016/0169-8095(94)00021-5.

Grosvenor D. P., and Wood R. 2014. On the effect of solar zenith angle on MODIS cloud optical and microphysical retrievals. *Atmos. Chem. Phys.*, **14**, 7291–7321, doi:10.5194/acp-14-7291-2014.

Gultepe, I. and Isaac, G. A. 1997. Liquid water content and temperature relationship from aircraft observations and its applicability to GCMs, *J. Climate*, **10**, 447–452.

Gultepe I, Isaac G.A. and Cober, S. G. 2002. The effects of air-mass origin on Arctic cloud microphysical parameters for April 1998 during FIRE.ACE. *J. Geophys. Res.* **107**: 4-1–4-12, doi: 10.1029/2000JC000440.

Gultepe I, Isaac G.A. 2004. Aircraft observations of cloud droplet number concentration: Implications for climate studies. *Q. J. R. Meteorol. Soc.* **130**, pp. 2377–

---

2390, doi: 10.1256/qj.03.120.

Han QY, RossowWB, Chou J. 1998. Global survey of the relationships of cloud albedo and liquid water path with droplet size using ISCCP. *J. Clim.* **11**: 1516–1528, doi: 10.1175/1520-0442(1998)011<1516:GSOTRO>2.0.CO;2.

Han QY, RossowWB, Chou J., and Welch R.M. 1998. Global variations of droplet column concentration of low-level clouds. *Geophys. Res. Lett.* **25**, 1419-1422.

Han QY, RossowWB, and Lacis A. A. 1994. Near global survey of effective droplet radii in liquid water clouds using ISCCP data, *J. Clim.*, **7**, 465-497.

Hansen, J., and L. Travis, 1974. Light scattering in planetary atmospheres, *Space Sci. Rev.*, **16**, 527–610, doi:10.1007/BF00168069.

Harrington, J. Y., and P. Q. Olsson. 2001. On the potential influence of ice nuclei on surface-forced marine stratocumulus cloud dynamics, *J. Geophys. Res.*, **106**, 27,473-27,484.

Hartmann D. L., Ockert-Bell M. E., and Michelsen M. L. 1992. The effect of cloud type on earth's energy balance – Global analysis, *J. Clim.*, **5**, 1281-1304.

Haynes, J. M., T. S. L'Ecuyer, G. L. Stephens, S. D. Miller, C. Mitrescu, N. B. Wood, and S. Tanelli. 2009, Rainfall retrieval over the ocean with spaceborne W-band radar, *J. Geophys. Res.*, **114**, D00A22, doi:10.1029/2008JD009973.

Haynes J. M., C. Jakob W. B. Rossow, G. Tselioudis, and Brown J. 2011. Major characteristics of Southern Ocean cloud regimes and their effects on the energy budget. *J. Climate*, **24**, 5061–5080, doi:10.1175/2011JCLI4052.1.

Hogan R. J., P. N. Francis, H. Flentje et al. 2003. Characteristics of mixed-phase clouds. Part I: Lidar, radar, and aircraft observations from CLARE'98, *Quart. J. Roy. Meteor. Soc.*, **129**, 2089-2116.

Holtz R. E., Ackerman S. A., Nagle F. W. 2008. Global Moderate Resolution Imaging Spectroradiometer (MODIS) cloud detection and height evaluation using CALIOP, *J. Geophys. Res.*, **113**, D00A19, doi:10.1029/2008JD009837.

---

Hoskins BJ, Hodges KI. 2005. A new perspective on Southern Hemisphere storm tracks. *J. Clim.* **18**: 4108–4109, 4111–4113, 4115–4116, 4118–4129, doi: 10.1175/JCLI3570.1.

Hou A.Y., Kakar R.K., Neeck S., Azarbarzin A.A., Kummerow C.D., Kojima M., Oki R., Nakamura K., Iguchi T. 2014. The global precipitation measurement mission. *Bull. Am. Meteorol. Soc.* **95**, 701–722.

Hu Y., and Coauthors 2009. CALIPSO/CALIOP cloud phase discrimination algorithm. *J. Atmos. Oceanic Technol.*, **26**, 2293–2309, doi:10.1175/2009JTECHA1280.1.

Hu Y, Rodier S, Xu K. 2010. Occurrence, liquid water content, and fraction of supercooled water clouds from combined CALIOP/IIR/MODIS measurements. *J. Geophys. Res.* **115**: D00H34, doi: 10.1029/2009JD012384.

Huang Y., Siems S. T., Manton M. J., Hande L. B., and Haynes J. M. 2012a. The structure of low-altitude clouds over the Southern Ocean as seen by CloudSat. *J. Climate*, **25**, 2535–2546, doi:10.1175/JCLI-D-11-00131.1.

Huang Y., Siems S. T., Manton M. J., A. Protat, and Delanoë J. 2012b. A study on the low-altitude clouds over the Southern Ocean using the DARDAR-MASK. *J. Geophys. Res.*, **117**, D18204, doi:10.1029/2012JD017800.

Huang Y, Siems ST, Manton MJ, Thompson G. 2014. An evaluation of WRF simulations of clouds over the Southern Ocean with A-Train observations. *Mon. Weather Rev.* **142**: 647–667, doi: 10.1175/MWR-D-13-00128.1.

Huang Y, Franklin CN, Siems ST, Manton MJ, Chubb TH, Lock A, Alexander S, Klekociuk A. 2015a. Evaluation of boundary-layer cloud forecasts over the Southern Ocean in a limited-area numerical weather prediction system using in situ, space-borne and ground-based observations. *Q. J. R. Meteorol. Soc.* **141**: 2259–2276, doi: 10.1002/qj.2519.

Huang Y, Protat A, Siems ST, Manton MJ. 2015b. A-Train observations of maritime mid latitude storm-track cloud systems: Comparing the Southern Ocean against the North Atlantic. *J. Clim.* **28**: 1920–1939, doi: 10.1175/JCLID- 14-00169.1.

---

Huang Y, Siems ST, MantonMJ, Rosenfeld D, Marchand R, McFarquhar GM, Protat A. 2016. What is the role of sea surface temperature in modulating cloud and precipitation properties over the Southern Ocean? *J. Clim.* **29**:7453–7476. <https://doi.org/10.1175/JCLI-D-15-0768.1>.

Huang Y, Chubb TH, Baumgardner D, Hoog M. d, Siems ST, Manton MJ, 2017. Evidence for secondary ice production in Southern Ocean open cellular convection, *Q. J. R. Meteorol. Soc.* **143**: 1685–1703, DOI: 10.1002/qj.3041.

Huffman G. J., D. T. Bolvin, D. Braithwaite, K. Hsu, R. Joyce, C. Kidd, E. J. Nelkin, and P. Xie. 2015a: NASA Global Precipitation Measurement (GPM) Integrated Multi-satellitE Retrievals for GPM (IMERG). *Algorithm Theoretical Basis Doc.*, version 4.5, 26 pp.

Huffman G. J., D. T. Bolvin, and E. J. Nelkin. 2015b: Integrated Multi-satellitE Retrievals for GPM (IMERG) technical documentation. *NASA Doc.*, 47 pp.

Huffman G. J., D. T. Bolvin, and E. J. Nelkin. 2015c: Day 1 IMERG final run release notes. *NASA Doc.*, 9 pp.

Isaac GA, Cober SG, Strapp JW, Korolev AV, Tremblay A, Marcotte DL. 2001. Recent Canadian research on aircraft in-flight icing. *Can. Aeronaut. Space J.* **7**: 213–221.

Im E., C. Wu, and S. L. Durden. 2005, Cloud profiling radar for the CloudSat mission, *IEEE Trans., Aerosp. Electron. Syst.*, **20**, 15-18.

Jensen J. B., S. Lee, P. B. Krummel 2000. Precipitation in marine cumulus and stratocumulus. Part I: Thermodynamic and dynamic observations of closed cell 133 circulations and cumulus bands, *Atmos. Research.*, **54**, 117-155.

Joiner J. A. P. Vasilkov, P. K, Bhartia, G. Wind, S. Platnick, and W. P. Menzel, 2010. Detection of multi-layer and vertically-extended clouds using A-Train sensors. *Atmos. Meas. Tech.*, **3**, 233-247.

King N. J., Bower, K. N., Crosier, J., and Crawford, I. 2013. Evaluating MODIS cloud retrievals with in situ observations from VOCALS-REx, *Atmos. Chem. Phys.*, **13**, 191-

---

209, doi:10.5194/acp-13-191-2013.

King M.D., W.P. Menzel, Y.J. Kaufman, D. Tanre, B.C. Gao, S. Platnick, S.A. Ackerman, L.A. Remer, R. Pincus, and P.A. Hubanks. 2003. Cloud and aerosol properties, precipitable water, and profiles of temperature and water vapor from MODIS. *IEEE Transactions on Geoscience and Remote Sensing* **41**: 442–458.

Kogan Y. L., M. P. Khairoutdinov, D. K. Lilly, Z. N. Kogan, and Q. Liu 1995. The simulation of a convective cloud in a 3-D model with explicit microphysics. Part I: Model description and sensitivity experiments. *J. Atmos. Sci.*, **52**, 2923–2940.

Korolev AV. 2007. Reconstruction of the sizes of spherical particles from their shadow images. Part I: Theoretical considerations. *J. Atmos. Oceanic Technol.* **24**: 376–389, doi: 10.1175/JTECH1980.1.

Korolev AV, Emery EF, Strapp JW, Cober SG, Isaac GA. 2013. Quantification of the effects of shattering on airborne ice particle measurements. *J. Atmos. Oceanic Technol.* **30**: 2527–2553, doi: 10.1175/JTECH-D-13-00115.1.

Korolev AV and Isaac GA. 1998. ‘Phase composition of stratiform clouds’. In proceedings of *FAA Workshop on Mixed-Phase and Glaciated Icing Conditions*, 2–3 December 1998. Federal Aviation Authority: Atlantic City, NJ, pp. 689–693.

Korolev AV and Isaac GA. 2000. ‘Phase composition of stratiform clouds’. In Proceedings of 13th *International Conference on Clouds and Precipitation*, 14–18 August, 2000. Reno, NV, pp. 725–727.

Korolev AV, Isaac GA, Cober SG, Strapp JW, Hallett J. 2003. Microphysical characterization of mixed-phase clouds. *Q. J. R. Meteorol. Soc.* **129**: 39– 65. doi: 10.1256/qj.01.204.

Korolev AV, G. McFarquhar, P. R. Field, C. Frankline, P. Lawson, Z. Wang, E. Williams, S. J. Abel, D. Axisa, S. Borrmann, J. Crosier, J. Fugal, M. Krämer, U. Lohmann, O. Schellnberger, M. Schnaiter, and M. Wendisch. 2017. Chapter 5. Mixed-Phase Clouds: Progress and Challenges. *Monograph, AMS*. **58**. <https://doi.org/10.1175/AMSMONOGRAPHS-D-17-0001.1>.

---

Lebsock, M. D. and T. S. L'Ecuyer, 2011: The Retrieval of Warm Rain from CloudSat. *J. Geophys. Res.*, **116**, doi:10.1029/2011JD016076.

Lebsock M. D., T. S. L'Ecuyer and Stephens G. L. 2011. Detecting the ratio of rain and cloud water in low-latitude shallow marine clouds. *J. Appl. Meteorol. Clim.*, **50**, 419-432.

Liang L., L. Di Girolamo, and S. Platnick. 2009. View-angle consistency in reflectance, optical depth, and spherical albedo of marine water clouds off the coast of California through MISR-MODIS fusion. *Geophys. Res. Lett.*, **36**, L09811, doi: 10.1029/2008GL037124.

Lilie L, Emery E, Strapp JW, Emery J. 2005. 'A multiwire hot-wire device for measurement of icing severity, total water content, liquid water content, and droplet diameter'. *43rd AIAA Aerospace Sciences Meeting and Exhibit*, 10–13 January 2005. Aerospace Sciences Meetings. Reno, NV.

Liu Z and coauthors. 2005. CALIOP Algorithm Theoretical Basis Document. PC-SCI-202 Part 3. Scene Classification Algorithms. NASA.

Mace G. G. 2010. Cloud properties and radiative forcing over the maritime storm tracks of the Southern Ocean and North Atlantic derived from A-Train. *J. Geophys. Res.*, **115**, D10201, doi:10.1029/2009JD012517.

Mace GG, Marchand R, Zhang Q. 2007. Global hydrometeor occurrence as observed by CloudSat: Initial observations from summer 2006. *Geophys. Res. Lett.* **34**: L09808, doi: 10.1029/2006GL029017.

Marchand RT, Mace GG, Ackerman TP. 2008. Hydrometeor detection using CloudSat, an Earth orbiting 94 GHz cloud radar. *J. Atmos. Oceanic Technol.* **25**: 531–546, doi: 10.1175/2007JTECHA1006.1.

Marchant B., S. Platnick, K. Meyer, G. T. Arnold, and Riedi J. 2016. MODIS Collection 6 shortwave-derived cloud phase classification algorithm and comparisons with CALIOP. *Atmos. Meas. Tech.*, **9**, 1587–1599, doi:10.5194/amt-9-1587-2016.

---

Martin S. T., Artaxo, P., Machado, L. A. T., Manzi, A. O., Souza, R. A. F., Schumacher, C., Wang, J., Andreae, M. O., Barbosa, H. M. J., Fan, J., Fisch, G., Goldstein, A. H., Guenther, A., Jimenez, J. L., Pöschl, U., Silva Dias, M. A., Smith, J. N., and Wendisch, M.: Introduction: Observations and Modeling of the Green Ocean Amazon (GoAmazon2014/5), *Atmos. Chem. Phys.*, **16**, 4785-4797, doi:10.5194/acp-16-4785-2016, 2016.

Mazin IP, Nevzorov AN, Shugaev VP, Korolev AV. 1992. 'Phase structure of stratiform clouds'. In Proceedings of **11th International Conference on Clouds and Precipitation**, 17–21 August, 1992. Montreal, Canada, pp. 332–336.

McCoy DT, Burrows SM, Wood R, Grosvenor DP, Elliott SM, Ma P, Rasch PJ, Hartmann DL. 2015. Natural aerosols explain seasonal and spatial patterns of Southern Ocean cloud albedo. *Sci. Adv.* **1**: e1500157, doi: 10.1126/sciadv.1500157.

McFarquhar G. M. and Cober S. G. 2004. Single-scattering properties of mixed-phase Arctic clouds at solar wavelengths: Impacts on radiative transfer, *J. Clim.*, **17**, 3799–3813.

McFarquhar G. M., and Coauthors, 2017: Processing of ice cloud in situ data collected by bulk water, scattering, and imaging probes: Fundamentals, uncertainties, and efforts toward consistency. Ice Formation and Evolution in Clouds and Precipitation: Measurement and Modeling Challenges, *Meteor. Monogr.*, No. **58**, *Amer. Meteor. Soc.*, doi:10.1175/AMSMONOGRAPHS-D-16-0007.1.

Strapp JW, J Oldenburg, Ide R, Lilie L, Bacic S, Vukovic Z, Oleskiw M, Miller D, Emergy E, Leone G. 2003. Wind tunnel measurements of the response of hot-wire liquid water content instruments to large droplet. *J. Atmos. Oceanic Technol.* **20**: 791–806. doi: [http://dx.doi.org/10.1175/1520-0426\(2003\)020<0791:WTMOTR>2.0.CO;2](http://dx.doi.org/10.1175/1520-0426(2003)020<0791:WTMOTR>2.0.CO;2).

Menzel W. P., R. A. Frey, H. Zhang, D. P. Wylie, C. C. Moeller, R. E. Holz, B. Maddux, B. A. Baum, K. I. Strabala, and L. E. Gumley, 2008: MODIS global cloud-top pressure and amount estimation: Algorithm description and results. *J. Appl. Meteor. Climatol.*, **47**, 1175–1198, doi:10.1175/2007JAMC1705.1.

- 
- Min Q., Joseph, E., Lin, Y., Min, L., Yin, B., Daum, P. H., Kleinman, L. I., Wang, J., and Lee, Y.-N. 2012. Comparison of MODIS cloud microphysical properties with in-situ measurements over the Southeast Pacific, *Atmos. Chem. Phys.*, **12**, 11261-11273, doi:10.5194/acp-12-11261-2012.
- Mitrescu C., T. L'Ecuyer, J. M. Haynes, S. D. Miller, and Turk F. J. 2010. CloudSat precipitation profiling algorithm—Model description. *J. Appl. Meteor. Climatol.*, **49**, 991–1003, doi:10.1175/2009JAMC2181.1.
- Morrison AE, Siems ST, Manton MJ. 2013. On a natural environment for glaciogenic cloud seeding. *J. Appl. Meteorol. Climatol.* **52**: 1097–1104, doi: 10.1175/JAMC-D-12-0108.1.
- Morrison AE, Siems ST, Manton MJ, Nazarov A. 2010. A modelling case study of mixed phase clouds over the Southern Ocean and Tasmania. *Mon. Weather Rev.* **138**: 839–862, doi: 10.1175/2009MWR3011.1.
- Morrison AE., S. T. Siems, and M. J. Manton. 2011. A Cloud-top Phase Climatology of Southern Ocean Clouds, *J. Clim.*, **24**, 2405–2418.
- Mossop S, C. 1985. The origin and concentration of ice crystals in clouds. *Bull. Amer. Meteor. Soc.*, **66**, 264-273.
- Mossop S, C, Ono A, Wishart ER. 1970. Ice particles in maritime clouds near Tasmania. *Q. J. R. Meteorol. Soc.* **96**: 487–508, doi: 10.1002/qj. 49709640910.
- Muhlbauer A, McCoy IL, Wood R. 2014. Climatology of stratocumulus cloud morphologies: Microphysical properties and radiative effects. *Atmos. Chem. Phys.* **14**: 6695–6716, doi: 10.5194/acp-14-6695-2014.
- Nakajima, T., and M. D. King. 1990, Determination of the optical thickness and effective particle radius of clouds from reflected solar radiation measurements. Part I: Theory, *J. Atmos. Sci.*, **47**(15), 1878–1893, doi:10.1175/1520-0469(1990)047<1878:DOTOTA>2.0.CO;2.
- Nakajima T. Y., K. Suzuki, and Stephens G. L. 2010a. Droplet growth in warm water

---

clouds observed by the A-train. Part I: Sensitivity analysis of the MODIS-derived cloud droplet sizes, *J. Atmos. Sci.*, **67**(6), 1884–1896, doi:10.1175/2009JAS3280.1.

Nakajima, T. Y., Suzuki K., Stephens G. L. 2010b. Droplet Growth in Warm Water Clouds Observed by the A-Train. Part II: A Multisensor View, *Journal of the Atmospheric Sciences*, vol. **67**, issue 6, pp. 1897-1907.

National Science Foundation (NSF). 2014. Investing in Science, Engineering, and Education for the Nation's Future, Strategic Plan for 2014 – 2018.

Oreopoulos L., and Davies R. 1998. Plane parallel albedo biases from satellite observations. Part I: Dependence on resolution and other factors, *J. Clim.*, **11**, 919–932., [https://doi.org/10.1175/1520-0442\(1998\)011<0919:PPABFS>2.0.CO;2](https://doi.org/10.1175/1520-0442(1998)011<0919:PPABFS>2.0.CO;2).

Painemal, D. and Zuidema, P.: Assessment of MODIS cloud effective radius and optical thickness retrievals over the Southeast Pacific with VOCALS-REx in situ measurements, *J. Geophys. Res.*, **116**, D24206, doi:10.1029/2011JD016155, 2011.

Partain P. 2007. CloudSat ECMWF-AUX Auxiliary Data Process Description and Interface Control Document. CloudSat Project CIRA. Colorado State University: Fort Collins, CO.

Pavolonis M. J., and A. K. Heidinger 2004. Daytime cloud overlap detection from AVHRR and VIIRS. *J. Appl. Meteor.*, **43**, 762-778.

Pawlowska H., and Brenguier J.-L. 2003. An observational study of drizzle formation in stratocumulus clouds for general circulation model (GCM) parameterizations, *J. Geophys. Res.*, **108**(D15), 8630, doi:10.1029/2002JD002679.

Platnick S. 2000. Vertical photon transport in cloud remote sensing problems. *J. Geophys. Res.*, **105**, 22919-22935.

Platnick S., and Valero F. P. J. 1995. A validation study of a satellite cloud retrieval during ASTEX. *J. Atmo. Sci.*, **52**, 2985-3001.

Platnick, S., M. D. King, S. A. Ackerman et al. 2003. The MODIS cloud products: Algorithms and examples from Terra, *IEEE Trans, Geosci. Remote Sens.*, **41**(2), 459-

---

473.

Platnick S. and Coauthors 2015. MODIS Cloud Optical Properties: User Guide for the Collection 6 Level-2 MOD06/MYD06 product and associated level-3 datasets. *NASA Goddard Space Flight Center*, 34 pp.

Platnick S., Kerry G. Meyer, Michael D. King, Fellow, IEEE, Galina Wind, Nandana Amarasinghe, Benjamin Marchant, G. Thomas Arnold, Zhibo Zhang, Paul A. Hubanks, Robert E. Holz, Ping Yang, William L. Ridgway, and Jérôme Riedi 2017. "The MODIS Cloud Optical and Microphysical Products: Collection 6 Updates and Examples From Terra and Aqua," in *IEEE Transactions on Geoscience and Remote Sensing*, vol. **55**, no. 1, pp. 502-525, Jan. 2017. doi: 10.1109/TGRS.2016.2610522.

Powell K., and Coauthors 2010. The CALIOP 532-nm channel daytime calibration: Version 3 algorithm. Proc. **25th Int. Laser Radar Conf.**, St. Petersburg, Russia, Intl. Radiation Commission, 1367–1370.

Protat A, Delanoë J, O'Connor E, L'Ecuyer T. 2010. The evaluation of CloudSat-derived ice microphysical products using ground-based cloud radar and lidar observations. *J. Atmos. Oceanic Technol.* **27**: 793–810, doi: 10.1175/2009JTECHA1397.1.

Pruppacher HR, Klett JD. 1997. *Microphysics of Clouds and Precipitation*. *Kluwer Academic*, 954 pp.

Pruppacher HR and Klett JD. 2010. *Microphysics of Clouds and Precipitation*, Chapter 10. Springer, doi: 10.1007/978-0-306-48100-0: Houten, Netherlands.

Puri K, Dietachmayer G, Steinle P, Dix M, Rikus L, Logan L, Naughton M, Tingwell C, Xiao Y, Barras V, Bermous I, Bowen R, Deschamps L, Franklin C, Fraser J, Glowacki T, Harris B, Lee J, Le T, Roff G, Sulaiman A, Sims H, Sun X, Sun Z, Zhu H, Chattopadhyay M, Engel C. 2013. Implementation of the initial ACCESS numerical weather prediction system. *Aust. Meteorol. Oceanogr. J.* **63**: 265–284.

Quinn P and Bates T. 2011. The case against climate regulation via oceanic phytoplankton sulphur emissions. *Nature* **480**: 51–56, doi: 10.1038/nature10580.

---

Risbey JS, Pook MJ, McIntosh PC, Ummenhofer CC, Meyers G. 2009. Characteristics and variability of synoptic features associated with cool season rainfall in southeastern Australia. *Int. J. Climatol.* **29**: 1595–1613, doi: 10.1002/joc.1775.

Rosenfeld D., and Coauthors, 2013b: The common occurrence of highly supercooled drizzle and rain near the coastal regions of the western United States. *J. Geophys. Res. Atmos.*, **118**, 9819–9833, doi:10.1002/jgrd.50529.

Rosenfeld D., Wang H, Rasch PJ. 2012. The roles of cloud drop effective radius and LWP in determining rain properties in marine stratocumulus, *Geophys. Res. Lett.* 39: L13801, doi: 10.1029/2012GL0 52028. Simmonds I, Keay K. 2000. Mean Southern Hemisphere extratropical cyclone behavior in the 40-year NCEP–NCAR reanalysis. *J. Clim.* **13**: 873–885, doi: 10.1175/ 1520-0442(2000)013,0873:MSHECB.2.0.CO;2.

Russell L. M., D. H. Lenschow, K. K. Laursen et al. 1998. Bidirectional mixing in an ACE 1 marine boundary layer overlain by a second turbulent layer, *J. Geophys. Res.*, **103** (D13), 16411–16432.

Seethala C., and Horváth Á. 2010. Global assessment of AMSR-E and MODIS cloud liquid water path retrievals in warm oceanic clouds, *J. Geophys. Res.*, **115**, D13202, doi:10.1029/2009JD012662.

Shupe M. D. 2011. Clouds at Arctic atmospheric observatories. Part II: Thermodynamic phase characteristics, *J. Appl. Meteorol. Clim.*, **50**, 645-661.

Shupe M. D., and J. M. Intrieri. 2004, Cloud radiative forcing of the Arctic surface: The influence of cloud properties, surface albedo, and solar zenith angle, *J. Clim.*, **17**, 616-628.

Simmonds I., and Keay K. 2000. Mean Southern Hemisphere extratropical cyclone behavior in the 40-Year NCEP–NCAR Reanalysis, *J. Clim.*, **13**, 873–885.

Smith RNB. 1990. A scheme for predicting layer clouds and their water contents in a general circulation model. *Q. J. R. Meteorol. Soc.* **116**: 435–460.

Squires P. 1952. The growth of cloud drops by condensation. 1: General characteristics.

---

Aust. *J. Sci. Res.*, **5**, 59–86.

Stephens G.L., D.G. Vane, R.J. Boain, G.G. Mace, K. Sassen, Z.E. Wang, A.J. Illingworth, O'Connor E.J., Rossow W.B., Durden S.L., Miller S.D., Austin R.T., Benedetti A., and Mitrescu C. 2002. The CloudSat mission and the A-Train —A new dimension of space-based observations of clouds and precipitation. *Bulletin of the American Meteorological Society* **83**: 1,771-1,790, doi:10.1175/BAMS-83-12-1771.

Stephens G.L. and Coauthors. 2010. Dreary state of precipitation in global models. *J. Geophys. Res.*, **115**, D24211, doi:10.1029/2010JD014532.

Suzuki K., T. Y. Nakajima, and Stephens G. L. 2010. Particle growth and drop collection efficiency of warm clouds as inferred from joint CloudSat and MODIS observations, *J. Atmos. Sci.*, **67**(9), 3019–3032, doi:10.1175/2010JAS3463.1.

Trenberth K. E., 1991. Storm tracks in the Southern Hemisphere. *J. Atmos. Sci.*, **48**, 2159–2178, doi:10.1175/1520-0469(1991)048<2159:STITSH.2.0.CO;2.

Trenberth K. E. and Fasullo JT. 2010. Simulation of present-day and twenty-first century energy budgets of the Southern Oceans. *J. Clim.* **23**: 440–454, doi:10.1175/2009JCLI3152.1.

Twomey S. A. 1977. Storm Tracks in the Southern Hemisphere, *J. Atmos. Sci.*, **34**, 1149-1152.

Vallina S. and R. Simo 2007. Strong relationship between DMS and the solar radiation dose over the global surface ocean, *Science*, **315**, 506-508.

Vaughan HY, , M., McClain, C., Behrenfeld, M., Maring, H., Anderson, D., Sun-Mack, S., Flittner, D., Huang, J., Wielicki, B., Minnis, P., Weimer, C., Trepte, C., and Kuehn, R. 2007. Global statistics of liquid water content and effective number concentration of water clouds over ocean derived from combined CALIPSO and MODIS measurements, *Atmos. Chem. Phys.*, **7**, 3353-3359, doi:10.5194/acp-7-3353-2007.

Vinoth J., and I. R. Young. 2011. Global estimates of extreme wind speed and wave height, *J. Clim.*, **24**(6), 1647–1665, doi:10.1175/2010JCLI3680.1.

- 
- Wang Q., D. H. Lenschow, L. Pan 1999. Characteristics of the marine boundary layers during two Lagrangian measurement periods 2 Turbulence structure, *J. Geophys. Res.*, **104**, 21767–21784.
- Wang S., Q. Wang, and G. Feingold 2003. Turbulence, condensation, and liquid water transport in numerically simulated nonprecipitating stratocumulus clouds. *J. Atmos. Sci.*, **60**, 262–278.
- Wang Z., S. T. Siems, D. Belusic', M. J. Manton, and Huang Y. 2015. A climatology of the precipitation over the Southern Ocean as observed at Macquarie Island. *J. Appl. Meteor. Climatol.*, **54**, 2321–2337, doi:10.1175/JAMC-D-14-0211.1.
- Wendisch M, Brenguier JL. 2013. In Situ Measurements of Cloud and Precipitation Particles, in: Airborne Measurements for Environmental Research: Methods and Instruments. *Wiley-VCH*, Berlin: pp 611.
- Wentz F. J. and T. Meissner (2000), AMSR algorithm theoretical basis document, version 2, *Remote Sens. Syst.*, Santa Rosa, Calif.
- Wilson DR, Ballard SP. 1999. A microphysically based precipitation scheme for the UK Meteorological Office Unified Model. *Q. J. R. Meteorol. Soc.* **125**: 1607–1636.
- Wind G. S., Platnick M. D., King P. A., Hubanks M. J., Pavolonis A. K., Heidinger P. Yang and B. A. Baum 2010. Multilayer cloud detection with the MODIS near-infrared water vapor absorption band. *J. Appl. Meteor. Climatol.*, **49**, 2315-2333.
- Winker D. M. 1997. LITE: Results, performance characteristics, and data archive. Proceedings of *SPIE* **3218**: 186-193.
- Winker D. M, Hunt B. H., and McGill M. J. 2007. Initial performance assessment of CALIOP, *Geophys. Res. Lett.*, **34**, L19803.
- Winker D. M, Mark A. Vaughan, Ali Omar, Yongxiang Hu, and Kathleen A. Powell, Zhaoyan Liu, William H. Hunt, Young Stuart A. 2009. Overview of the CALIPSO Mission and CALIOP Data Processing Algorithms. *J. Atmos. Oceanic Technol.*, **26**, 2310–2323, Doi :<https://doi.org/10.1175/2009JTECHA1281.1>.

- 
- Wofsy S. 2011. HIAPER Pole-to-Pole Observations (HIPPO): Fine-grained, global-scale measurements of climatically important atmospheric gases and aerosols. *Philos. Trans. R. Soc. A.* **369**: 2073–2086, doi: 10.1098/rsta. 2010.0313.
- Wolters E. L. A., H. M. Deneke, B. J. J. M. van den Hurk, J. F. Meirink, and Roebeling R. A. 2010. Broken and inhomogeneous cloud impact on satellite cloud particle effective radius and cloudphase retrievals. *J. Geophys. Res.*, **115**, D10214, doi:10.1029/2009JD012205.
- Woods CP, Waliser DE, Li JL, Austin RT, Stephens GL, Vane DG. 2008. Evaluating CloudSat ice water content retrievals using a cloud-resolving model: Sensitivities to frozen particle properties. *J. Geophys. Res.* **113**: D00A11, doi: 10.1029/2008JD009941.
- Wood R. 2000. Parameterization of the effect of drizzle upon the droplet effective radius in stratocumulus clouds, *Q. J. Roy. Meteor. Soc.*, **26**, 3309–3324. doi:10.1002/qj.49712657015.
- Wood R. 2005. Drizzle in stratiform boundary layer clouds. Part 1: Vertical and horizontal structure, *J. Atmos. Sci.*, 62, 3011 –3033.
- Wood R. 2012a. Stratocumulus clouds. *Mon. Weather Rev.* **140**: 2373–2423, doi: 10.1175/MWR-D-11-00121.1.
- Wood R., Bretherton C, Leon D, Clarke A, Zuidema P, Allen G, Coe H. 2011. An aircraft case study of the spatial transition from closed to open mesoscale cellular convection over the southeast Pacific. *Atmos. Chem. Phys.* **11**: 2341–2370, doi: 10.5194/acp-11-2341-2011.
- Wood R. and Field PR. 2011. The distribution of cloud horizontal sizes. *J. Clim.* **24**: 4800–4816, doi: 10.1175/2011JCLI4056.1.
- Wood R. and Hartmann DL. 2006. Spatial variability of liquid water path in marine boundary layer clouds: The importance of mesoscale cellular convection. *J. Clim.* **19**: 1748–1764, doi: 10.1175/JCLI3702.1.
- Wood R., Leon D, Lebsock M, Snider J, Clarke AD. 2012b. Precipitation driving of

---

droplet concentration variability in marine low clouds. *J. Geophys. Res.* **117**: D19210, doi: 10.1029/2012JD018305.

Yin, J. H. (2005), A consistent poleward shift of the storm tracks in simulations of 21st century climate, *Geophys. Res. Lett.*, **32**, L18701.

Yum, S.S., Hudson, J.G., 2004. Wintertime/summertime contrasts of cloud condensation nuclei and cloud microphysics over the Southern Ocean. *J. Geophys. Res.* **109**, D06204.

Zanten van, M., Stevens and B. 2005. Observations of the structure of heavily precipitating marine stratocumulus, *J. Atmos. Sci.*, **62**, 4327 – 4342.

Zelinka M. D., and Hartmann D. L. 2012. Climate feedbacks and their implications for poleward energy flux changes in a warming climate, *J. Clim.*, **25**, 608-624.

Zhang, J., and U. Lohmann 2003, Sensitivity of single column model simulations of Arctic springtime clouds to different cloud cover and mixed phase cloud parameterization, *J. Geophys. Res.*, **108**, 4439.

Zhang Z., A. S. Ackerman, G. Feingold, S. Platnick, R. Pincus, and H. Xue, 2012: Effects of cloud horizontal inhomogeneity and drizzle on remote sensing of cloud droplet effective radius: Case studies based on large-eddy simulations. *J. Geophys. Res.*, **117**, D19208, doi:10.1029/2012JD017655.

Zhang Z. and Platnick S. 2011. An assessment of differences between cloud effective particle radius retrievals for marine water clouds from three MODIS spectral bands. *J. Geophys. Res.*, **116**, D20215, doi:10.1029/2011JD016216.

Zheng X., Albrecht, B., Jonsson, H. H., Khelif, D., Feingold, G., Minnis, P., Ayers, K., Chuang, P., Donaher, S., Rossiter, D., Ghate, V., Ruiz-Plancarte, J., and Sun-Mack, S. 2011. Observations of the boundary layer, cloud, and aerosol variability in the southeast Pacific near-coastal marine stratocumulus during VOCALSREx, *Atmos. Chem. Phys.*, **11**, 9943–9959, doi:10.5194/acp-11-9943-20.

---

## Notation

4DVAR	Four-Dimensional Variational Data Assimilation
ACCESS	Australian Community Climate and Earth System Simulator
ACCESS-VT	ACCESS Victoria–Tasmania’
APS1	Australian Parallel Suite version 1
BoM	Australian Bureau of Meteorology
CALIOP	Cloud-Aerosol Lidar with Orthogonal Polarization
CALIPSO	Cloud–Aerosol Lidar and Infrared Pathfinder Satellite Observations
CAS	Cloud Aerosol Spectrometer
CCN	Cloud Condensation Nuclei
CIP	Cloud Imaging Probe
CMLF	Cloud multi-layer flag
CM_SPI	Cloud mask sub-pixel heterogeneity index
COT	Cloud optical thickness
CPOP	Cloud phase optical property
CPR	Cloud Profiling Radar
CSR	Clear sky restoral
CTH	Cloud top height
CTP	Cloud-top pressure
CTT	Cloud top temperature
DPR	Dual-Frequency Precipitation Radar
ECMWF	European Centre for Medium-range Weather Forecasts
GMI	GPM Microwave Imager
GPM	Global Precipitation Measurement
HOI	Horizontally-oriented ice
IMERG	Integrated Multi-Satellite Retrievals for GPM

---

IR	Infrared
MCC	Mesoscale Cellular Convection
MODIS	MODerate-resolution Imaging Spectroradiometer
$N_d$	Cloud droplet number concentration
NSF	National Science Foundation
NWP	Numerical Weather Prediction
PC	2C-PRECIP-COLUMN
PCL	Partly cloudy
PP	Pixel population
PR	Precipitation Radar
$r_{eff}$	Cloud effective radius
ROI	Randomly-oriented Ice
RP	2C-RAIN-PROFILE
RR	Rain rate
SDS	Science data set
SOCEX	Southern Ocean Cloud Experiment
SZA	Solar zenith angle
SO	Southern Ocean
TRMM	Tropical Rainfall Measuring Mission
UD	Undetermined
UM/VAR	Unified Model/Variational Assimilation
UN/ND	Unknown/not determined
VFM	Vertical feature mask
VOCALS-REx	Variability of the American Monsoon Systems (VAMOS) Ocean- Cloud-Atmosphere-Land Study Regional Experiment

---

# APPENDIX

## Cloud seeding flights

Hydro Tasmania conducts about 30 - 50 seeding flights (Morrison *et al.*, 2013, 2010) per year. Over the three-year period studied, the research only includes observations from eight flights, which are deemed to be 'suitable' for analysis. Cloud seeding was actually not even attempted on two of these eight operational flights (20130803 and 20130707) due to marginal seeding conditions. These seeding flights were conducted aiming for the Lake Gordon catchment (Figure A1, Operational flight).

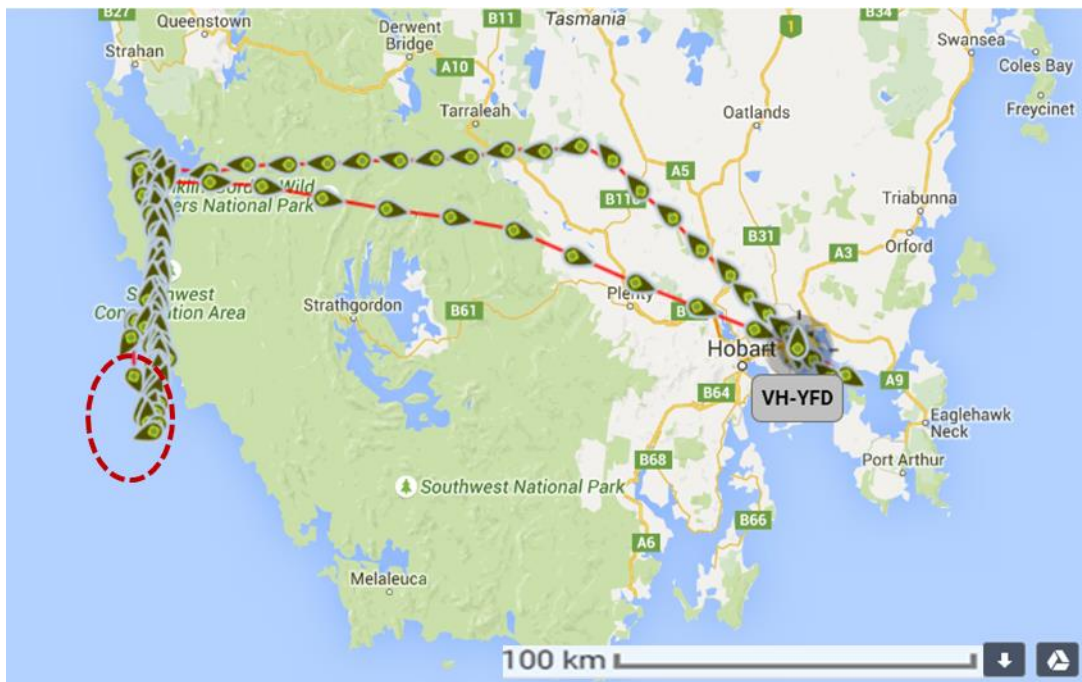


Figure A1. The cloud seeding map in in 4<sup>th</sup> August 2015. The map below shows the flight path for a cloud seeding flight targeting the Gordon catchment. The average wind direction was westerly (270) with a speed of 25 knots. The broken lined circle is where the clouds selected for the analysis.

---

These observations were done over the open ocean upwind of any seeding activity to perform thermodynamic soundings and/or de-icing where the altitude is relatively low compared to that of seeding conducted.

## **Error estimates**

The measurement uncertainties and limitations of light scattering and imaging spectrometers, like the CAS and CIP, respectively, have been evaluated in many studies. They are summarized in the book by Wendisch and Brenguier (2013) and a new monograph to be published by the American Meteorological Society (Baumgardner *et al.*, 2016; McFarquhar *et al.*, 2017). The estimated sizing accuracy of the CAS is  $\pm 20\%$  for water droplets and  $\pm 30\%$  when measuring ice crystals. The uncertainty in number concentration is  $\pm 15\%$  when measuring  $< 300 \text{ cm}^{-3}$ . The root sum squared error (RSS) in derived LWC is 38% and 54% for LWC and IWC, respectively. The CIP sizing accuracy is the same for droplets or ice crystals, but varies with size, with an average uncertainty of  $\pm 25\%$ . The concentration uncertainty is also size dependent but on average is estimated to be  $\pm 20\%$ . The largest uncertainties are for particles  $< 100 \text{ }\mu\text{m}$  because of some particles that, while detected, are out of focus and whose images are larger than the physical size. This can produce as much as a 50% positive bias that can be partially corrected (Korolev *et al.*, 2007). The propagated error in derived LWC/IWC is  $\pm 48\%$ ; however, this does not account for the uncertainties in the assumed volume and density of ice crystals. The size errors due to being out of focus are corrected by using SODA software.

The SEA WCM-2000 is a relatively new probe but its usage is increasing (Rosenfeld *et al.*, 2013; Martin *et al.* 2016). The WCM-2000 is similar to the Nevzorov probe with similar limitations and uncertainties. Although it does have a better response to larger

droplets than the single element hotwire probes (Biter *et al.*, 1987; Strapp *et al.*, 2003) wind tunnel studies shows that there might still be some under estimation of the water in larger drops due to splashing and incomplete evaporation (Lilie *et al.*, 2005). In addition, similar to the Nevzorov and single element hotwire sensors (Cober *et al.*, 2001), wind tunnel studies have shown that the cylindrical LWC elements of the WCM-2000 will respond to ice crystal; however, with a sensitivity less than 10% of the liquid fraction.

As an example, a comparison of LWC collected by the LWC083 and the LWC021 for the 14 June 2013 flight was made in (Figure A2 (a)). A comparison of the LWC from the CAS and the LWC021 returned a correlation of 0.82 (Figure A2 (b)). The agreement between the CAS and LWC021 is well within the expected uncertainties. The CAPS is installed underneath the left wing of the aircraft and the WCM is on the right wing. As such much of the scatter may be attributed to the distance between them, as well as to the possibility that different parts of the clouds are being measured by the different instruments.

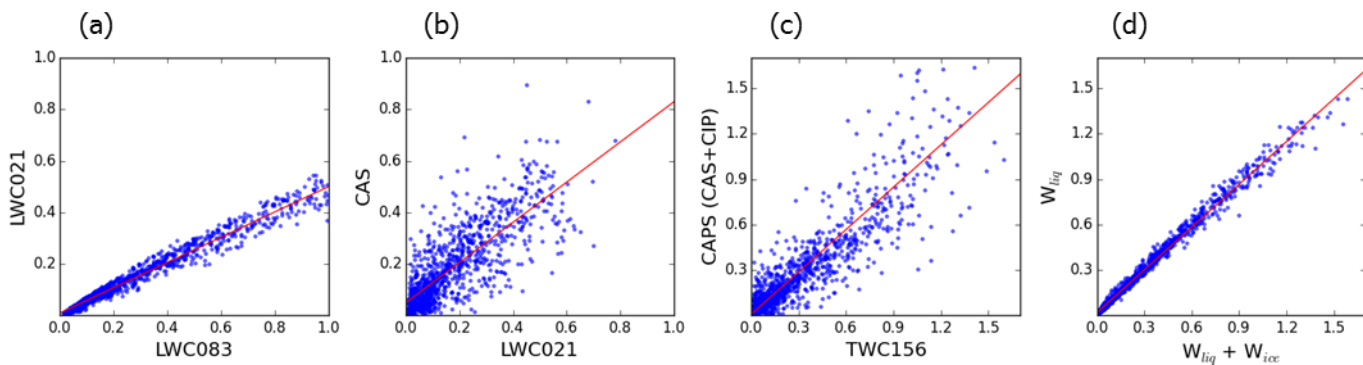


Figure A2. Comparisons of LWC [ $\text{gm}^{-3}$ ] from different measurements for 14 June 2013 flight, as noted. The correlation coefficients for (a) – (d) are 0.99, 0.79, 0.82, and 0.99, respectively and their linear regression equations are  $y = 0.49x + 0.01$ ,  $y = 0.78x + 0.05$ ,  $y = 0.93x + 0.01$ , and  $y = 0.94x + 0.02$ , respectively.

---

## CIP data processing

The SODA software used for CIP data processing provides several options. The ‘circle-fit’ method is used for sizing droplets that fit within the smallest possible circle around a particle image and uses the diameter of that circle as the size of the particle. The area ratio (particle’s projected cross-sectional area divided by the area of a circle having the particle’s maximum dimension) is used to separate water droplets from ice crystals. Under ‘water processing’ option, the particles are rejected if the area ratio is smaller than 0.4. Shattering particles are identified and corrected with the “Shatter Correct” option based on the particle by particle inter-arrival time, i.e. the time between neighboring particles (Field *et al.*, 2006). A threshold of  $10^{-4}$  sec is used to filter potential shattered particles in our analysis. The “All-In” option is used to process only particles that are fully imaged and do not touch an edge of the CIP array. A particle covering more than 10 pixels having an area ratio smaller than 0.5 is also rejected as a potential shattered particle image. In addition, corrections to spherical particles out of focus are implemented using the technique described in Korolev (2007).

## Calculation of liquid and ice water content from WCM-2000

Assuming that the measurement technique of the WCM is similar to that of the Nevzorov probe, TWC and LWC are derived from the WCM probes following Korolev *et al.* (1998, 2003).

$$TWC = \varepsilon_{liqT} W_{liq} + k\varepsilon_{iceT} W_{ice} \quad (1)$$

$$LWC = \varepsilon_{liqL} W_{liq} + \beta W_{ice} \quad (2)$$

where  $\varepsilon_{liqT}$  and  $\varepsilon_{iceT}$  are the integrated collection of efficiencies of liquid droplets and ice particles for the TWC156, respectively.  $\varepsilon_{liqL}$  is the integrated collection efficiency

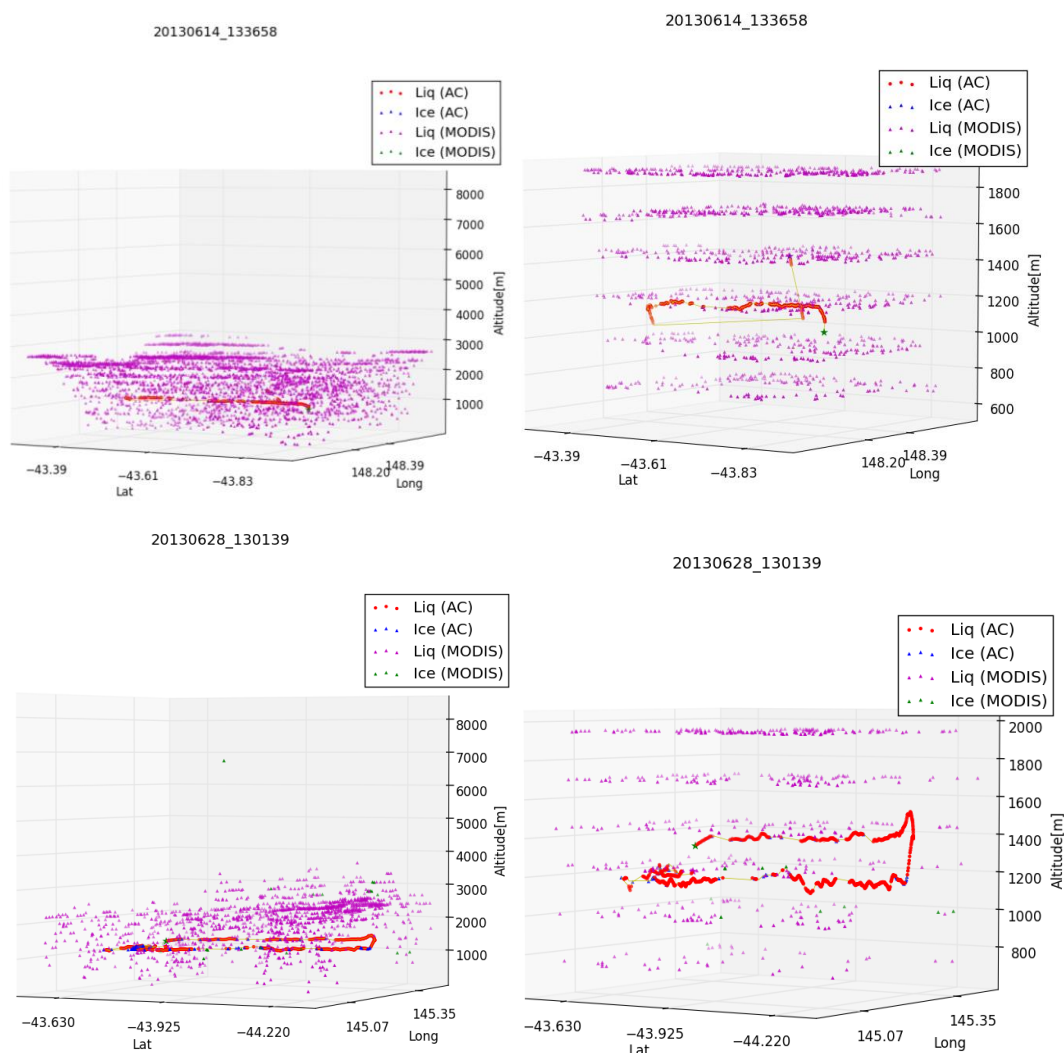
---

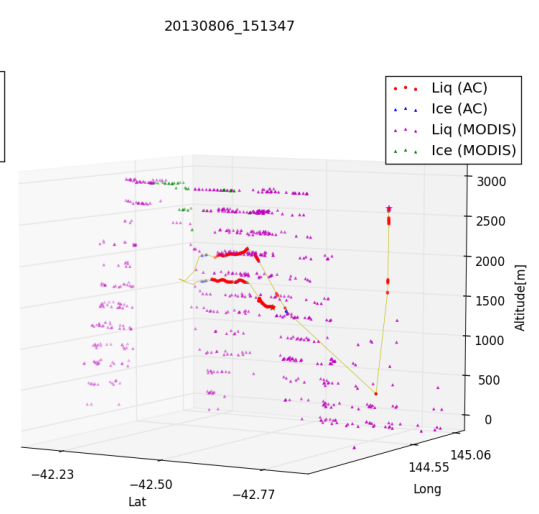
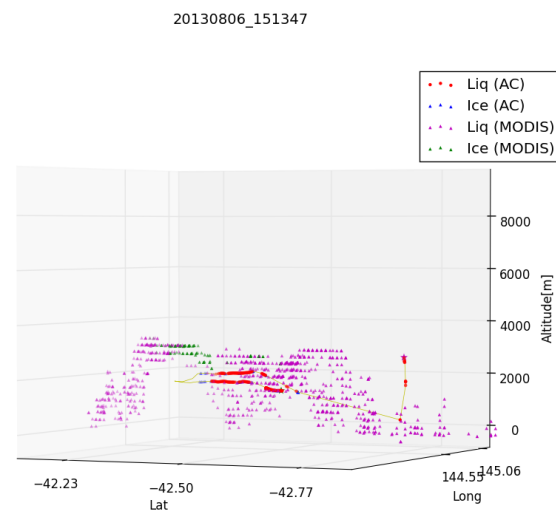
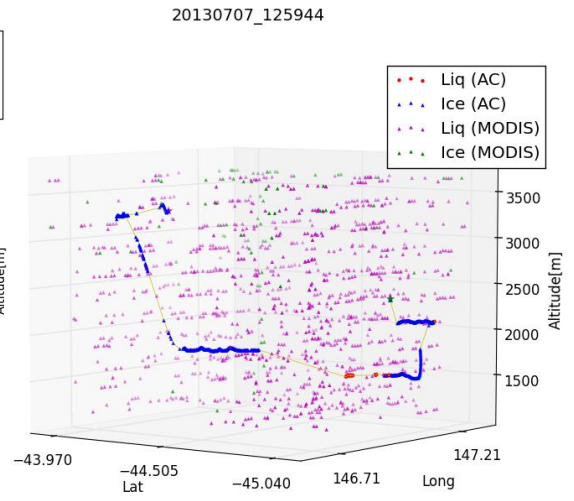
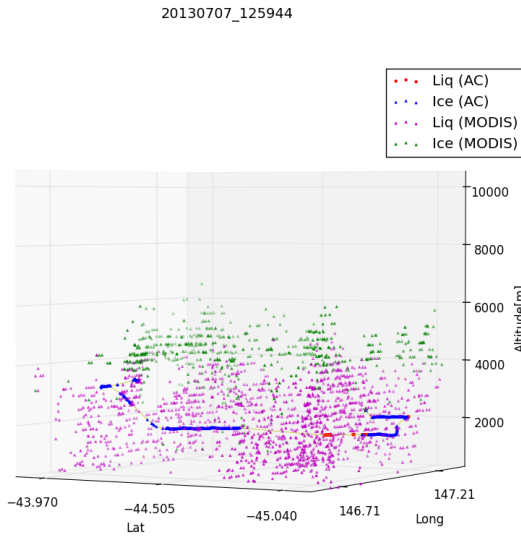
for liquid droplets for the LWC083,  $\beta$  is the coefficient accounting for the residual effect of the ice on the LWC083, and  $k$  is the correction coefficient for the difference between expended specific energy of water evaporation and ice sublimation. Following the method in Korolev *et al.* (2003), the integrated collection efficiencies were all assumed to be unity and  $k = 1.12$ .

The coefficient  $\beta$  for the LWC083, derived from (2) for ice-only clouds ( $T < -25^\circ\text{C}$ ), was 0.142. Figure A2 (d) displays a comparison between  $W_{\text{liq}}$  and  $W_{\text{liq}} + W_{\text{ice}}$  after filtering out the mixed and ice phase clouds. A comparison of LWC including bigger droplets (diameter  $> 50 \mu\text{m}$ ) was made with the WCM TWC156 and the CAPS (CAS+CIP) (Figure A2 (c)).

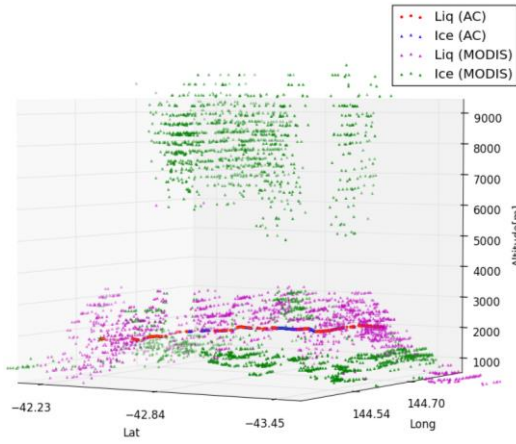
## Cloud phase observed by *in-situ* and MODIS in spatiotemporally coincided

Figure A3. Composite 3-D images of aircraft track and MODIS cloud phase optical properties (CPOP) retrieval pixels for each flight which are spatiotemporally coincided. The aircraft track is plotted with yellow line with green star for starting and purple star for ending point for the collocation. Cloud phase determined by aircraft measurements and MODIS CPOP product is indicated with different colours.

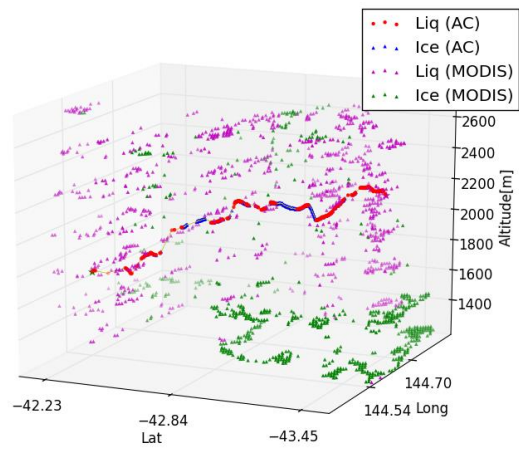




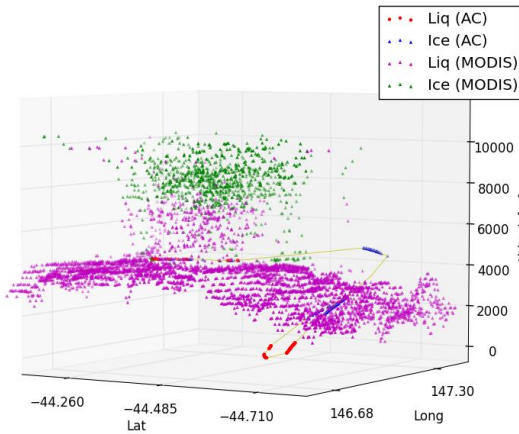
20130815\_122404



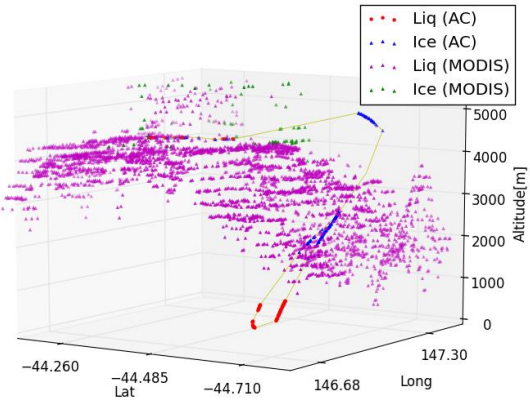
20130815\_122404



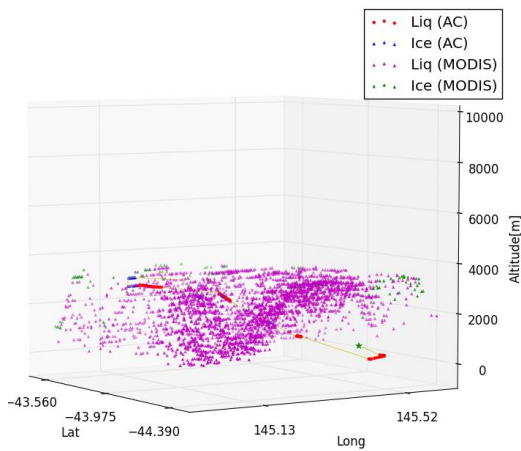
20131011\_132432



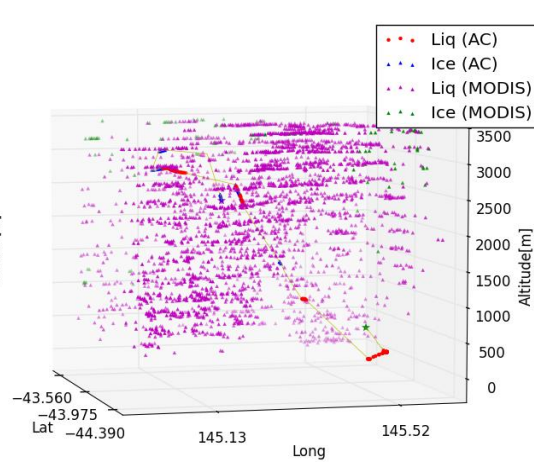
20131011\_132432



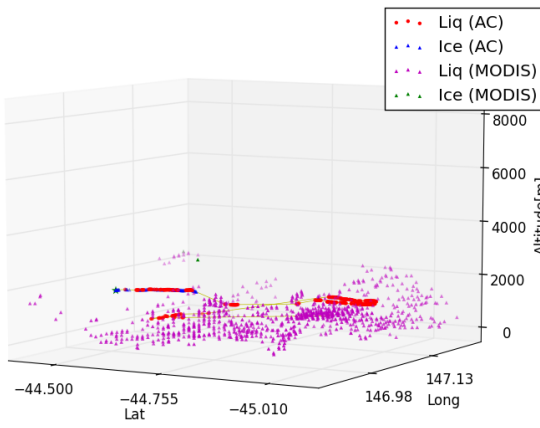
20140903\_124321



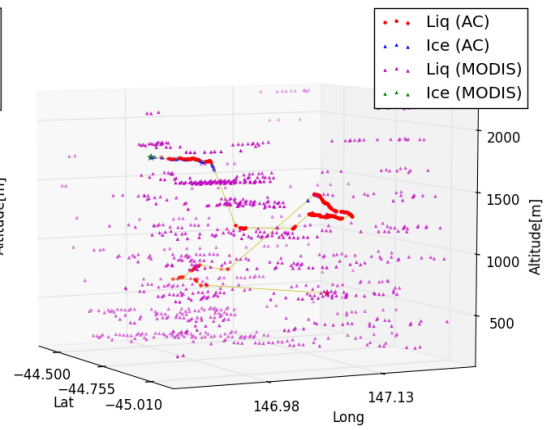
20140903\_124321



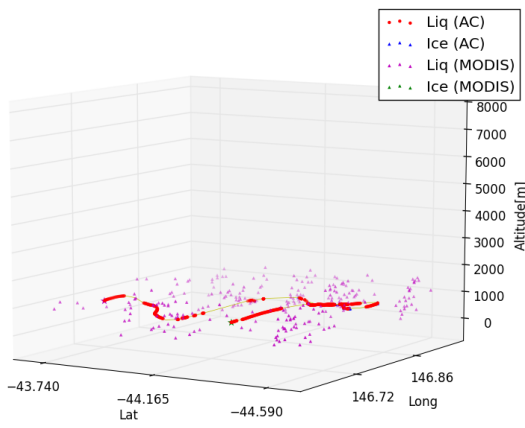
20140912\_124317



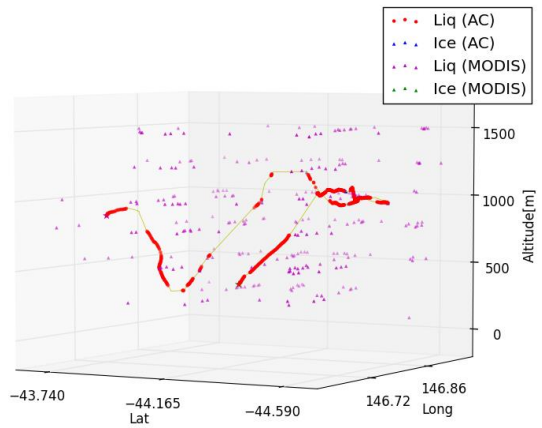
20140912\_124317



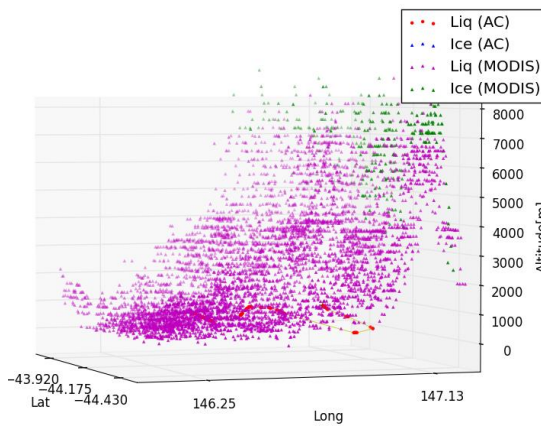
20150830\_130524



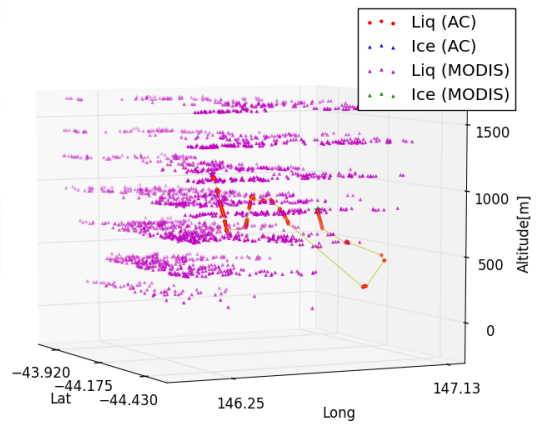
20150830\_130524



20151001\_123025



20151001\_123025



## Cloud CIP image



Figure A4. The CIP images of mixed/ice phase clouds for four flights which heavily or lightly experienced of ice.

## HYSPLIT back trajectory ensembles for the two high $N_d$ cases

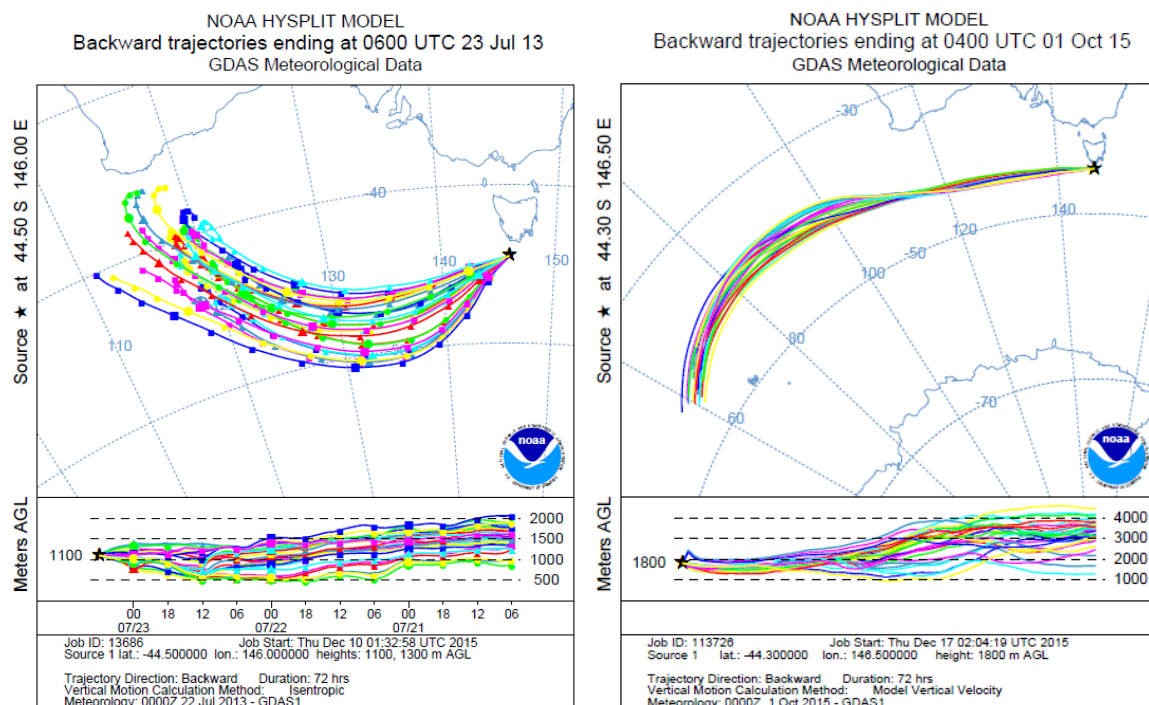


Figure A5. Hybrid Single Particle Lagrangian Integrated Trajectory Model (HYSPLIT) back trajectory ensembles for the high  $N_d$  cases (20130723 and 20151001).

## Mesoscale Cellular Convection (MCC)

Mesoscale Cellular Convection (MCC) is a regular pattern of convective cells that can develop in an atmospheric boundary layer heated from below or radiatively cooled from cloud top (Wood and Hartmann, 2006) and is commonly observed during cold air outbreaks as in Figure A6. Wood and Hartmann (2006) classified cloud in terms of MCC as four types; ‘No MCC’, ‘Cellular but disorganized’, ‘Open MCC’ and ‘Closed MCC’. Figure A7 illustrates the clouds classified by the MCC type for 20 flights.

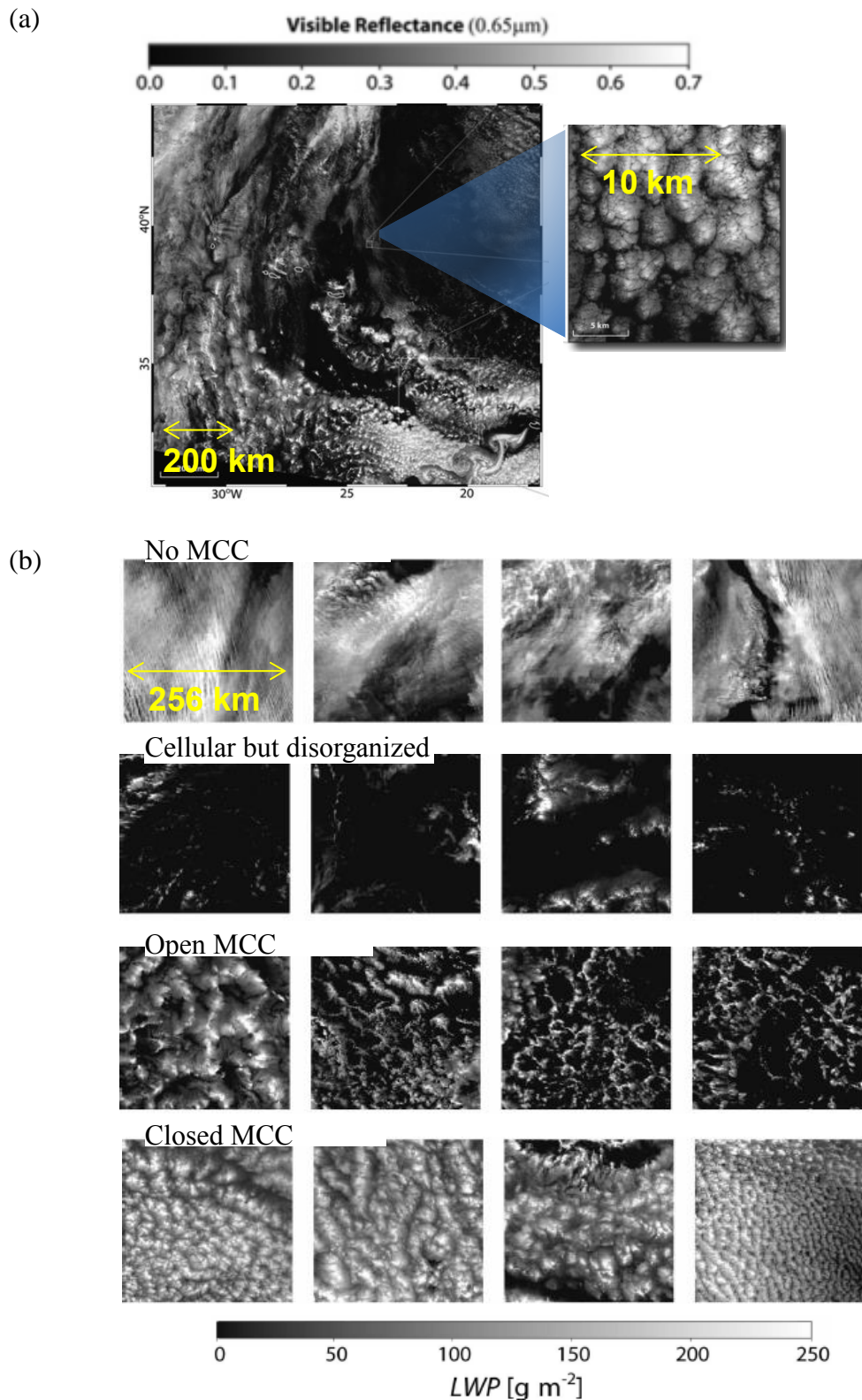


Figure A6. Mesoscale satellite imagery of cloud and MCC classification (a) a visible reflectance image (250-m resolution) for stratocumulus cloud by MODIS (left) and a visible image (15 m resolution) by Advanced Spaceborne Thermal Emission and Reflection Radiometer (ASTER) taken at 1235 UTC, 7 Apr 2001 over the northeast

Atlantic Ocean (Adapted from Wood (2012).) (b) Illustration of the MCC classification (Adapted from Wood and Hartmann (2006))

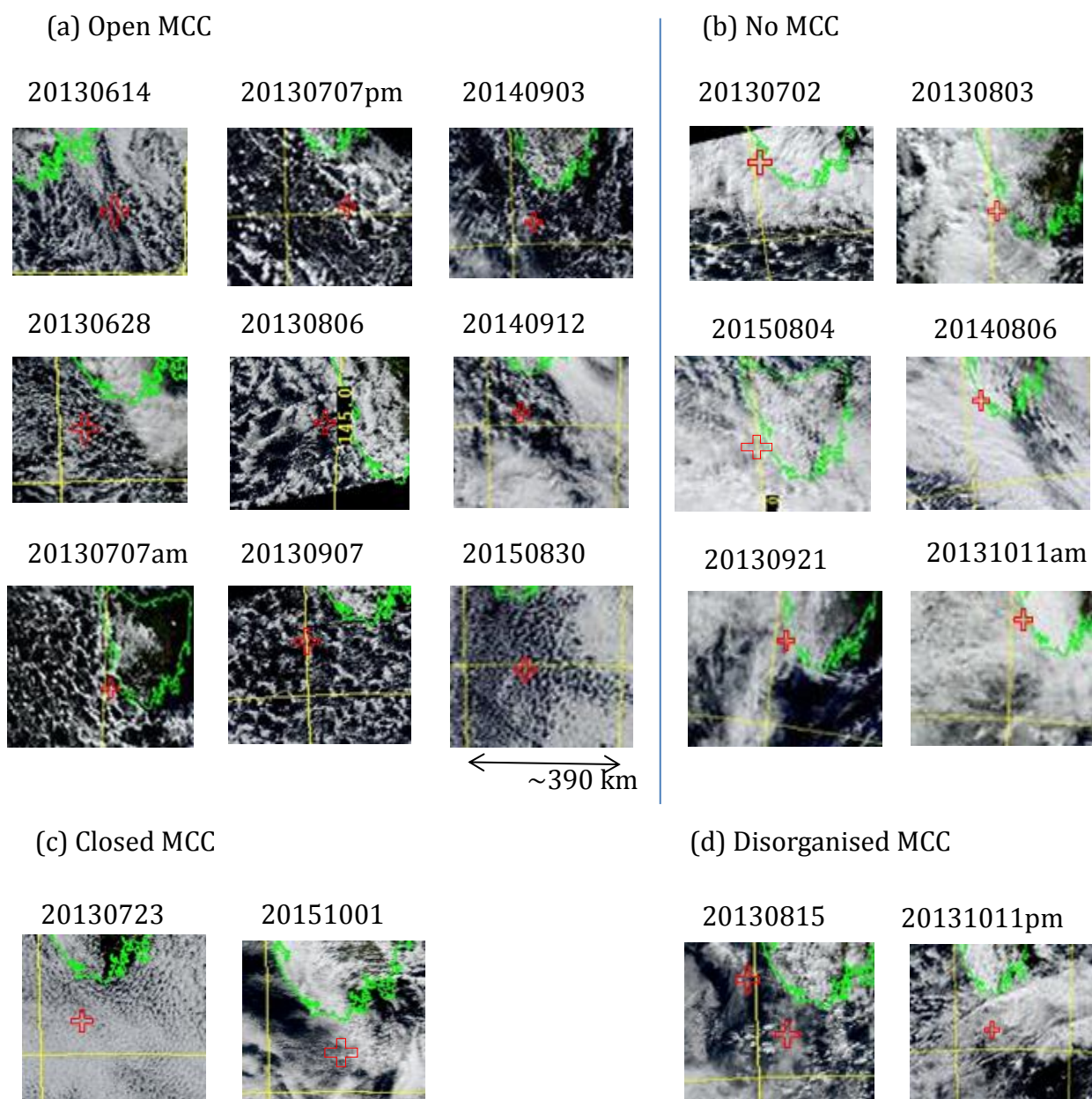


Figure A7. MODIS visual images sorted by MCC classification for the 20 flights. The flight location is marked as red on each image.

Mean Sea Level Pressure (MSLP) diagrams for the two high  $N_d$  flights

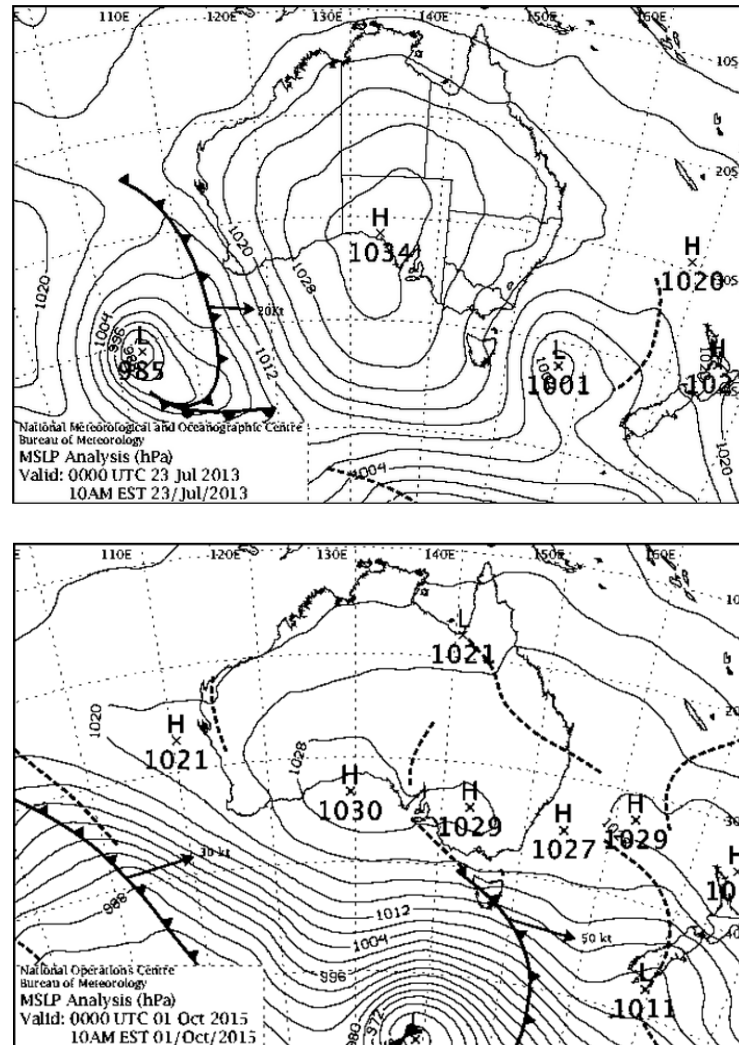


Figure A8. Mean Sea Level Pressure (MSLP) diagrams for the two high  $N_d$  cases (20130723 and 20151001).